LBL-30540

Lawrence Berkeley Laboratory

UNIVERSITY OF CALIFORNIA

Materials & Chemical Sciences Division

The Photodissociation of R-NO_2 Molecules

C.E. Miller
(Ph.D. Thesis)

April 1991

LOAN COPY
Circulates
for 4 weeks
Bldg. 50 Library.
LBL-30540
Copy 2

Prepared for the U.S. Department of Energy under Contract Number DE-AC03-76SF00098

DISCLAIMER

This document was prepared as an account of work sponsored by the United States Government. Neither the United States Government nor any agency thereof, nor The Regents of the University of California, nor any of their employees, makes any warranty, express or implied, or assumes any legal liability or responsibility for the accuracy, completeness, or usefulness of any information, apparatus, product, or process disclosed, or represents that its use would not infringe privately owned rights. Reference herein to any specific commercial product, process, or service by its trade name, trademark, manufacturer, or otherwise, does not necessarily constitute or imply its endorsement, recommendation, or favoring by the United States Government or any agency thereof, or The Regents of the University of California. The views and opinions of authors expressed herein do not necessarily state or reflect those of the United States Government or any agency thereof or The Regents of the University of California and shall not be used for advertising or product endorsement purposes.

Lawrence Berkeley Laboratory is an equal opportunity employer.

DISCLAIMER

This document was prepared as an account of work sponsored by the United States Government. While this document is believed to contain correct information, neither the United States Government nor any agency thereof, nor the Regents of the University of California, nor any of their employees, makes any warranty, express or implied, or assumes any legal responsibility for the accuracy, completeness, or usefulness of any information, apparatus, product, or process disclosed, or represents that its use would not infringe privately owned rights. Reference herein to any specific commercial product, process, or service by its trade name, trademark, manufacturer, or otherwise, does not necessarily constitute or imply its endorsement, recommendation, or favoring by the United States Government or any agency thereof, or the Regents of the University of California. The views and opinions of authors expressed herein do not necessarily state or reflect those of the United States Government or any agency thereof or the Regents of the University of California.

LBL-30540

The Photodissociation of R-NO_2 Molecules

C.E. Miller
Ph.D. Thesis

Chemical Sciences Division
Lawrence Berkeley Laboratory
University of California
Berkeley, CA 94720

April 1991

This work was supported by the Director, Office of Energy Research, Office of Basic Energy Sciences, Chemical Sciences Division, of the U.S. Department of Energy under Contract No. DE-AC03-76SF00098.

The Photodissociation of R-NO_2 Molecules

By

Charles Edward Miller

ABSTRACT

The internal energy distributions, $P(E_{int})$, are derived for rovibronically excited NO_2 ensembles produced from the photodissociation of R-NO_2 molecules (R = CH_3, C_2H_5, C_3H_8, HO, Cl) and the chemiluminescent NO + O → NO_2^* reaction. The $P(E_{int})$ distribution is evaluated using the Integrated Fluorescence (IF) method, which assumes that a dispersed NO_2 fluorescence spectrum can be represented by a linear combination of mono-energetic emitters.

The performance of the IF model was assessed using measurements of the NO_2^* spectral distribution from the NO + O → NO_2^* reaction. The results show that the NO_2^* $P(E_{int})$ distribution is sharply peaked at 25,130 cm^{-1}, the NO_2 dissociation energy, and has minimal contributions from components possessing less than 20,000 cm^{-1}, consistent with the kinetics and thermodynamics of this reaction. Tests also reveal that the optimized NO_2^* $P(E_{int})$ distribution obtained from the IF model depends strongly on the observation range and resolution of the data.

Photodissociation of nitromethane between 193.3nm and 248.5nm demonstrates that the NO_2^* $P(E_{int})$ transform from inverted distributions sharply peaked at 25,130 cm^{-1} to ones in which a majority of the NO_2^* components have internal energies

less than 15,000 cm^{-1} as the single photon excitation energy decreases from 51,000 cm^{-1} to 42,500 cm^{-1}. These findings suggest that the dissociations all originate on the $^1B_2$ surface, which results from a ($\pi \rightarrow \pi^*$) electron promotion localized on the NO_2 chromophore, but dissociate via different pathways. The $P(E_{int})$ derived from nitroethane and 1-nitropropane photolyses produce comparable results.

The wavelength dependence of $HONO_2$ and $ClNO_2$ photodissociations was investigated in greater detail. The NO_2^* $P(E_{int})$ for $ClNO_2$ evolve from distributions peaked at 25,130 cm^{-1} to those having a majority of the NO_2^* components with internal energies less than 15,000 cm^{-1} as the energy available to the photofragments decreases from 30,000 to 20,000 cm^{-1}. The NO_2^* $P(E_{int})$ distributions derived for $HONO_2$ are dominated by components with energies less than 15,000 cm^{-1} and only for photolysis wavelengths shorter than 255nm do the distributions have significant contributions from NO_2^* components approaching the maximum available energy. The transformations in the NO_2^* $P(E_{int})$ contours are linked to changes in which potential energy surface dominates the dissociation dynamics. The principal differences between $ClNO_2$ and $HONO_2$ photodissociations are explained in terms of the perturbations induced by the R group on the local C_{2v} symmetry of the NO_2 chromophore.

ACKNOWLEDGEMENTS

The seemingly Sisyphean task of completing this doctoral research and thesis required the assistance and dedication of many people. First and foremost, I would like to thank Professor Harold Johnston for the opportunity to work with him. He has provided me with excellent counsel on the ways one should think about Science and how to implement this advice. It is he I have to thank (or is it curse?) for introducing me the "spectroscopist's black hole", the infamous NO_2 molecule. I hope he has enjoyed this foray as much as I.

I have also been fortunate to work with a number of other people during my tenure in the Johnston Group and I am indebted to them as well. Wade Sisk provided much mirth and a skillful mechanic's touch during our molecular beam PIF experiments. Ken Patten was always available for computer consultations, and without his analysis codes, this work would have been far more taxing. I have also greatly benefitted from Ken's unique socio-political perspectives. Joel Burley, Phil Hunter, and Bongsoo Kim helped me survive this ordeal with their witty banter and comradeship. Daniel Oh and Doug Kinneson were enjoyable office partners and introduced me to the original experimental setup during my first year.

I would like to thank Mike Covinsky, Floyd Davis and Pam Chu of the Lee Group

for their lessons in time of flight spectroscopy. The members of various incarnations of Black Flag deserve special praise for their own ineptitudes and butchery of the art of softball.

Joel Bader, Jack Hartung, and John Price merit mention for the mythical adventures with which they helped fill my spare time. They are probably not unlike some of the greatest friends I personally have had, ever.

Finally, I would like to thank my family and Mary Louise. My successes have been due in no small part to their love and support.

This work was supported by the Director, Office of Energy Research, Office of Basic Energy Sciences, Chemical Sciences Division of the U.S. Department of Energy under contract number DE-AC03-76SF00098.

TABLE OF CONTENTS

ABSTRACT 1

ACKNOWLEDGEMENTS ii

TABLE OF CONTENTS iv

CHAPTER 1: The Energetics of the $NO + {}^{\bullet}O \rightarrow NO_2^{\bullet}$ Recombination Reaction

1.0 Abstract 1

1.1 Introduction 2

1.2 The $NO_2^{\bullet}$ Integrated Fluorescence Analysis Method 3

1.3 Data Preparation 9

1.3.A Bradburn Data 10

1.3.B Vanpee Data 11

1.3.C Paulsen Data 13

1.4 Results 14

1.4.A BRADBURN 15

1.4.B VANPEE and PAULSEN 17

1.4.C Fontijn and Becker Data 19

1.5 Discussion 20

1.5.A Evaluation of the IF Analysis Method 20

1.5.B Comparison to Other Experimental Results 27

1.6 Conclusions 36

CHAPTER 1:

THE ENERGETICS OF THE $NO + O \rightarrow NO_2^*$ RECOMBINATION REACTION

1.0 ABSTRACT

We report the internal energy distribution, $P(E_{int})$, determined for the fluorescing NO_2^* species from the chemiluminescent $NO + O \rightarrow NO_2^*$ recombination reaction. The $P(E_{int})$ distribution is evaluated using the Integrated Fluorescence (IF) method, which assumes that a dispersed NO_2 fluorescence spectrum can be represented by a linear combination of mono-energetic emitters. We have previously used IF analysis to derive NO_2^* $P(E_{int})$ distributions for R-NO_2 photodissociation and NO_2 collisional energy transfer experiments; however, these spectra only recorded the emission intensity between 25,000 and 12,000 cm^{-1}. We use measurements of the NO_2^* spectral distribution from the NO + O recombination to evaluate the performance of the IF model when analyzing data that extends the low energy observation limit to 6000 cm^{-1}. The results show that the NO_2^* $P(E_{int})$ distribution is sharply peaked at the NO_2 dissociation energy of 25,130 cm^{-1} and has minimal contributions from components possessing less than 20,000 cm^{-1}, consistent with the known kinetics and thermodynamics of this reaction. They also reveal that the optimized NO_2^* $P(E_{int})$ distribution obtained from the IF model depends strongly on the observation range and resolution of the data. A lesser dependence was found on the nature of the weighting function used to describe the linear combination of NO_2 emitters which constitute the NO_2^* ensemble.

1.1 INTRODUCTION

In this report we continue our analysis of the internal energy distributions, $P(E_{int})$, of fluorescing NO_2 ensembles, NO_2^*, created by various chemical and physical processes[1,2,3,4,5]. This is done by deconvoluting the dispersed NO_2^* fluorescence spectrum created by the process of interest into its mono-energetic components using the Integrated Fluorescence (IF) method. This method was initially developed to study energy partitioning in R-NO_2 photodissociation and NO_2 collisional deactivation experiments, but its derivation is general. It can, therefore, be used to derive $P(E_{int})$ information from any process which generates a NO_2^* ensemble, including the interesting chemiluminescent reaction

$$NO + O(^3P) \rightarrow NO_2^* \qquad \text{(R1)}$$

All previous applications of the IF method have been conducted on data which were experimentally limited to a 380 - 850nm (26,500 - 12,000 cm^{-1}) observation window, although the NO_2^* emission extends to longer wavelengths. The present investigation was motivated by the recent remeasurement of the NO_2^* emission from R1 between 380 and 1700 nm (26,500 - 6000 cm^{-1}) [6]. Analysis of these data simultaneously enables us to evaluate the performance of the IF model for data containing observations at energies lower than 12,500 cm^{-1} and to provide a the first NO_2^* $P(E_{int})$ distribution for R1.

1.2 THE NO_2^* INTEGRATED FLUORESCENCE ANALYSIS METHOD

The mathematical derivation of the IF method has been described in detail elsewhere[2-5]. Below we provide a qualitative outline of the method's salient features and the peculiar features of NO_2 spectroscopy which motivated its development.

The NO_2 molecule is infamous for its spectral complexity. A moderately resolved NO_2 absorption spectrum shows a single broad continuum centered at 400nm and extending past 800 nm into the near infra red with irregular vibronic structure superimposed on it. At energies greater than 25,130 cm^{-1} individual rotational transition lines become diffuse, signalling the onset of predissociation. Myriad spectral lines blend to form the apparent continuum at resolutions above 1 cm^{-1}: Hsu, Monts, and Zare catalog over 19,000 lines in the 560-648nm range alone[7]. The unexpectedly large number of observed transitions indicates the breakdown of the normal transition selection rules and the onset of spectral chaos[8,9,10,11]. This is due to the presence of four mutually coupled electronic surfaces below the predissociation threshold - X $^2A_1$, A $^2B_2$, B $^2B_1$, and C $^2A_2$ (Figure 1). It is possible to assign quantum states to selected portions of the spectrum, but these regions of regularity are difficult to initially identify and constitute a small fraction of the total spectrum.

The NO_2 fluorescence excitation (FEX) spectrum has proven equally inscrutable

because a deep conical intersection strongly perturbs the X $^2A_1$ and A $^2B_2$ zero-order potential surfaces[8,12,13,14,15]. The origin of the perturbation is seen in the intersection of the $^2A_1$ and $^2B_2$ surfaces near 110° in Figure 1. Smalley, Wharton, and Levy[16] first demonstrated that the NO_2 FEX spectrum in a 10 K supersonic jet expansion contained nearly six times as many vibronic origins as would be expected from normal mode calculations. More recently Demtröder and co-workers[8] have re-investigated the FEX spectrum using sub-Doppler resolution and covering energies from 13,000 to 24,000 cm^{-1}. Analysis of the energy level spacing statistics between vibronic origins of b_2 symmetry shows that they exhibit gaussian orthogonal ensemble (GOE) characteristics. The presence of GOE spectral fluctuations indicates the absence of "good" electronic or vibrational quantum numbers and that energy is the only appropriate label for excited eigenstates of NO_2 [7]. In other words, the $^2A_1$ and $^2B_2$ surfaces are inextricably intermixed and adequate descriptions of these potential surfaces are only possible using non-adiabatic bases. A final peculiarity of the NO_2 FEX spectrum is that the fluorescence quantum yield which remains constant at unity below D_0 decreases abruptly by at least a factor of 10^{-6} at energies immediately above 25,130.6 cm^{-1} [4]. The virtual coincidence of the predissociation threshold, the thermodynamic threshold, 25,125 cm^{-1}, and the fluorescence cessation energy indicates a predissociative mechanism, probably involving a crossover from the upper ($^2B_2$) surface to the lower ($^2A_1$) surface, with virtually no barrier to dissociation on the lower surface.

The IF model circumvents the complexities of a fully resolved NO_2 spectrum by

sacrificing individual eigenstate information and considering only the total internal energy content of the emitting NO_2^* ensemble. This seems reasonable given the chaotic nature of NO_2 spectra. Data are instead recorded in ~2.0nm wide observation windows across the spectrum, producing an empirical "averaging" of the emission intensity. The observed wavelength dependent spectral distribution is then transformed into the corresponding energy dependent function for analysis. The IF model assumes that any dispersed NO_2^* spectrum is described by a linear combination of mono-energetic NO_2 emitters, and determines the weighting coefficients which best define the linear combination of NO_2 emitters using the energies from the observed data as a basis set. The weighting coefficients are optimized by a non-biased least squares algorithm.

In early applications of this method, it was found that optimization of the weighting coefficients was more efficiently accomplished by comparing the calculated and experimental cumulative integrated intensities rather than the calculated and experimental fluorescence spectra. By cumulative integrated fluorescence we mean the total fluorescence intensity as a function of displacement from $D_0(NO_2)$. For example, the value of the integrated fluorescence intensity at 20,000 cm^{-1} (500nm) is given by summing the fluorescence intensities in all of the bins from $D_0(NO_2)$ (25,130.6 cm^{-1}, or roughly 398nm) to 20,000 cm^{-1}. The value of the integrated fluorescence intensity at 19,920 cm^{-1} (502nm) is given by summing the intensities in all of the data bins from $D_0(NO_2)$ to 19,920 cm^{-1}, etc. In this manner the IF curve is mapped out as a function of the observed fluorescence energies. A graphical description of the transformation and

resulting fits is given in Figure 2. Normalization of the total fluorescence intensity transforms the IF function into a well behaved continuous function that asymptotically approaches 0 at $D_0(NO_2)$ and 1 at the lowest observation energy. If the lowest observation energy cuts off significant amounts of the total NO_2^* emission profile, then the approach at this limit will not be asymptotic. Note that the original fluorescence spectrum can be retrieved from the integrated fluorescence function by differentiation with respect to energy. It is far easier to achieve fast computational minimization of the fitting residual to the well-behaved cumulative integrated fluorescence function than to the highly oscillatory fluorescence spectrum, thus our reason for the transformation. The accuracy of a given set of optimized coefficients is determined by the square of the total fitting residuals between the calculated and experimental cumulative integrated fluorescence functions. This value is referred to as the sum error.

The relative contributions of the mono-energetic NO_2^* emitters are currently determined by using one of three weighting functions:

$$F(X_L) = \left(\frac{1}{2\pi B^2}\right)^{\frac{1}{2}} \exp\left[\frac{-(A - X_L)^2}{2B^2}\right] \tag{1}$$

$$F(X_L) = \exp\left[\frac{-(M - X_L)}{A}\right]\left(1 - \exp\left[\frac{-(M - X_L)}{B}\right]\right) \tag{2}$$

$$F(X_L) = \left(\left[\frac{M - X_L}{A}\right] \exp\left[\frac{-(M - X_L)}{A}\right] \right)^B \qquad (3)$$

In these equations X_L stands for the specific rovibronic energy possessed by an excited NO_2 molecule or ensemble of molecules. In a separate series of experiments, this group has empirically determined the dependence of the cumulative integrated fluorescence intensity as a mutual function of X_L *and* observation energy[1,2]. The weighting function parameters are optimized to minimize the fitting residual between the calculated and observed IF functions.

Equation (1) is the well known Gaussian function with the fitting parameters A and B representing the mean and width of the distribution, respectively. Equation (2) is a biexponential function where A and B represent the declining and rising rates of the two exponential components (C_d and C_r). Equation (3) is called the gamma kernel because it is the integrand of the incomplete gamma function. The parameter M in Equations (2) and (3) provides an origin point for the weighting functions and is often allowed to vary in obtaining globally optimized fits, although populations components with $E_{int} > 25,130$ cm^{-1} are automatically set equal to zero regardless of the M value.

The set of A, B, and M parameters which minimizes the least squares residual between the experimental and calculated cumulative integrated fluorescence intensity

curves are used as the optimized values. The weighting coefficients produced by the optimized parameters are then transformed into the NO_2^* $P(E_{int})$ distribution by correcting them for the internal energy dependent NO_2 radiative lifetime and for thermal excitation of the NO_2 parent[5]. The optimized parameters have no physical significance aside from describing the shape of the various coefficient functions.

The individual weighting functions were selected because of their flexibility in producing continuous forms thought to be possible shapes of the NO_2 $P(E_{int})$ distributions. The gaussian coefficient function, Equation (1), was the function used in the earliest form of the PIF analysis[1]. The biexponential function, Equation (2), is especially well suited at producing coefficient distributions which are peaked near M and fall off exponentially to lower energies. This coefficient function models very narrow $P(E_{int})$ distributions quite well, such as those generated by NO_2 LIF experiments. The gamma kernel function, Equation (3), is the most versatile of the coefficient generators: it can approximate the contours of the gaussian, or biexponential coefficient functions, as well as producing contours these functions are incapable of creating.

Populations obtained from the optimized fits are normalized over the range of data used in that particular fit. The average energy, root mean square energy, and most probable energy are calculated from the normalized population components for numerical comparison. For example, the average energy of the distribution is calculated from by summing $P(E_{int})*E_{int}$ over all of the energies in the basis set.

1.3 DATA PREPARATION

We have used the IF method to analyze data from the different experimental determinations of the NO_2^* spectral distribution, $I(\lambda)$, from R1 shown in Figure 3. Due to the memory capacity of the computers used in this study, the data used in analysis are limited to a maximum size of 400 points. Each point consists of an NO_2^* emission intensity measurement and the wavelength bin in which that measurement was stored.

The data were subdivided for the following tests:

RESOLUTION: The data for a given set were "recorded" at 1, 2, or 4nm intervals across the specified observation range. This variation tests the effect of fixed experimental resolution on the resulting $P(E_{int})$ distributions for nominally identical data.

OBSERVATION RANGE: Each analysis determines the NO_2^* $P(E_{int})$ distribution between D_0 and a specific lower energy limit. The possible lower energy limits that could be tested depended on 1) the extent of the experimental data, 2) the resolution, or wavelength increment between points, and 3) a maximum of 400 points in a single subset. This test assesses the impact of the lower energy observation limit on the calculated

$P(E_{int})$ distribution. Standard ranges and the allowable resolutions are given in Table I.

M PARAMETER: We note that there are two very similar values in this work that have entirely different definitions. There is the maximum energy available to the fluorescing NO_2 ensemble, hereafter denoted as θ, and the weighting function parameter M which may coincide with θ, but is only a fitting parameter used to mark the origin of the biexponential and gamma kernel weighting functions. Part of the confusion results from the fact that both θ and M are values determined relative to the zero point vibrational energy of the NO_2 $^2A_1$ electronic groundstate. We calculated optimized weighting function parameters for M values of 25,000; 26,000; and 27,000 cm^{-1}, a range of θ energies consistent with a minimal barrier inverse predissociation mechanism for R1. In this work, 25,000 cm^{-1} was chosen as the minimum M value, roughly corresponding to $D_0(NO_2)$. This test enables us to determine the influence of the M parameter value when it has values energetically inaccessible to the NO_2^* ensemble.

1.3.A. Bradburn Data

Data from the study of Bradburn and Levelenfield[6], hereafter referred to as the

BRADBURN set, were obtained from the authors in tabulated form. The I(λ) measurements in this set were recorded between 350 and 1700nm at 1nm intervals by dispersing the emission through a 0.25 meter monochromator using a 1180 lines/mm grating blazed at 600nm for the visible signals and a 590 lines/mm grating blazed at 1000nm for the IR signals. The fluorescence signal was detected continuously using 200 Hz modulation. A PMT registered the emission signals between 380 and 800nm. A cooled Ge detector monitored the 750 - 1700nm fluorescence. Filters blocking visible fluorescence protected the spectrum against contamination from second order grating effects in the IR. Absolute emission intensities were calibrated with respect to the $O_2(^1\Delta)$ at 1270nm. The total reaction pressure was maintained at 1000 millitorr.

We adopt the BRADBURN set as the standard for IF fitting evaluations since we have the complete data at our disposal. Individual subsets of the BRADBURN data used in the resolution test were obtained by beginning at 380nm and selecting subsequent points from the set at the stated wavelength interval, the set's resolution. Subsets of the BRADBURN data used in testing the effect of the lowest observable energy on the NO_2^* $P(E_{int})$ distributions were obtained by collecting all points from 380nm to the desired long wavelength limit at the specified resolution.

1.3.B. Vanpee Data

The experimental measurements of Vanpee, Hill, and Kineyko[17], hereafter referred to as the VANPEE data, were digitized from Figure 4 of Reference 17 at 50nm

intervals from 400 - 1800nm. The VANPEE study eliminates many of the discrepancies between the visible and IR emission intensities by recording the 600 - 1500nm portion of the spectrum with the same detector, a specially enhanced PMT. To further guarantee proper absolute intensity measurements, these authors calibrated their optical collection system against a series of NBS standard emission lamps over the entire 400 - 2000nm range.

The recombination emission was generated in a subsonic jet with total pressure of 1 Torr. The optical detection system consisted of a prism dispersing monochromator having a linear dispersion of 30 nm/mm in the visible and 200 nm/mm in the IR. Photon signals were detected continuously.

The subsets required for IF analysis were obtained by calculating a cubic spline interpolation[18] to the digitized data. The minor undulations in the rising edge (400 - 500nm) of the data are due to the interpolation of slight digitization errors. This curvature was greatly reduced by digitizing points at a 20nm interval from 400 to 500nm, but some residual undulations remain in the interpolated spectrum. The VANPEE data were subjected to the same series of IF analysis tests as the BRADBURN data; subsets were obtained by interpolating the digitized data from 390nm to the desired long wavelength limit with the appropriate resolution increment between points. However, due to the wide spacings of the digitized points, no subset was generated for the 1nm resolution test.

1.3.C. Paulsen Data

Data from the study of Paulsen, Sheridan, and Huffman[19], hereafter referred to as the PAULSEN data, were digitized from Figure 4 of Ref 19. The solid circle points included in that figure were assumed to have 10nm spacing from 390 - 860nm, and the emission intensities

were digitized from the positions of these points, not the smooth line also present in this figure. The data marked by cross hairs in this figure represent the relevant points from the FONTIJN[20] data which were used by Paulsen et al. to verify their absolute emission sensitivity calibration over the 380 - 890nm range. CW monitoring of the emission signal at a modulation frequency of 400 Hz was employed. Total pressures were maintained in the range of 2 - 5 Torr.

Interestingly, these authors reported observing low intensity banded structure superimposed on the emission continuum for wavelengths shorter than 630nm. These bands only rose 5 - 10% above the intensity of the continuum intensity and appeared diffuse on the photographic plates. However, there were a series of bands observed between 383.2 and 395.7nm (26,096 - 25,272 cm^{-1}) which have energies *greater* than the NO_2 predissociation energy of 25,130 cm^{-1}. The band observed at 383.2nm would seem to place a lower limit of 26,096 cm^{-1} on θ.

Cubic spline interpolations were calculated over the entire 390 - 860nm range for wavelength increments of 1, 2, and 4nm. All of the PAULSEN interpolated subsets had

a lower energy limit of 12,250 cm^{-1}. The interpolated data show some undulations near the emission maximum, consistent with the data which they reflect. The largest interpolation calculates 10 new points between each digitized point, but the interpolated data are well behaved even for this case.

The PAULSEN data are included primarily because they were measured in an experimental arrangement very similar to that which we currently employ in the measurement of R-NO_2 PIF and NO_2^* collisional deactivation studies. The response function of a GaAs photomultiplier tube determines the long wavelength (low energy) observation limit. We expect IF analysis of the PAULSEN data to reflect possible inadequacies of data which view a limited portion of the total NO_2^* spectral distribution.

1.4 RESULTS

The data described above were analyzed using the IF method with variation of weighting function, observation range, resolution, and M value. Optimized fitting parameters were determined by a least squares algorithm which minimized the residual between the calculated and experimental integrated fluorescence intensity functions.

The sum error values reported for specific sets of optimized parameters have been reduced to reflect the statistical error of any individual point in the fit. This number is

inversely proportional to the square root of the number of points in the set. The total error values, where

$$\text{Total Error} = \text{Sum Error} \times N^{1/2}$$

remove the dependence on the number of points in the set from the measurement of fitting accuracy. However, parameter optimization was still based on a minimization of the sum error value and this is the figure of merit one should use to compare various populations.

The IF analysis results are plotted in three different ways to correspond with the battery of tests used in performance evaluation. Each figure in the first series illustrates the three $P(E_{int})$
calculated for a specific subset using the three weighting functions. The second series is grouped by weighting function and resolution: these figures display how variation of the low energy observation limit affects the $P(E_{int})$ distributions. The third series demonstrates how the NO_2^* $P(E_{int})$ distributions change as the experimental resolution is varied. The optimized weighting function parameters and numerical descriptions of the $P(E_{int})$ referred to below are found in Tables III-VII, IX-XI, and XIII-XV for the BRADBURN, VANPEE, and PAULSEN data, respectively.

1.4.A. BRADBURN

The BRADBURN data, shown in Figure 2A, yielded the NO_2^* $P(E_{int})$ shown in Figures 4-22. Figure 4 exhibits the NO_2^* $P(E_{int})$ determined from each of the weighting functions for the subset having 1nm resolution and a 12,750 cm^{-1} lower energy observation limit. These population contours reproduce virtually the same population contour despite the marked differences in the weighting functions. The NO_2^* $P(E_{int})$ is inverted, peaks sharply at $D_0(NO_2)$, has minimal contributions from NO_2^* components below 18,000 cm^{-1} and has an average energy of ~21,500 cm^{-1} (Tables II, IV, and VI). Figures 5-7 show the $P(E_{int})$ produced by the three weighting functions for subsets having 2nm resolution. The outstanding aspect of these plots is the increased breadth near 24,000 cm^{-1} of the NO_2^* $P(E_{int})$ derived for the subset which only extends to 12,250 cm^{-1}. Again, there seems to be little difference between the populations produced by the different weighting functions. The first series of BRADBURN data plots is concluded with the $P(E_{int})$ for the 4nm resolution subsets shown in Figures 8-13. These figures again demonstrate that the different weighting functions produce nearly identical $P(E_{int})$ distributions, and that the NO_2^* $P(E_{int})$ from R1 is inverted.

The results of the observation range test are given in Figures 14-19 with these plots arranged according to weighting function. All of these Figures have been truncated at a low energy limit of 12,000 cm^{-1} for display purposes, but, as can be seen, this does not affect the comparisons. The most pronounced feature in each of these figures is the difference between the $P(E_{int})$ derived for the subset including data only to 12,500 cm^{-1} compared to the $P(E_{int})$ from other subsets. In each case the $P(E_{int})$ associated with the

smallest observation window distorts the $P(E_{int})$ in the 20,000 to 25,000 cm^{-1} region. Tables III-VI also show that the sum errors to the A1X and B1X subsets are larger than the sum errors for the other subsets having the same resolution. This indicates that not only are the $P(E_{int})$ derived from the smallest observation window subsets distorted from the other $P(E_{int})$, but that they additionally generate larger fitting residuals (poorer fits) than the other population distributions.

The results of the data resolution test are highlighted in Figures 20-22 for the three weighting functions and the $P(E_{int})$ derived for the C1X (1nm resolution), A1X (2nm resolution), and B1X (4nm resolution) subsets. The maxima of the $P(E_{int})$ have been equated for comparison in each of these figures. The Gaussian and biexponential $P(E_{int})$ in Figures 20 and 21 illustrate that the 1nm resolution subsets produce more sharply peaked populations. The general trend gleaned from these figures is that lower resolution subsets produce NO_2^* $P(E_{int})$ which are broader and have proportionately more concentration of NO_2^* components in the 20,000 to 25,000 cm^{-1} range than the higher resolution subsets. The shift in $P(E_{int})$ contour also includes a red shifting of the $P(E_{int})$ maximum in several cases.

1.4.B. VANPEE and PAULSEN

The results for the VANPEE data, see Figure 3, are presented in the same format as the BRADBURN data. Figures 23-33 show that the NO_2^* $P(E_{int})$ for these data are

quite similar to the BRADBURN $P(E_{int})$, displaying maxima near $D_0(NO_2)$ and having minimal NO_2^* components with energies less then 18,000 cm^{-1}. Tables IX-XI show that the VANPEE populations have somewhat higher average energies, ~23,000 cm^{-1}, however. The agreement of the $P(E_{int})$ determined from each weighting function for a given subset is again very good, and the gamma kernel and gaussian $P(E_{int})$ become nearly indistinguishable for certain subsets. Figures 34-39 again illustrate the distortion in the $P(E_{int})$ caused by limited observation range, although the effect is not nearly as large for these data as for the BRADBURN data. Since no subset with 1nm resolution was analyzed for the VANPEE data, figures directly comparing the effect of varying the experimental resolution are not given, but it can be seen from Figures 23-39 that there is no great discrepancy between the 2nm and 4nm resolution subsets.

The PAULSEN data have an intrinsic low energy observation limit of 12,000 cm^{-1}, so no test of the observation range was made for this data. Figures 40-42 show the $P(E_{int})$ calculated from the different weighting functions for a specific resolution follow the same pattern seen for the BRADBURN and VANPEE data. Tables XIII-XV indicate that the PAULSEN $P(E_{int})$ have substantially lower average energies than those determined for the BRADBURN and VANPEE data. Additionally, there is no discernable trend in Figures 43-45 for the behavior of the $P(E_{int})$ associated with a variation in the subset resolution.

1.4.C. Fontijn and Becker Data

We also submitted interpolated data from the I(λ) measured for R1 by Fontijn, Meyer, and Schiff[20], but the IF least squares fitting algorithm was unable to converge on optimized parameters for these data. All of the sum error values obtained in the IF analysis battery were greater than 4.0×10^{-3} and many were larger than 1.0×10^{-2}; we generally discard any fits with sum errors larger than 3.0×10^{-3}. We believe the reason that the IF analysis failed to converge for this data is that this measurement of the I(λ) underestimates the amount of IR emission: Fontijn et al. observed no emission past 1400nm, probably due to the relative insensitivity of their PbS detector. The studies of Vanpee et al.[17], Sutoh et al.[21], Stair and Kennealy[22], and Bradburn and Levelenfield[6] indicate that the NO_2^* emission profile extends well past the 1400nm limit observed by Fontijn et al.

Becker, Groth, and Thran[23] recorded a series of pressure dependent NO_2^* I(λ) profiles at pressures from 0.25 to 1000 mT. As with the Fontijn data, the IF optimization procedure did not generate converged parameters for these data. The lowest sum error value was 5.8×10^{-3}. This is disappointing, since we had hoped to determine through our analysis the internal energy of the NO_2^* ensembles as a function of reaction pressure. The total reaction pressure should be roughly proportional to the number of collisions an average NO_2^* molecule undergoes prior to emission, so these data provide another means to evaluate the rate of NO_2^* collisional deactivation. Becker et al. used

calculations based on a stepladder model to conclude that each hard sphere collision removed ~800 cm^{-1} from an NO_2^* molecule.

We believe that the inability of the IF optimization algorithm to generate converged fits for the Becker data is due to an extrapolation applied by the authors to their data recorded for wavelengths longer than 750nm: "The spectrum above 750nm was roughly analyzed with a linear variable filter and a PbS detector showing that extrapolations of the spectral distribution between 400 and 750nm to the long wavelength limit of the NO_2^* chemiluminescence at 1400nm [Fontijn study[19] referenced] caused an uncertainty within 40% of the present limit." It seems that the Becker data measured between 400 and 750nm were extrapolated to a 1400nm limit using the Fontijn data as a scaling reference, and that this extrapolation agreed with the Becker IR measurements to within 40%. Our analysis of the FONTIJN data clearly show that it is not fit nearly as well by the IF method as data with significantly more IR emission. Therefore, it we were probably unable to obtain converged fits to the Becker data due to their extrapolation of the IR emission falloff.

1.5 DISCUSSION

1.5.A Evaluation of the IF Analysis Method

We have evaluated the performance of the IF analysis method using an extensive

battery of tests on the data from R1 provided by Bradburn and Levelenfield[6]. The most important factor in this evaluation is the sum error value determined between the calculated and experimental IF curves for a given set of optimized weighting function parameters. Tables III-VII contain the information required for these assertions.

We use Table V containing the optimized gamma kernel weighting function parameters for the BRADBURN subsets with 1 and 2nm resolution to demonstrate how comparisons between optimized $P(E_{int})$ are made. The "Set" column refers to the specific subset of the data for which the parameters apply. Multiple occurrences of each set are the result of variations in the M parameters, as seen in the second column. The optimized A and B parameters are given in the next columns. The sum error is reflects the fitting residual per point provides the proper value to use when comparing subsets with different numbers of points. The adjacent total error column provides the entire fitting residual. The final three columns contain numerical information on the NO_2^* $P(E_{int})$ distributions.

Observation Range Test:

One primary motivation in this study is assessing the impact of extending the NO_2^* fluorescence observation window to include energies lower than 12,000 cm^{-1}, wavelengths longer than 800nm, on the calculated NO_2^* $P(E_{int})$ distributions. We know that the NO_2 fluorescence spectrum extends well past the 850nm detection limit of experiments

conducted in our laboratory, but we remained unsure what quantitative effect the inclusion of such data would have on our NO_2^* $P(E_{int})$ distributions. This question is especially pertinent to the NO + O recombination reaction since Figure 2A illustrates that nearly half of the emitted photons have energies below 12,000 cm^{-1}, while the reaction's thermodynamics and spectral distribution suggest that the NO_2^* components producing this emission are concentrated around 25,000 cm^{-1}.

We found that the fitting accuracy increased as the observation window included data for energies less than 12,000 cm^{-1}. Table III shows that the sum error associated with Gaussian weighting function fits minimized for the 4nm resolution B4X subset whose low energy limit is 8000 cm^{-1}, although the B3X and B5X subsets with low energy limits of 9000 and 7000 cm^{-1} have only slightly larger residuals, as does the 2nm resolution A3X subset with a 9000 cm^{-1} lower energy limit. Tables IV and V show that the B4X and B5X subsets produce the lowest sum error residuals for biexponential weighting function parameters. Tables VI and VII show that the gamma kernel weighting function favors the A3X subset. One can see from these tables that the sum error values systematically favor an observation window which has its low energy limit at 8000 or 9000 cm^{-1}. Further increases in the observation range result in higher sum error residuals. This trend is observable for all of the applied weighting functions at all resolutions and M values.

We propose two main reasons for these tendencies. Recall that the parameters derived for IF analysis are based on the fluorescence spectra of mono-energetically excited NO_2 ensembles. These measurements were made with an 26,000 - 12,000 cm^{-1} observation window. Additionally, experimental measurements of the NO_2^* radiative lifetimes are only known between $D_0(NO_2)$ and 13,300 cm^{-1}. Therefore, the model's behavior outside of the 25,130 - 12,000 cm^{-1} window is uncalibrated and purely speculative. However, the functions used by the IF fitting algorithm are continuous and well behaved inside the calibrated range, so that their extrapolations should be satisfactory approximations for a limited energy range below 12,000 cm^{-1}. The increasing fitting residuals for subsets which include data points below 9000 cm^{-1} probably signal the breakdown of the IF extrapolations. We also note the coincidence of our preferred low energy observation limit with the 9750 cm^{-1} value determined from *ab initio* calculations for the electronic origin of the NO_2 $^2B_2$ electronic state. Furthermore, the $^2A_1/^2B_2$ conical intersection which severely perturbs the NO_2 visible absorption spectrum is thought to occur very close to the $^2B_2$ minimum[12-15]. The $^2B_2$ electronic state provides the electric dipole transition strength to the low energy portion of the NO_2 absorption spectrum. So a severe perturbation of the bright state or its ceasing to exist could also be responsible for fitting inaccuracies below 9000 cm^{-1}. It is very likely that our results reflect both of these conditions.

We also note from Tables III-VII that the $P(E_{int})$ distributions derived from data subsets which extend only to 12,250 cm^{-1} have maxima red shifted compared to the $P(E_{int})$

distributions derived from subsets viewing more of the fluorescence signal. The reason for this result is unclear. There should be more than sufficient energy range for the coefficients and $P(E_{int})$ to sample when the lower energy bound is 12,500 cm^{-1} to achieve adequate fitting. The high concentration of NO_2^* components near $D_0(NO_2)$ also makes this result puzzling. Based on the trends and results seen here as a function of the lower energy bound, we can only conclude that since the 12,500 cm^{-1} lower limit truncates the NO_2^* emission spectrum while it is still intense, the resulting $P(E_{int})$ overweights the contributions from the lower energy components. Viewing 2000 to 3000 cm^{-1} more of the spectrum enables the model to more accurately judge the contributions of low energy NO_2^* components to the overall emission profile.

Resolution Test:

We found the IF analysis to be very sensitive to the resolution, or wavelength increment between successive data points. This test is best understood by comparing the total errors for the C1X (1nm), A1X (2nm), and B1X (4nm) optimized fits. The results are quite surprising. In each case the sum error values for the 1nm resolution subset are much lower than for the

2 or 4nm resolution subsets. A comparison between the results of the 2nm and 4nm for observation ranges extending to 9000 cm^{-1} show that the sum error values for these cases are nearly equivalent for both resolutions.

The best explanation for these results recognizes the difference in how the spectral distribution is measured. Experimental limitations require the fluorescence spectra to be acquired in linear wavelength increments. However, we wish to analyze the data in terms of energy. Therefore, the mono-energetic NO_2 components used in IF analysis disproportionately sample the energy space covered by the emission profile. A 2nm wavelength difference at 400nm corresponds to a 125 cm^{-1} energy difference, while a 2nm wavelength difference at 800nm corresponds to an energy difference of only 31 cm^{-1}. Thus, the experimental data submitted for IF analysis sample about four times more mono-energetic components near the lower energy observation limit than near $D_0(NO_2)$. This results in a much coarser sampling of the energies above 20,000 cm^{-1} than we desire. Ideally, we would prefer to reverse this trend and oversample the energies above 20,000 cm^{-1}, since we expect a higher density of states at these energies, hence more possible emitters per cm^{-1} than at lower energies.

This problem is compounded for Reaction (1) because the $P(E_{int})$ distributions are concentrated above 20,000 cm^{-1}. A doubling in resolution doubles the number of mono-energetic components available to the fitting algorithm at these critical energies, and allows the analysis to obtain increasingly smaller sum errors. The lower resolution spectra are unable to adequately optimize the weighting of the high energy NO_2^* components because of this undersampling and the result is a much broader distribution of high energy components required to minimize the sum error. Note that despite the spread in sum error values for the different resolution subsets, the optimized fits

constantly reproduce the same $P(E_{int})$ contour. The constancy of the $P(E_{int})$ distributions is further underlined by a comparison of the statistical measures of each distribution.

Weighting Functions Test:

We find that within the errors of the IF method no weighting function systematically outperforms the others, they all produce comparable sum errors and $P(E_{int})$ contours. Computationally there are some marked differences which should be noted. The Gaussian function requires no M parameter as long as the thermodynamic threshold for the process creating the NO_2^* ensemble is above $D_0(NO_2)$. Optimization of the fitting parameters for this function is computationally efficient and there is an analytic solution to the rotational energy convolution integral required for the coefficient to population transformation[4]. The intuitive distribution of coefficients from this function also contributes to making it the easiest to use, but also the least flexible of the weighting functions. There also exists an analytic solution to the biexponential function rotational energy integral, but this function has an extreme sensitivity to the M parameter[5], making its computational efficiency very low. The gamma kernel is the most flexible of the three weighting functions presented here, but its rotational energy integral must be evaluated numerically. It requires an M parameter, but optimizes much more efficiently than the biexponential function. The gamma kernel weighting function is probably the best compromise of computational efficiency and fitting ability.

M Variation:

Tables IV-VII show that the biexponential and gamma kernel weighting functions display a moderate degree of sensitivity to the M parameter. The M values for these tests were constrained to the 25,000 to 27,000 cm^{-1} range for this test. This range was chosen to coincide with reasonable values of θ, the maximum energy available to the NO_2^* emitters. All of the reported activation energies for R1 are *negative* and on the order of 1 to 2 kcal/mole (E_a = -350 to -750 cm^{-1}) [24]. If we assume a barrier-less inverse predissociation, then this indicates that the nascent energy of the NO_2^{**} complex is 25,500 - 26,000 cm^{-1}. Tests varying M over much larger energy ranges showed that the optimized fits still had M values in the 25,000 - 27,000 range. This seems to indicate that variation of M over the small range of physically anticipated threshold energies is well handled by the IF model. Additionally, the sum error values do not indicate a preferred threshold energy, although fits with M = 25,000 have systematically higher sum error values than do fits with M = 26,000 or 27,000.

1.5.B Comparison to Other Experimental Results

The NO + O recombination reaction exhibits a complicated pressure dependence[24]. At pressures below ~1 millitorr, the reaction is bimolecular and the only available relaxation mechanism is radiative. At pressures between 1 millitorr and 1000

millitorr, the reaction displays an M gas dependent termolecular rate. The reaction essentially reaches its infinite pressure limit when total pressures are above ~1000 millitorr, and the rate expression again becomes bimolecular. The spectral distribution of NO_2^* emission from this reaction changes in conjunction with the total reaction pressure[23,25]. The I(λ) distribution possesses proportionately more emission intensity at wavelengths shorter than 450nm (energies greater than 24,000 cm^{-1}) under reaction conditions in which the radiative relaxation mechanism dominates. With increasing contributions from the collisional relaxation mechanism (increasing M gas pressure), the I(λ) distribution red shifts, until the reaction pressures reach 1000 millitorr. At this point the asymptotic limit of the reaction rate has been reached, and the I(λ) distribution then remains constant with further increases in pressure.

It has been concluded that the overall reaction scheme

$$NO + O + M \rightarrow NO_2 + M + h\nu \qquad (R1')$$

possesses a mechanism consisting of the production of a collision complex followed by competition between redissociation, and stabilization via either collisional or radiative paths

$$NO + O \rightarrow NO_2^{**} \qquad K_c \rightleftarrows k_1/k_{-1} \qquad (M1,M-1)$$

$$NO_2^{**} + M \rightarrow NO_2^* + M \qquad k_c \qquad (M2)$$

$$NO_2^* + M \rightarrow NO_2 + M \qquad k_c' \qquad (M2')$$

$$NO_2^{**} \rightarrow NO_2 + h\nu \qquad k_r \qquad (M3)$$

$$NO_2^* \rightarrow NO_2 + h\nu \qquad k_r' \qquad (M3')$$

where NO_2^{**} indicates a short lived species with internal energy larger than $D_0(NO_2)$ and NO_2^* denotes an internal energy below $D_0(NO_2)$ but sufficient to fluoresce. The collisional stabilization mechanism is at least 10^6 times more effective than the radiative mechanism and Kaufman[25] has concluded that the rate is best expressed as 90% collisional/10% radiative. Step ladder models[23,25,26] have had great success in predicting the emission profiles based on the NO_2^{**} collision complex undergoing a series of vibrational energy transfer collisions prior to emission. Becker et al.[23] found a collisional deactivation rate (M2 and M2′) of 2×10^{-10} cm^3 molecule^{-1} s^{-1} and an average transfer of ~ 800 cm^{-1} per collision.

The complicated pressure dependence of R1 and its implications on the NO_2^* $P(E_{int})$ distributions are elucidated by a steady-state treatment of the Becker reaction mechanism. In this derivation we assume the following approximate rates

$$k_1 \approx 10^{-10} \text{ cm}^3 \text{ molecule}^{-1} \text{ s}^{-1}$$

$$k_{-1} \approx 10^{10} \text{ s}^{-1}$$

$$k_r \approx 10^5 \text{ s}^{-1}$$

$$k_r' \approx 10^5 \text{ s}^{-1}$$

$$k_c \approx 10^{-9}\ cm^3\ molecule^{-1}\ s^{-1}$$

$$k_c' \approx 10^{-10}\ cm^3\ molecule^{-1}\ s^{-1}$$

The rates k_1,k_c, and k_c' are approximately gas kinetic with k_c increased to compensate for the increased facility of deactivating collisions from the unstable NO_2^{**} collision complex. Both radiative relaxation rates, k_r and k_r', correspond to lifetimes of 10μs which is correct for NO_2^* to within a factor of 3 at these rovibronic excitation energies[5].

We note that whenever $k_1 >> k_r, k_r', k_c[M]$, or $k_c'[M]$ we may introduce the steady-state approximation. This indicates a pressure dependent competition between k_r,k_r',$k_c[M]$, and $k_c'[M]$ acting on the small concentration of NO_2^{**}.

$$I_{OBS} = k_r [NO_2^{**}] + k_r' [NO_2^*] \tag{4}$$

$$\frac{d\ [NO_2^{**}]}{dt} = k_1 [NO]\ [O] - (k_{-1} + k_r + k_c [M])\ [NO_2^{**}] \tag{5}$$

$$\frac{d\ [NO_2^{**}]}{dt} = 0 \quad at\ steady\ state \tag{6}$$

$$[NO_2^{**}] = \frac{k_1 [NO] [O]}{k_{-1} + k_r + k_c[M]} = \frac{k_1 [NO] [O]}{k_{-1}} \quad since\ k_{-1} > k_r\ ,\ k_c[M] \tag{7}$$

$$\frac{d\ [NO_2^*]}{dt} = k_c[M]\ [NO_2^{**}] - (k_r' + k_c'[M])\ [NO_2^*] \tag{8}$$

$$\frac{d\ [NO_2^*]}{dt} = 0 \quad at\ steady\ state \tag{9}$$

$$[NO_2^*] = [NO_2^{**}]\left(\frac{k_c[M]}{k_r' + k_c'[M]}\right) = \frac{k_1 [NO]\ [O]}{k_{-1}}\ \frac{k_c[M]}{k_r' + k_c'[M]} \tag{10}$$

Collecting terms from $[NO_2^{**}]$ and $[NO_2^*]$ from Equations (7) and (10), Equation (4) becomes

$$I_{OBS} = k_1 [NO]\ [O]\left(\frac{k_r}{k_{-1}} + \frac{k_r'}{k_{-1}}\ \frac{k_c[M]}{k_r' + k_c'[M]}\right) \tag{11}$$

which displays the total pressure dependence of R1′. In the limiting case as [M] → 0, Equation (11) simplifies to produce the second order radiative relaxation rate

$$I_{OBS} = \frac{k_1 k_r}{k_{-1}} [NO]\ [O] = K_e k_r [NO]\ [O] = I_0 \tag{12}$$

When the third body collision gas has a small but non-negligible concentration ([M] ~ 10^{13} molecules cm^3), $k_c'[M] << k_r'$ and the reaction has the following complicated third order rate

$$I_{OBS} = k_1 [NO] [O] \left(\frac{k_r + k_c [M]}{k_{-1}} \right) = I_0 + \frac{k_1 k_c}{k_{-1}} [NO] [O] [M] \qquad (13)$$

which contains the second order radiative relaxation rate, I_0, and a pressure dependent third order contribution. At the high pressure limit ([M] ~ 10^{17} molecules cm^3) $k_r'[M] >> k_c'$ and the rate expression again assumes a second order form

$$I_{OBS} = k_1 [NO] [O] \left(\frac{k_r}{k_{-1}} + \frac{k_r' k_c}{k_{-1} k_c'} \right) = I_0 + K_e \frac{k_c}{k_c'} k_r' [NO] [O] \qquad (14)$$

which has second order contributions from both the radiative relaxation rate and the collisional relaxation rate and my be re-expressed as

$$I_{OBS} = \left(K_e k_r + K_e \frac{k_c}{k_c'} k_r'\right) [NO]\ [O] \qquad (15)$$

Literature values for the derived rates are

$k_0 = K_e k_r = 4.2 \times 10^{-18}$ cm^3 molecule^{-1} s^{-1} [Ref. 23]

$k_{low}^{300} = K_e k_c = 9.0 \times 10^{-32}$ cm^6 molecule^{-2} s^{-1} [Ref. 24]

$k_{inf}^{300} = (K_e k_r + K_e k_r' k_c / k_c') = 3.0 \times 10^{-11}$ cm^3 molecule^{-1} s^{-1} [Ref. 24]

The results of the IF analysis for the BRADBURN, VANPEE, and PAULSEN data sets agrees very well with the 90% collisional/10% radiative stabilization mechanism. The populations determined for the high pressure limit of R1 from these data sets indicate that the majority of the NO_2^* emission is from an ensemble whose average energy is about 22,000 cm^{-1}. Assuming that the Becker energy transfer value of 800 cm^{-1} per collision is correct and that the NO_2^{**} complex is initially formed with 26,000 cm^{-1} of rovibronic energy, our results indicate that the average NO_2^{**} collision complex undergoes 5 deactivating collisions prior to emission. The population distributions also suggest that the minimal internal energy possessed by any emitting NO_2 molecules is ~18,000 cm^{-1}, or that the maximum number of collisions prior to emission is 10 - 12. The NO_2^* $P(E_{int})$ distributions also indicate that the purely radiative stabilization mechanism contributes substantially to the emission profile, since all of the populations are sharply peaked at $D_0(NO_2)$. Collisional deactivation channels

corresponding to only 2 or 3 energy transfers must also be important.

It is very interesting to note that all of the NO + O recombination I(λ) analyzed produce NO_2^* $P(E_{int})$ distributions are highly concentrated at energies above 20,000 cm^{-1} even though the emission profile extends continuously from 25,000 to 5000 cm^{-1}. The lack of significant contributions from NO_2^* molecules having energies less than 20,000 cm^{-1} indicates that the total spectral distribution reflects the Franck-Condon factors of an emitting ensemble whose internal energies are very close to D_0 rather than contributions from NO_2^* components with energies of all possible values between 25,000 and 5000 cm^{-1}.

This observation is supported by an experimental result obtained by Honma and Kajimoto[27]. These authors measured the NO_2^* emission from the crossed beams reaction of

$$O + (NO)_2 \rightarrow NO_2^* + NO \qquad \text{(R3)}$$

This reaction is a very interesting variation on R1. One of the NO molecules in the Van der Waals dimer participates in the O + NO reaction while the spectator NO acts as a built in third-body for "half-collisional" deactivation. The angular distribution of the emission intensity in this experiment is highly anisotropic, indicating that the collisional quenching mechanism dominates in NO_2^* formation. Furthermore, they found the same

angular distribution of the NO_2^* emission intensity for the total emission signal as for emission detected only at 420, 530, and 730nm. The indistinguishable angular distributions found for the wavelength resolved emission measurements means that the entire spectral distribution for this process arises from a single NO_2^* ensemble whose minimal internal energy is 23,800 cm^{-1} (corresponding to 420nm, the shortest wavelength tested). We expect that the NO + O recombination reaction produces a similar nascent NO_2^* ensemble, but that the multiple collision conditions intrinsically present in the high pressure experiments analyzed here broaden and red shift this ensemble.

Although the IF method provides no means for explicit identification of the NO_2 electronic configurations producing the emission in R1, there is strong evidence suggesting that the NO_2^* ensemble has $^2B_2$ character. Quack and Troe[28] derived rates for R1 using the statistical adiabatic channel model (SACM). The recombination was modelled as taking place entirely on the $^2A_1$ groundstate electronic surface and the calculated infinite pressure rate, 1.8×10^{-11}, agrees well with the experimental value, 3.0×10^{-11}. Smith[29] extended Quack and Troe's work by calculating the SACM contributions to the recombination reaction rate from all four of the low lying NO_2 doublet electronic surfaces. The spectroscopic parameters required for this study were taken from the *ab initio* calculations of Gillispie[12]. Inclusion of the excited state channels in R1 increases the calculated low pressure limit of k by a factor of 1.7 to 3.64×10^{-32} (compared to 9×10^{-32}) and k_{inf} by a factor of 2.9 to 5.34×10^{-11} (compared to 3.0×10^{-11}). Including only the rates calculated for the $^2A_1$ and $^2B_2$ NO_2 surfaces leads to values

of $k_0 = 3.26 \times 10^{-32}$ cm^6 molecule^{-2} s^{-1} and $k_{inf} = 3.52 \times 10^{-11}$ cm^3 molecule^{-1} s^{-1}. We note that the $^2A_1$ and $^2B_2$ contributions constitute 90% of the calculated radiative recombination rate, in accord with our expectations that excited electronic configurations are necessary for a complete description of the process.

1.6 CONCLUSIONS

We have applied the IF analysis method to the NO_2^* spectral distribution produced in the NO + O recombination reaction. The $P(E_{int})$ distributions derived for the recombination show that the fluorescing NO_2 ensemble has an internal energy sharply peaked at D_0 and having negligible contributions from energies less than 20,000 cm^{-1}, despite the fact that the emission peaks at 17,500 cm^{-1} and extends past 5000 cm^{-1}. Such an energy distribution mirrors the large exothermicity of the reaction. The average NO_2^* emitter undergoes 5 - 10 deactivating collisions before fluorescing when the reaction proceeds at pressures above 1000 millitorr.

An extensive battery of tests was carried out to evaluate the performance of the IF method under more rigorous standards than have previously been applied. The main result of these studies is that the method can readily be extrapolated to deal with emission spectra extending to 9000 cm^{-1}, but further extrapolation begins to suffer from degraded performance. An important aspect of this viewing range test is that the NO_2^* $P(E_{int})$ distributions derived for data sets which only extend to 12,500 cm^{-1} (the useful red limit

for most PMTs) are probably somewhat distorted. For analysis of the data used in this study, it was found that the extension of the red portion of the spectrum improved the fitting residuals and produced a blue shift in the overall population, despite the large energy difference in the energy of the population maximum and the lower energy limits. We also found that energies above 22,000 cm^{-1} are inadequately sampled by a constant wavelength interval of 2nm across the observation window. This results in a slight overweighting of the corresponding population distributions relative to the $P(E_{int})$ derived for "more resolved" spectra. The amount of distortion produced by our coarse wavelength grid and limited long wavelength coverage may be judged by the difference between the set of curves in Figures 4 (1nm resolution) and 5 (2nm resolution).

REFERENCES

[1] B.Y. Oh, W.N. Sisk, A.T. Young, and H.S. Johnston. J. Chem. Phys. **85** 7146 (1986).

[2] B.Y. Oh. Ph.D. Thesis. Department of Chemistry, University of California, Berkeley. 1988.

[3] W.N Sisk. Ph.D. Thesis. Department of Chemistry, University of California, Berkeley. 1990.

[4] H.S. Johnston, C.E. Miller, B.Y. Oh, K.O. Patten, and W.N. Sisk. Manuscript in preparation.

[5] K.O. Patten, Jr., Ph.D. Thesis, Department of Chemistry, University of California, Berkeley, 1991.

[6] G.R. Bradburn and H.V. Levelenfield, J. Phys. Chem. **92**, 5266 (1988).

[7] D.L. Hsu, D.L. Monts, R.N. Zare. Spectral Atlas of Nitrogen Dioxide. (New York: Academic Press, 1978).

[8] G. Persch, E. Mehdizadeh, W. Demtröder, Th. Zimmermann, H. Köppel, and L.S. Cedarbaum. Ber. Bunsenges. Phys. Chem. 92 312 (1988) and references therein.

[9] J.L. Hardiwck, J. Mol. Spec. **109**, 85 (1985).

[10] K.K. Lehman and S.L. Coy, J. Chem. Phys. **83**, 3290 (1985).

[11] S.L. Coy, K.K. Lehman, and F.C. DeLucia, J. Chem. Phys. **85**, 4297 (1986).

[12] G.D. Gillispie, A.U. Khan, A.C. Wahl, R.P. Hosteny, and M. Krauss, J. Chem. Phys. **63**, 3425 (1975); G.D. Gillispie and A.U. Khan, J. Chem. Phys. **65**, 1624 (1976).

[13] C.F. Jackels and E.R. Davidson, J. Chem. Phys. **64**, 2908 (1976); C.F. Jackels and E.R. Davidson, J. Chem. Phys. **65**, 2941 (1976).

[14] C.P. Blahous III, B.F. Yates, Y. Xie, and H.F. Schaefer III, J. Chem. Phys. **93**, 8105 (1990); Y. Xie, R.D. Davy, B.F. Yates, C.P. Blahous III, Y. Yamaguchi, and H.F. Schaefer III, Chem. Phys. **135**, 179 (1989).

[15] G. Hirsch and R.J. Buenker, Can. J. Chem. **63**, 1542 (1985); G. Hirsch, R.J. Buenker, and C. Petrongolo, Mol. Phys. **70**, 835 (1990).

[16] R.E. Smalley, L. Wharton, and D.H. Levy. J. Chem. Phys. **63** 4977 (1975).

[17] M. Vanpee, K.D. Hill, and W.R Kineyko, AIAA J. **9**, 135 (1971).

[18] The SPLINE and SPLINT routines from W.H. Press, B.P. Flannery, S.A. Teukolsky, and W.T. Vetterling, Numerical Recipes: The Art of Scientific Computing. (Cambridge University Press: Cambridge, England, 1986) formed the basis for the interpolation code.

[19] D.E. Paulsen, W.F. Sheridan, and R.E. Huffman, J. Chem. Phys. **53**, 647 (1970).

[20] A. Fontijn, C.B. Meyer, and H.I. Schiff, J. Chem. Phys. **40**, 64 (1964).

[21] M. Sutoh, Y. Morioka, and M. Nakamura, J. Chem. Phys, **72**, 20 (1980).

[22] A.T. Stair and J.P. Kennealy, J. Chim. Phys. et Physico-Biol. **64**, 124 (1967).

[23] K.H. Becker, W. Groth, and D. Thran, Chem. Phys. Lett. **15**, 215 (1972).

[24] D.A. Baulch, R.A. Cox, R.F. Hampson, J.A. Kerr, J. Troe, and R.T. Watson, J. Phys. Chem. Ref. Dat. **9**, 295 (1980) and references therein.

[25] F. Kaufman in Chemiluminescence and Bioluminescence, M.J. Cormier ed., (New York: Plenum Press, 1973), p. 83.

[26] S.M. Adler-Golden, J. Phys. Chem **93**, 684 (1989); J. Phys. Chem. **93**, 691 (1989).

[27] K. Honma and O. Kajimoto, J. Chem. Phys. **86**, 5491 (1987).

[28] M. Quack and J. Troe, Ber. Bunsenges. Phys. Chem. **79**, 170 (1979).

[29] I.W.M. Smith, Int. J. Chem. Kin. **16**, 423 (1984).

Table I. Allowable observation ranges and resolutions for the subsets used in data analysis.

Range (nm)	Low Energy Limit (cm^{-1})	Resolution (nm)
380 - 820	12,250	1,2,4
380 - 1000	10,000	2,4
380 - 1125	9000	2,4
380 - 1275	8000	4
380 - 1675	6000	4

Table II. Descriptions of the BRADBURN Data subsets.

Set	Range (nm)	Lower Energy Observation Limit (cm^{-1})	Reso-lution (nm)	No. Points
C1X	390 - 785	12,740	1	395
A1X	375 - 825	12,250	2	225
A2X	375 - 999	10,000	2	312
A3X	375 - 1125	9,000	2	375
B1X	375 - 823	12,250	4	112
B2X	375 - 999	10,000	4	156
B3X	375 - 1123	9,000	4	190
B4X	375 - 1271	8,000	4	225
B5X	375 - 1371	7,300	4	250
B6X	375 - 1671	6,000	4	325

Table III. Optimized Gaussian weighting function parameters for the BRADBURN Data.

Set	μ	σ	Sum Error (10^{-5})	Total Error ($x10^{-5}$)	E_{ave} (cm^{-1})	E_{rms} (cm^{-1})	E_{sup} (cm^{-1})
C1X	35,264	6375	2.2204	44.186	21,676	21,855	25,125
A1X	27,349	4125	2.6845	40.268	21,933	22,072	25,125
A2X	40,215	7375	2.1013	37.117	21,505	21,731	25,125
A3X	54,707	9750	1.7851	34.568	21,334	21,603	25,125
B1X	25,420	3343.7	2.8474	30.125	22,104	22,219	25,125
B2X	30,024	5062.5	2.1230	26.516	21,730	21,911	25,125
B3X	34,326	6187.5	1.7716	24.420	21,563	21,782	25,125
B4X	56,035	10,000	1.7508	26.262	21,270	21,565	25,125
B5X	105860	15,500	1.7636	27.884	21,094	21,439	25,125
B6X	53,711	9750	2.2308	40.217	21,106	21,439	25,125

Table IV. Biexponential weighting function optimized fits to the BRADBURN Data subsets with resolution = 1 and 2nm.

Set	M x10^3	C_r	C_d	Sum Error x10^{-3}	Total Error x10^{-3}	E_{ave} (cm^{-1})	E_{max} (cm^{-1})	E_{map} (cm^{-1})
C1X	25	9.7656	2716.8	2.4830	49.412	21554	21756	25000
C1X	26	913.09	2609.4	2.4135	48.029	21654	21849	25125
C1X	27	2529.3	2406.2	2.3507	46.779	21656	21855	25125
A1X	25	568.85	2015.6	3.4307	51.461	22230	22367	24509
A1X	26	37500	1585.9	3.1814	47.721	22150	22289	24752
A1X	27	67500	1742.2	3.5013	52.520	22030	22190	25125
A2X	25	234.37	2375.0	2.2985	40.601	21737	21953	24752
A2X	26	1914.1	2203.1	2.2128	39.087	21736	21941	24875
A2X	27	35625	1843.7	2.1908	38.698	21728	21930	25125
A3X	25	106.20	2539.1	1.7541	33.968	21405	21681	24875
A3X	26	1093.7	2476.6	1.7316	33.532	21430	21699	25000
A3X	27	2187.5	2421.9	1.7322	33.544	21416	21683	25125

Table V. Biexponential weighting function optimized parameters for BRADBURN Data subsets with 4nm resolution.

Set	M x10^3	C_r	C_d	Sum Error x10^{-3}	Total Error x10^{-3}	E_{ave} (cm^{-1})	E_{mo} (cm^{-1})	E_{mp} (cm^{-1})
B1X	25	637.21	1968.7	3.5190	37.231	22233	22365	24390
B1X	26	60000	1585.9	3.3383	35.319	22160	22302	24875
B1X	27	57500	1765.6	3.7685	39.871	22032	22197	25125
B2X	25	388.18	2226.6	2.2571	28.191	21863	22053	24630
B2X	26	5293.0	1875	2.0997	26.225	21888	22067	24630
B2X	27	65000	1820.3	2.2511	28.116	21785	21986	25125
B3X	25	324.71	2293	1.8516	25.522	21712	21934	24630
B3X	26	2587.9	2109.4	1.7613	24.278	21732	21945	24875
B3X	27	53750	1843.7	1.8021	24.840	21679	21901	25125
B4X	25	151.37	2464.8	1.5605	23.408	21149	21448	24630
B4X	26	1372.1	2398.5	1.5499	23.249	21176	21474	24630
B4X	27	2939.5	2328.1	1.5732	23.598	21184	21482	25125
B5X	25	29.297	2554.7	1.5808	24.995	21032	21372	24875
B5X	26	1001	2531.2	1.5888	25.121	21011	21353	24630
B5X	27	1855.5	2507.8	1.6096	25.450	21017	21361	25125
B6X	25	231.93	2429.7	2.2783	41.073	20997	21335	24390
B6X	26	1669.9	2343.7	2.2481	40.528	21040	21371	24390
B6X	27	4882.8	2187.5	2.2393	40.370	21074	21397	25125

Table VI. Gamma kernel weighting function optimized parameters for subsets of the BRADBURN data with 1 and 2nm resolution.

Set	M $x10^3$	Y	N	Sum Error $x10^{-3}$	Total Error $x10^{-3}$	E_{ave} (cm^{-1})	E_{max} (cm^{-1})	E_{mp} (cm^{-1})
C1X	25	66.040	0.0250	2.4779	49.310	21585	21783	25000
C1X	26	820.08	0.3625	2.3404	46.574	21672	21862	25125
C1X	27	1328.1	0.6250	2.3178	46.124	21680	21868	25125
A1X	25	801.56	0.4297	2.9403	44.105	21982	22139	24691
A1X	26	1603.9	1.0000	2.9011	43.517	21979	22128	24691
A1X	27	2443.7	1.7188	2.9261	43.892	21992	22137	24813
A2X	25	465.62	0.2031	2.1645	38.110	21517	21751	24937
A2X	26	963.67	0.4532	2.0978	36.936	21511	21739	25062
A2X	27	1455.5	0.7188	2.1113	37.173	21505	21733	25062
A3X	25	349.41	0.1445	1.7434	33.761	21343	21614	25062
A3X	26	688.67	0.2969	1.7335	33.569	21322	21592	25062
A3X	27	1078.9	0.4844	1.7551	33.988	21327	21595	25062

Table VII. Gamma kernel weighting function optimized parameters for BRADBURN Data subsets having 4nm resolution.

Set	M $x10^3$	Y	N	Sum Error $x10^{-3}$	Total Error $x10^{-3}$	E_{ave} (cm^{-1})	E_{min} (cm^{-1})	E_{max} (cm^{-1})
B1X	25	847.27	0.4609	3.1417	33.239	22015	22171	24570
B1X	26	1763.7	1.1250	3.0078	31.823	22005	22152	24570
B1X	27	2606.2	1.9063	2.9483	21.193	22009	22152	24813
B2X	25	557.03	0.2500	2.1629	27.015	21573	21813	24813
B2X	26	1171.9	0.5781	2.1478	26.826	21554	21777	25062
B2X	27	1778.9	0.9375	2.1457	26.800	21552	21773	25062
B3X	25	450.39	0.1914	1.8114	24.968	21398	21664	25062
B3X	26	930.0	0.4219	1.8173	25.050	21376	21638	25062
B3X	27	1412.5	0.6719	1.8240	25.142	21371	21632	25062
B4X	25	137.7	0.0508	1.9417	29.126	20996	21345	25062
B4X	26	251.95	0.0938	1.9513	29.270	20976	21327	25062
B4X	27	374.41	0.1406	1.9559	29.339	20975	21325	25062
B6X	25	323.03	0.1328	2.2273	40.154	21030	21391	25062
B6X	26	675	0.2813	2.2292	40.188	21012	21370	25062
B6X	27	1019.5	0.4375	2.2308	40.217	21007	21363	25062

Table VIII. Descriptions of the subsets generated from the VANPEE data.

Set	Range (nm)	Lower Energy Observation Limit (cm^{-1})	Reso-lution (nm)	No. Points
A21	390 - 1190	9000	2	395
A22	390 - 1000	10,000	2	306
A23	390 - 910	11,000	2	261
A24	390 - 820	12,250	2	216
A41	390 - 1680	6000	4	320
A42	390 - 1430	7000	4	260
A43	390 - 1250	8000	4	215
A44	390 - 1110	9000	4	180
A45	390 - 1000	10,000	4	152
A46	390 - 910	11,000	4	130
A47	390 - 820	12,250	4	107

Table IX VANPEE NO + O Data: Gaussian Coefficient Function Optimized Fit Parameters

Set	μ	σ	Sum Error (10^{-3})	Total Error $x10^{-3}$	E_{ave} (cm^{-1})	E_{rms} (cm^{-1})	E_{max} (cm^{-1})
A21	39102	6375	2.1409	42.550	22197	22355	25125
A22	27026	3531.2	2.0902	36.564	22440	22540	25125
A23	26201	3218.7	2.5806	41.611	22492	22583	25125
A24	26870	3468.7	3.3254	48.873	22458	22556	25125
A41	23828	2000	5.4077	96.736	22719	22774	23696
A42	32393	4937.5	1.5889	25.620	22426	22554	25125
A43	58125	9000	1.9454	28.591	22264	22441	25125
A44	32666	5000	2.0303	27.239	22424	22552	25125
A45	27700	3687.5	2.1543	26.560	22536	22637	25125
A46	26792	3375	2.6601	330.330	22577	22670	25125
A47	27920	3750	3.4482	35.668	22540	22641	25125

Table X. Biexponential weighting function optimized parameters for the VANPEE data.

Set	M $x10^3$	C_r	C_d	Sum Error $x10^{-3}$	Total Error $x10^{-3}$	E_{ave} (cm^{-1})	E_{rms} (cm^{-1})	E_{mp} (cm^{-1})
A21	26	1513.7	1921.9	2.1041	41.818	22832	22954	25125
A22	26	43,750	1406.1	2.2761	39.815	23573	23629	25125
A23	26	45,000	1398.4	2.8794	46.429	23585	23640	25125
A24	26	33,750	1421.9	3.5522	52.206	23557	23613	25125
A41	25	20,000	1070.3	5.4869	98.153	23812	23842	24875
A42	26	6132.8	1531.2	1.6096	25.954	23461	23531	25125
A43	26	1098.6	1976.6	1.9026	27.962	22800	22934	25125
A44	26	2656.2	1703.1	2.0506	27.512	23219	23309	25125
A45	26	35,000	1390.6	2.3042	28.408	23656	23710	25125
A46	26	36,250	1382.8	2.8960	33.01	23667	23720	25125
A47	26	28,125	1406.2	3.6291	37.540	23639	23693	25125

Table XI VANPEE NO + O Data: Gamma Kernel Coefficient Function Optimized Fit Parameters and M Values

Set	M $x10^3$	Y	N	Sum Error $x10^{-3}$	Total Error $x10^{-3}$	E_{ave} (cm^{-1})	E_{max} (cm^{-1})	E_{mp} (cm^{-1})
A21	26	934.45	0.5500	2.1102	41.939	22345	22495	2515
A22	27	2467	2.2500	2.1978	38.446	22621	22719	24875
A23	27	2620.8	2.6000	2.7361	44.118	22685	22773	24752
A24	27	2413.3	2.1500	3.4891	51.279	22622	22719	24875
A41	27	3359.4	5.9000	5.4285	97.108	23001	23051	23923
A42	27	1932.4	1.4500	1.6006	25.809	22576	22697	25125
A43	25	296.63	0.1563	1.9092	28.059	22203	22365	2875
A44	27	1807.9	1.3000	2.0395	27.363	22559	22683	25125
A45	27	2354.7	2.1000	2.2535	27.783	22696	22794	24875
A46	27	2498.8	2.4000	2.8007	31.933	22749	22839	24875
A47	27	2208.3	1.8500	3.5908	37.144	22677	22778	25125

Table XII. PAULSEN data subsets.

Set	Range (nm)	Lower Energy Observation Limit (cm^{-1})	Reso-lution (nm)	No. Points
P11	390 - 785	12,740	1	395
P21	390 - 825	12,250	2	215
P41	390 - 823	12,250	4	108

Table XIII. Gaussian weighting function optimized parameters for the PAULSEN Data.

Set	μ	σ	Sum Error $x10^{-3}$	Total Error $x10^{-3}$	E_{ave} (cm^{-1})	E_{rms} (cm^{-1})	E_{mp} (cm^{-1})
A11	31401	6312.5	1.1808	23.468	20779	21014	25125
A21	26514	4468.7	1.8944	28.416	21210	21401	25125
A41	25225	3031.2	3.0721	32.945	22237	22424	24875

Table XIV. Paulsen Biexponential

Set	M $x10^3$	C_r	C_d	Sum Error $x10^{-3}$	Total Error $x10^{-3}$	E_{ave} (cm^{-1})	E_{rms} (cm^{-1})	E_{mp} (cm^{-1})
P11	25	313.72	3337.5	1.5213	30.235	21275	21507	25125
P11	26	1320.8	3137.5	1.3902	27.630	21460	21678	25125
P11	27	41113	2775	1.3002	25.841	21830	22020	25125
P21	25	642.09	2656.2	1.3951	20.456	21810	22002	25000
P21	26	42,500	1937.5	1.2573	18.436	22860	22971	25125
P21	27	67,500	2140.6	1.3301	19.503	22587	22721	25125
P41	25	2011.7	1675	3.4118	35.456	23278	23360	25125
P41	26	36,250	1550	3.3930	35.261	23447	23516	25125
P41	27	43,750	1712.5	3.5934	37.344	23227	23313	25125

Table XV. PAULSEN gamma kernel.

Set	M x10^3	Y	N	Sum Error x10^{-3}	Total Error x10^{-3}	E_{ave} (cm^{-1})	E_{rms} (cm^{-1})	E_{mp} (cm^{-1})
P11	25	647.22	0.2250	1.3772	27.371	20924	21165	24813
P11	26	1280.8	0.4938	1.3107	26.050	20930	21166	25000
P11	27	1944.8	0.8125	1.2811	25.461	20940	21174	25125
P21	25	1152.3	0.5546	2.1122	31.683	21306	21508	24330
P21	26	2015.6	1.1250	2.1008	31.512	21309	21504	24330
P21	27	2910.9	1.8281	2.0895	31.343	21319	21510	24330
P41	25	1076.4	0.7375	3.3561	34.878	22366	22483	24390
P41	26	1953.1	1.6000	3.2771	34.057	22413	22521	24390
P41	27	2883.8	2.7500	3.2342	33.611	22442	22545	24390

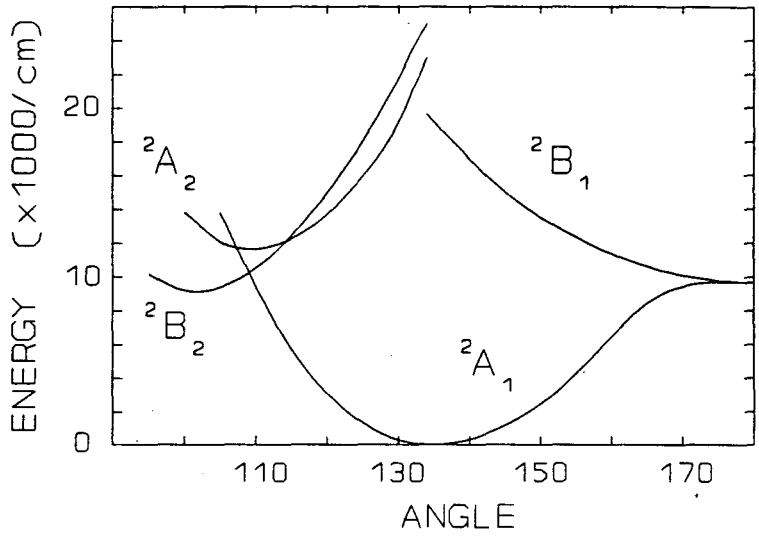

Figure 1. The low lying NO_2 potential energy surfaces after Gillispie et al. J. Chem. Phys. **63**, 3425 (1975).

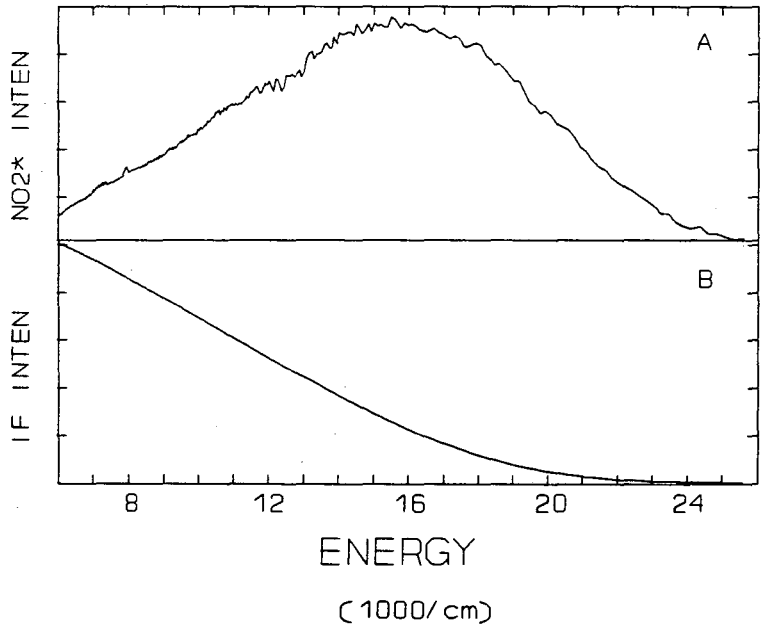

Figure 2. A). The BRADBURN NO_2^* spectral distribution from the NO + O recombination reaction. B). The corresponding mapping of the energy dependent integrated fluorescence intensity function.

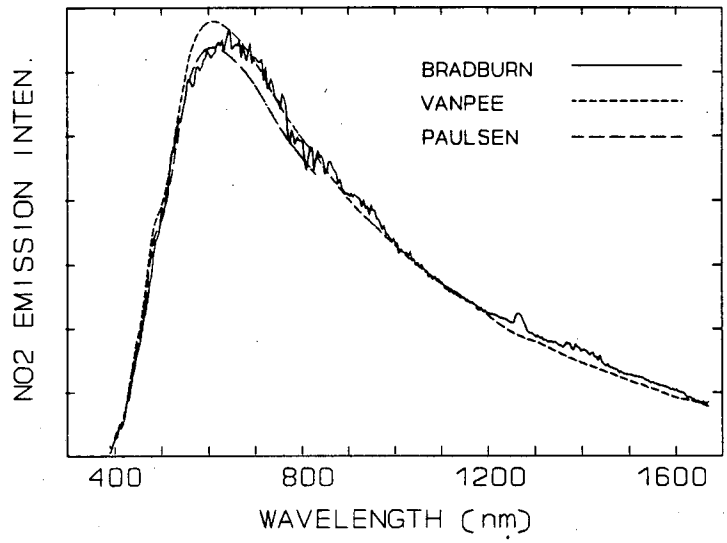

Figure 3. Measurements of the NO_2 I(λ) from the NO + O recombination reaction analyzed with the IF method. The spectra have been normalized for total emission intensity.

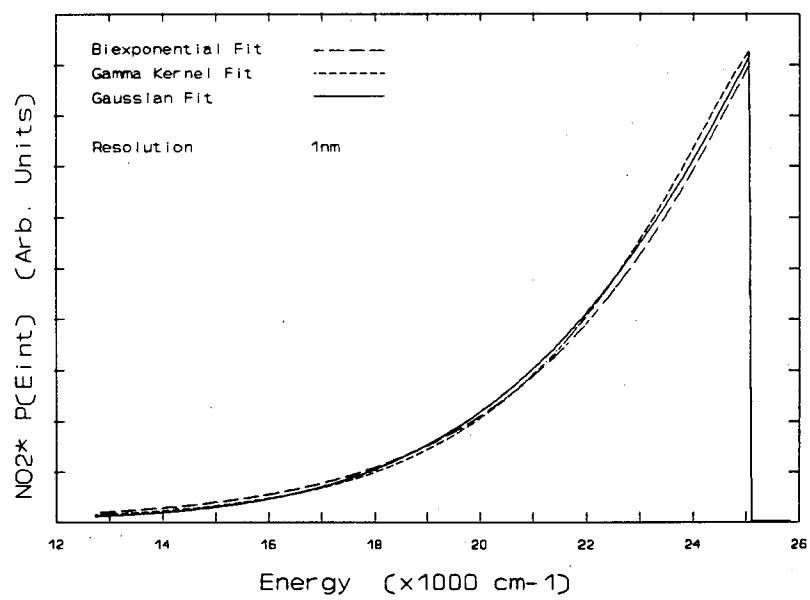

Figure 4 BRADBURN $P(E_{int})$ distributions: Resolution = 1nm; Low Energy Limit = 12,740 cm^{-1}.

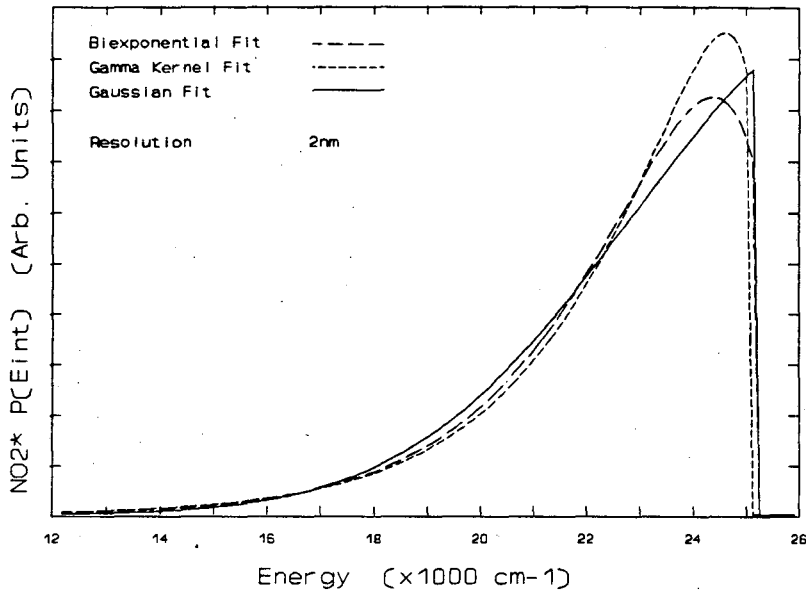

Figure 5 BRADBURN $P(E_{int})$ distributions: Resolution = 2nm; Low Energy Limit = 12,250 cm^{-1}.

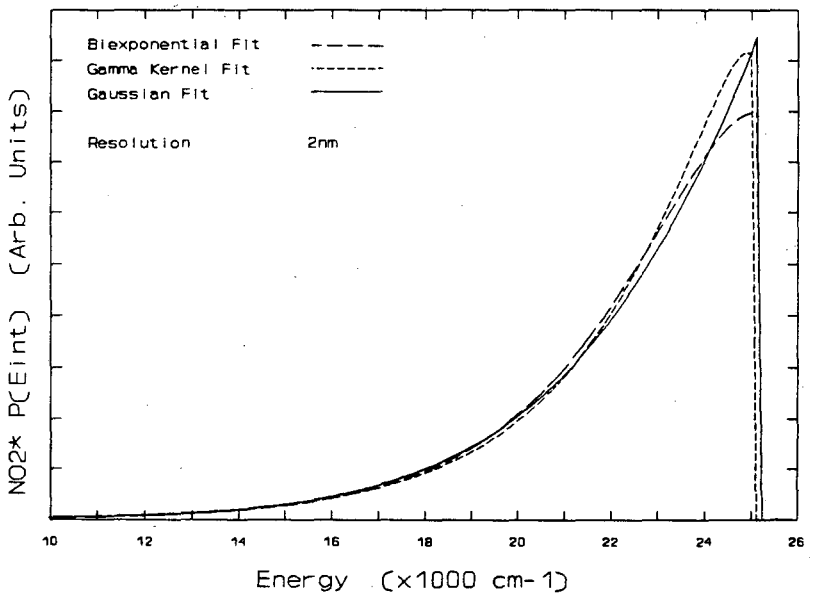

Figure 6 BRADBURN NO_2^* $P(E_{int})$ distributions: Resolution = 2nm; Low Energy Limit = 10,000 cm^{-1}.

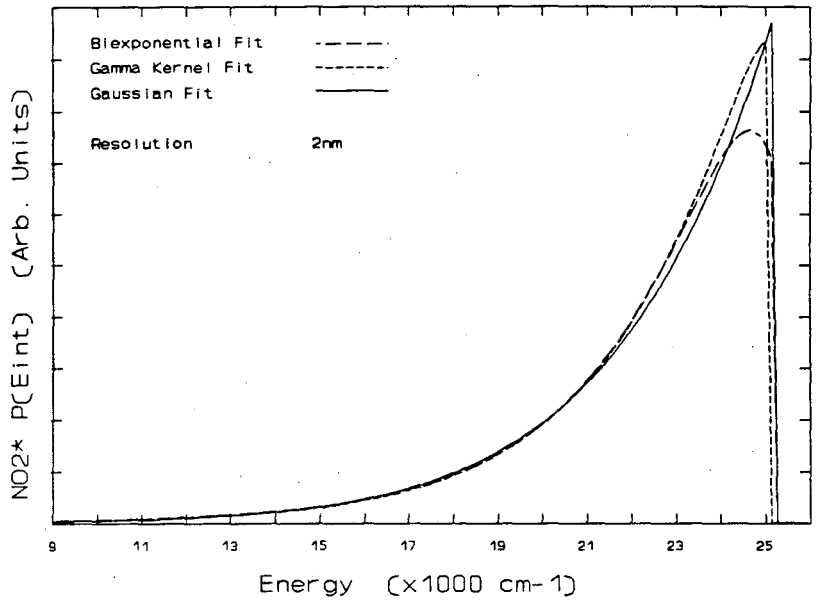

Figure 7 BRADBURN NO_2^* $P(E_{int})$ distributions: Resolution = 2nm; Low Energy Limit = 9000 cm^{-1}.

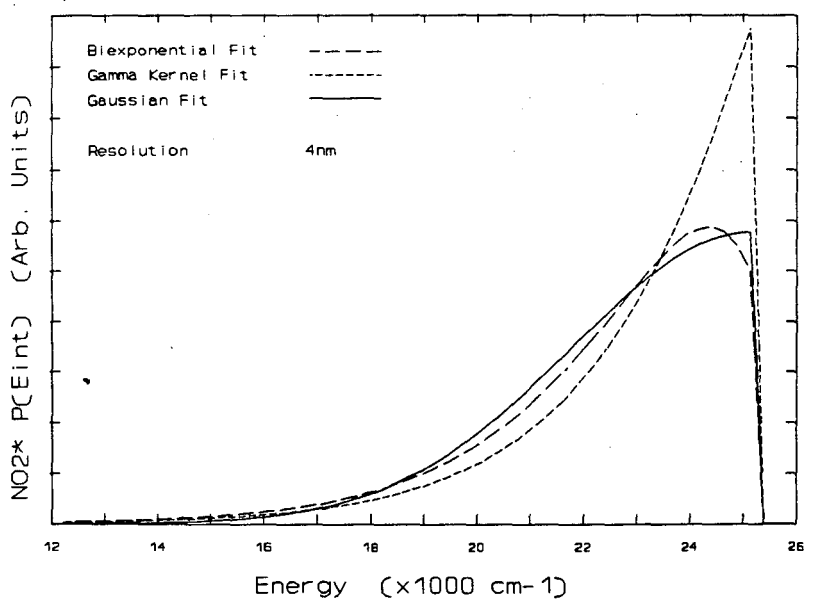

Figure 8 BRADBURN NO_2^* $P(E_{int})$ distributions: Resolution = 4nm; Low Energy Limit = 12,250 cm^{-1}.

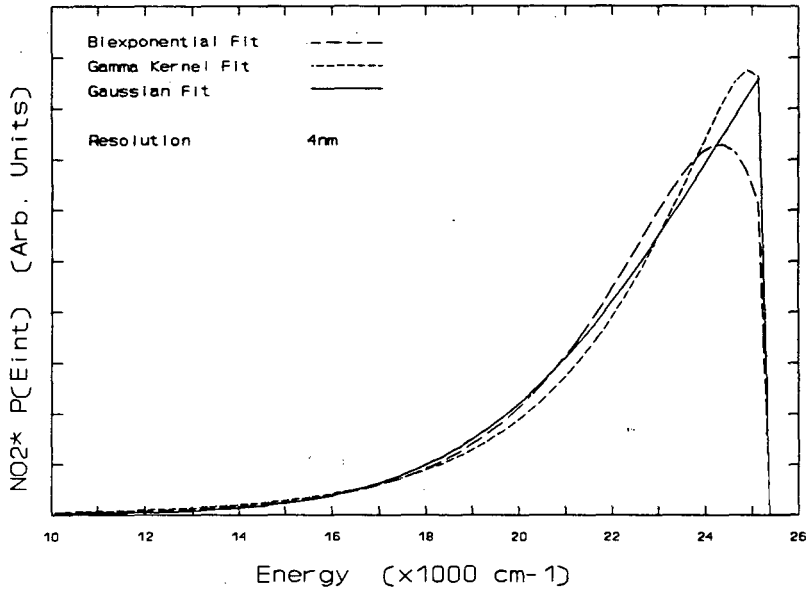

Figure 9 BRADBURN NO_2^* $P(E_{int})$ distributions: Resolution = 4nm; Low Energy Limit = 10,000 cm^{-1}.

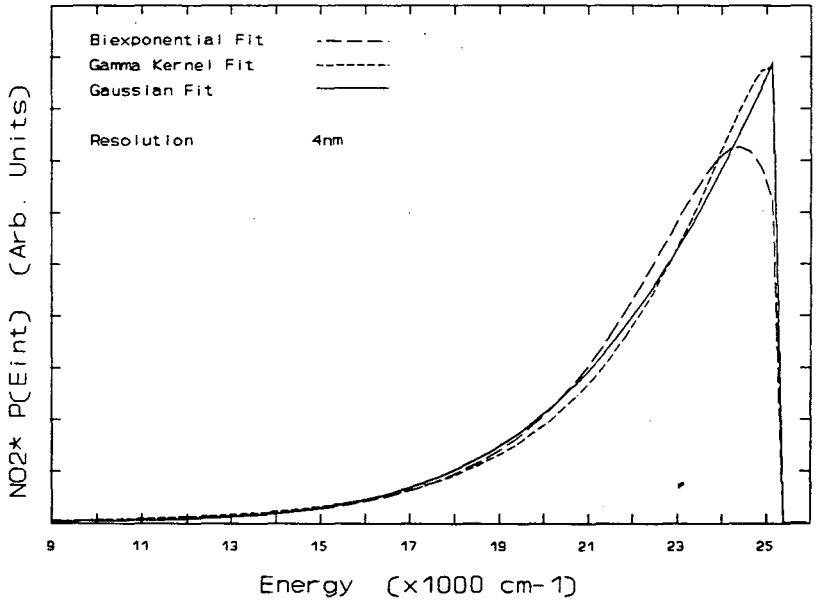

Figure 10 BRADBURN NO_2^* $P(E_{int})$ distributions: Resolution = 4nm; Low Energy Limit = 9000 cm^{-1}.

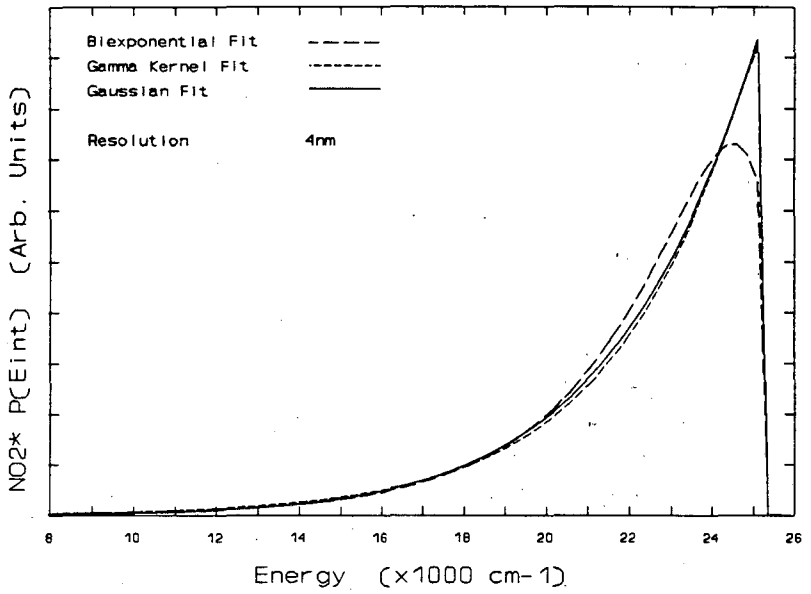

Figure 11BRADBURN NO_2^* $P(E_{int})$ distributions: Resolution = 4nm; low energy limit = 8000 cm^{-1}.

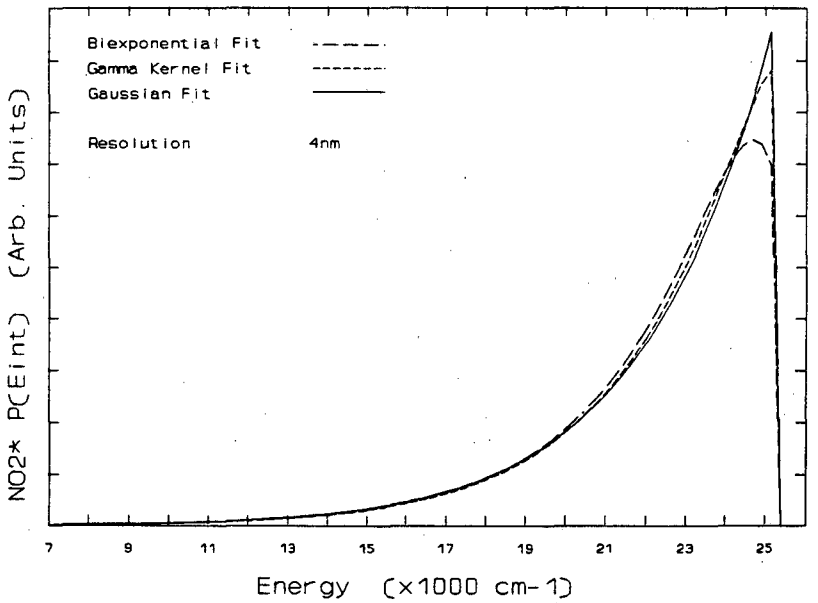

Figure 12 BRADBURN NO_2^* $P(E_{int})$ distributions: resolution = 4nm; low energy limit = 7000 cm^{-1}.

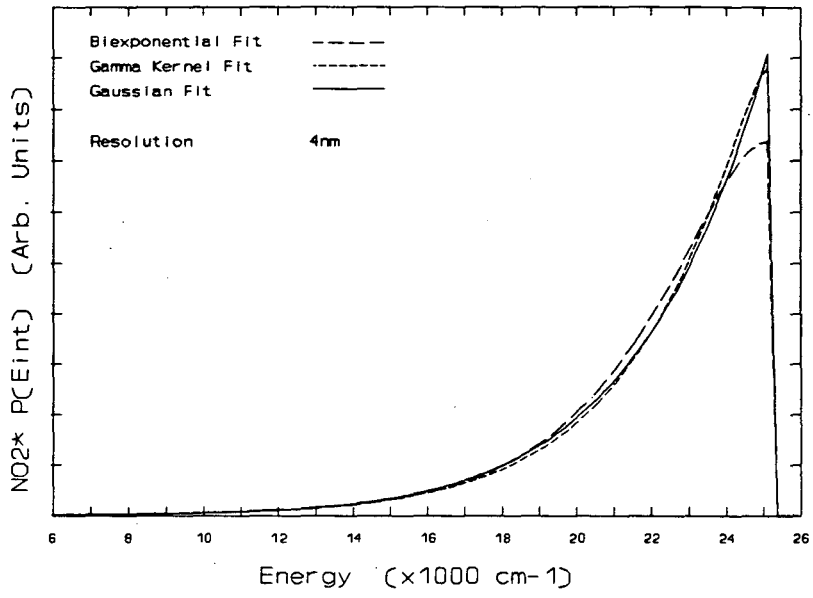

Figure 13 BRADBURN NO_2^* $P(E_{int})$ distributions: resolution = 4nm; low energy limit = 6000 cm^{-1}.

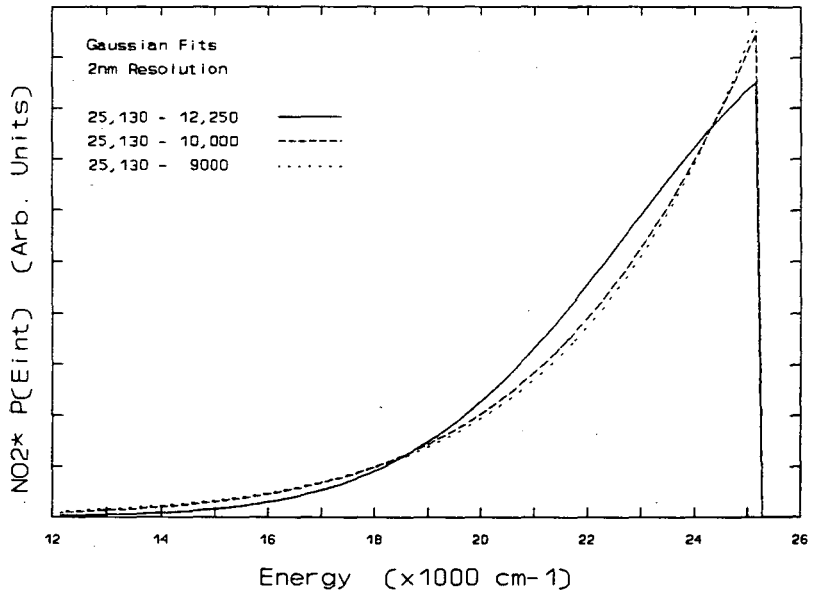

Figure 14 A comparison of all of the Gaussian weighting function fits for BRADBURN data subsets with 2nm resolution.

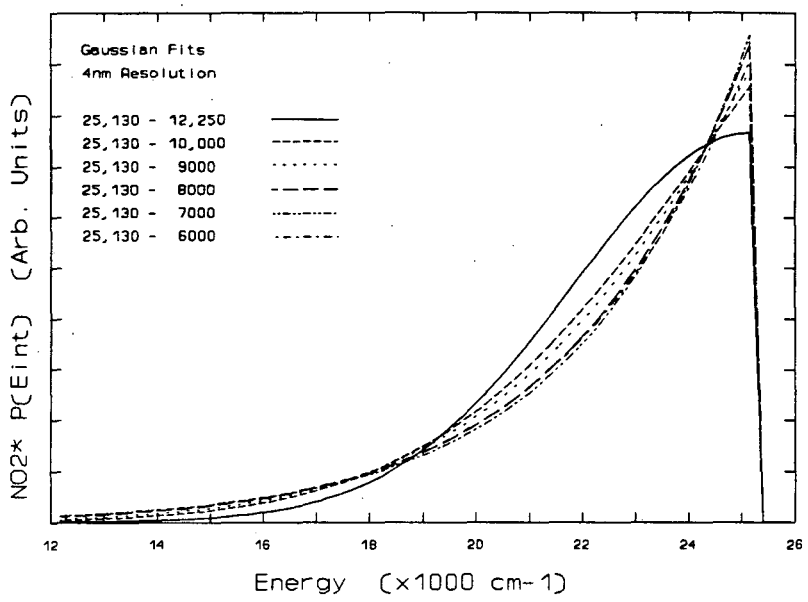

Figure 15 A comparison of all of the Gaussian weighting function fits for BRADBURN data subsets with 4nm resolution.

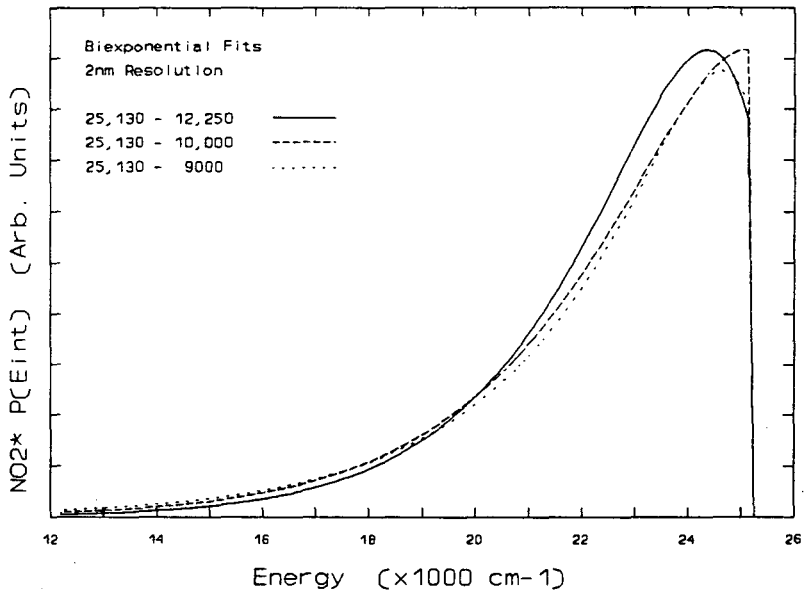

Figure 16 A comparison of all of the biexponential weighting function fits to the BRADBURN data subsets with 2nm resolution.

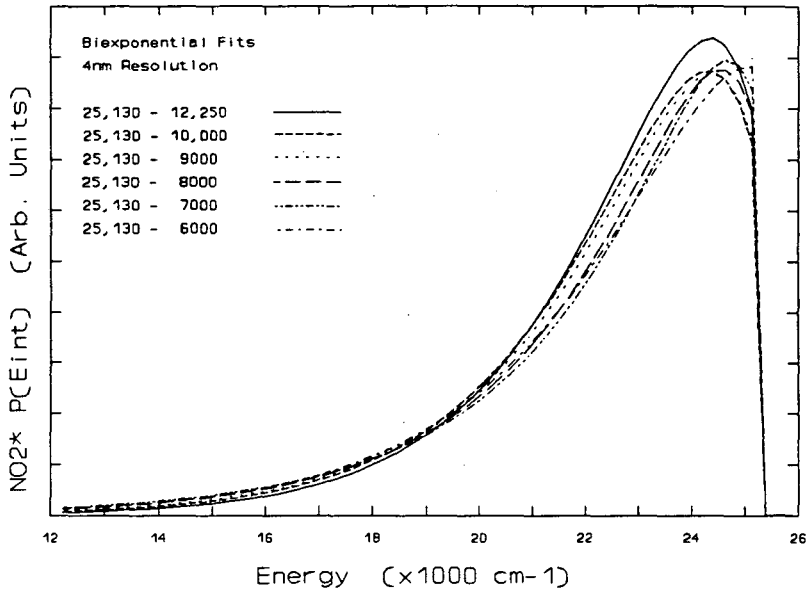

Figure 17 A comparison of all of the biexponential weighting function fits to BRADBURN data subsets with 4nm resolution.

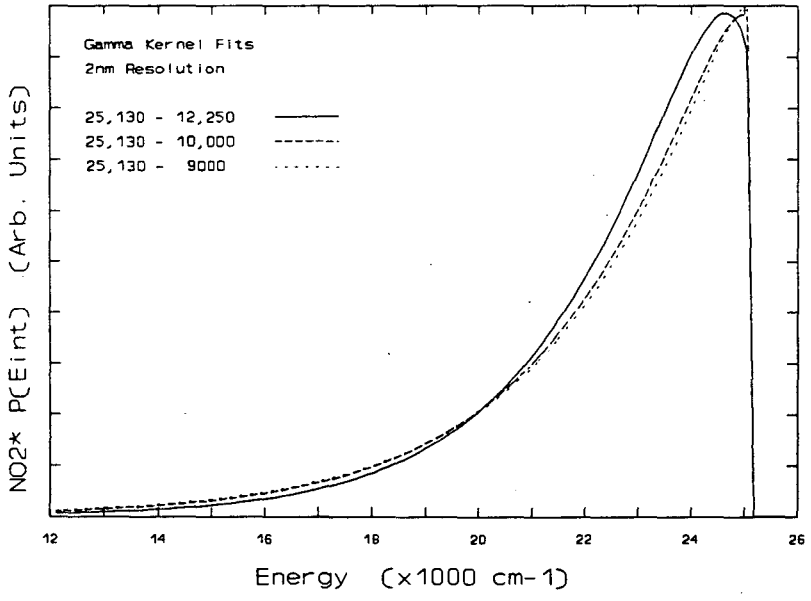

Figure 18 A comparison of all of the gamma kernel weighting function fits to BRADBURN data subsets with 2nm resolution.

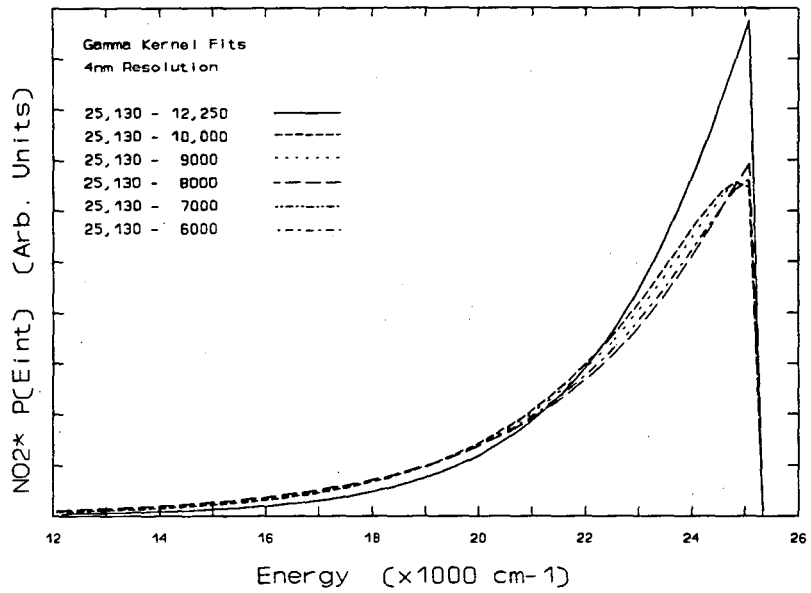

Figure 19 A comparison of all of the gamma kernel weighting function fits to BRADBURN data subsets with 4nm resolution.

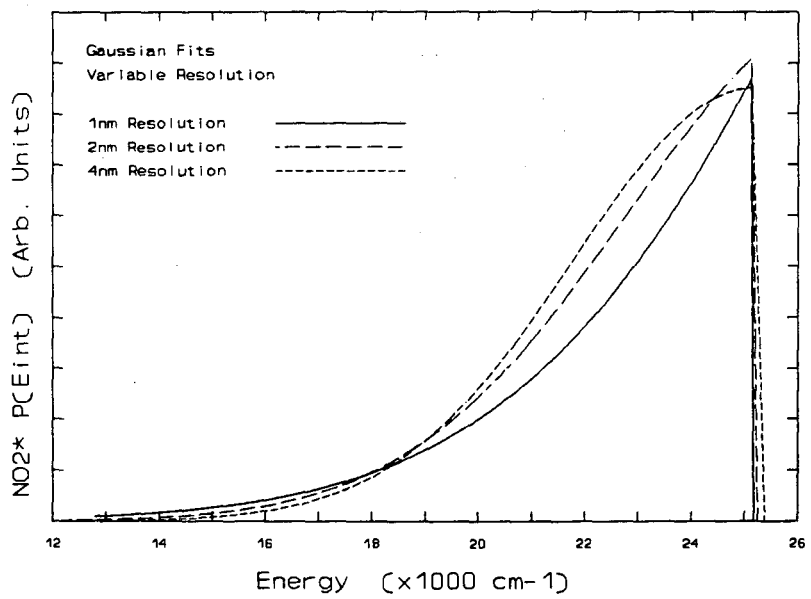

Figure 20. Resolution test of the BRADBURN data for the Gaussian weighting function and observation range extending to 12,250 cm^{-1}.

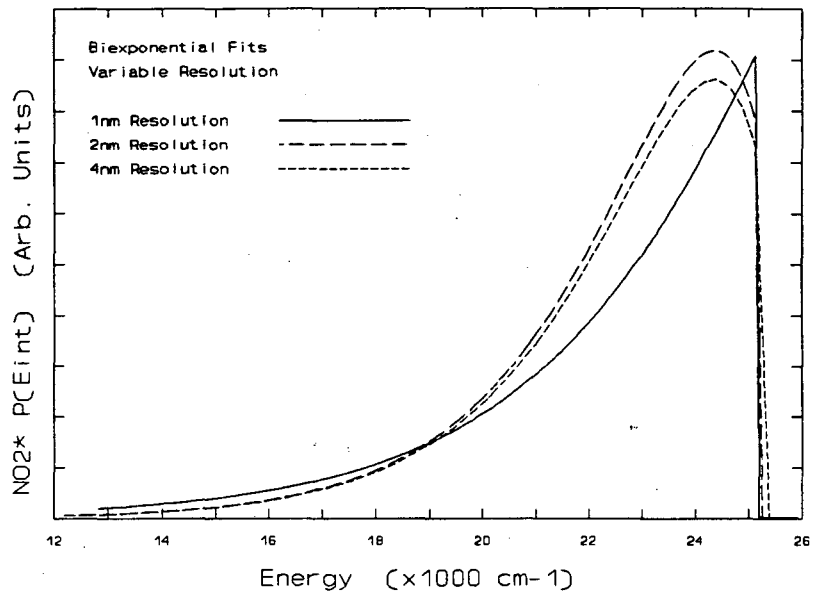

Figure 21. Resolution test of the BRADBURN data for the biexponential weighting function and observation range extending to 12,250 cm^{-1}.

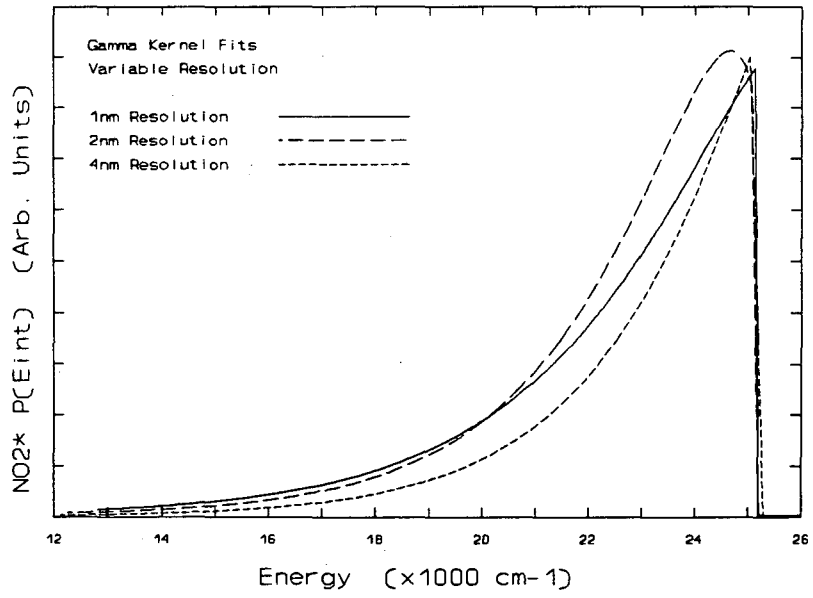

Figure 22. Resolution test of the BRADBURN data for the gamma kernel weighting function and observation range extending to 12,250 cm^{-1}.

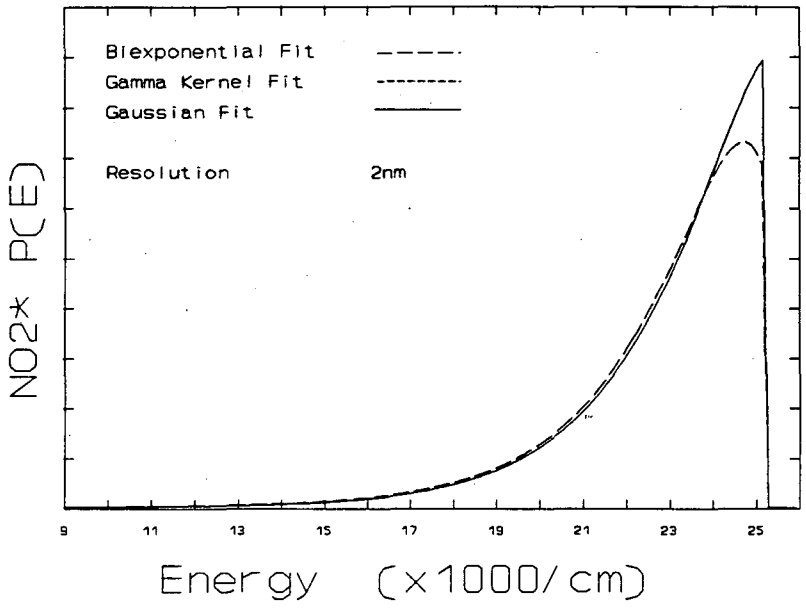

Figure 23 VANPEE NO_2^* $P(E_{int})$ distributions: resolution = 2nm; low energy limit = 9000 cm^{-1}.

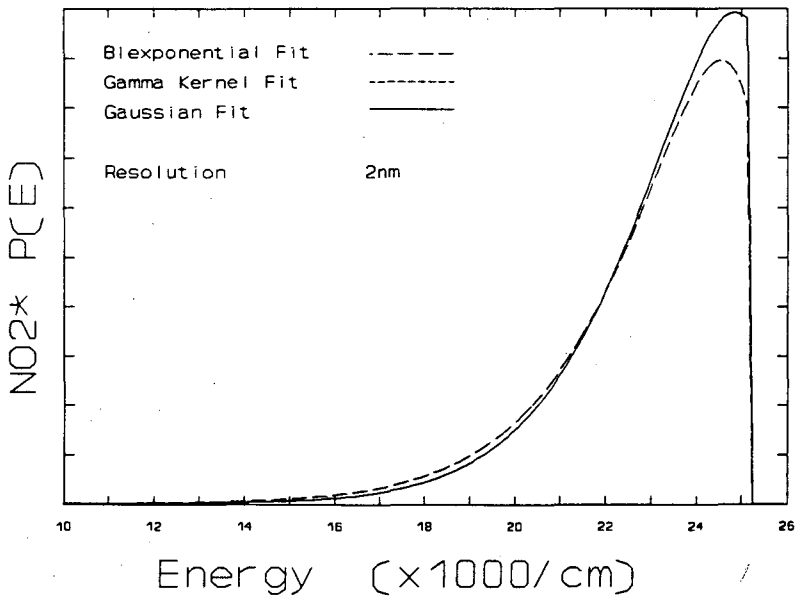

Figure 24 VANPEE NO_2^* $P(E_{int})$ distributions: resolution = 2nm; low energy limit = 10,000 cm^{-1}.

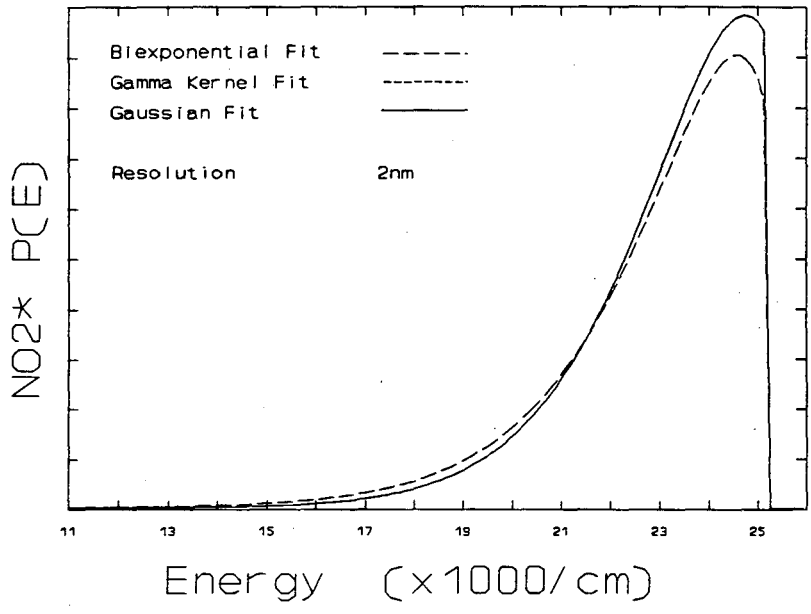

Figure 25 VANPEE NO_2^* $P(E_{int})$ distributions: resolution = 2nm; low energy limit = 11,000 cm^{-1}.

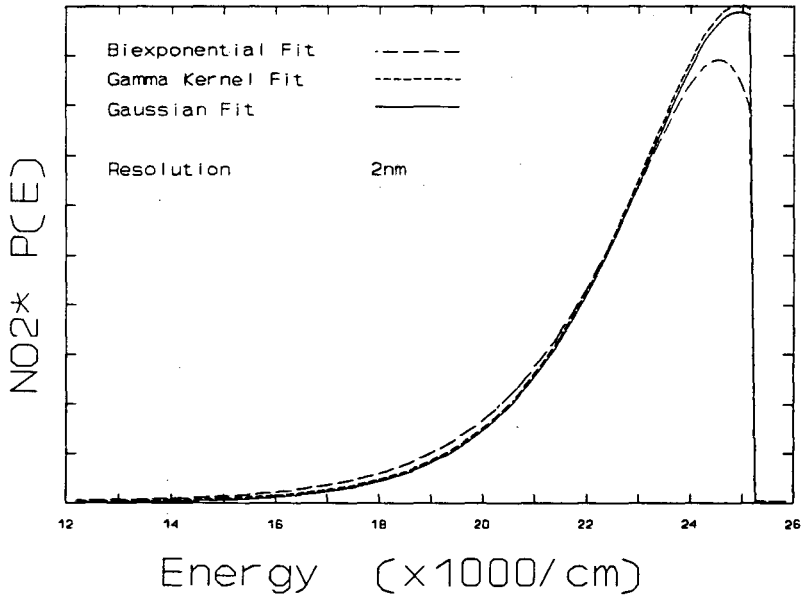

Figure 26 VANPEE NO_2^* $P(E_{int})$ distributions: resolution = 2nm; low energy limit = 12,250 cm^{-1}.

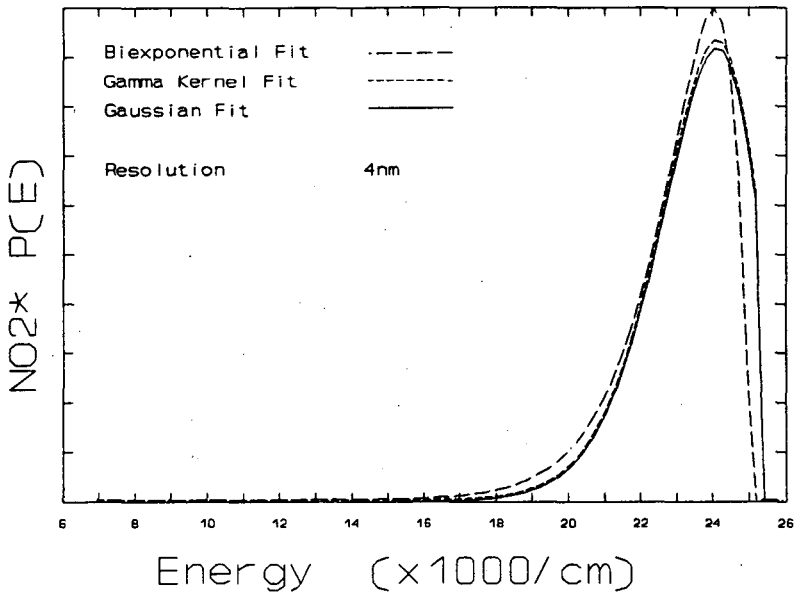

Figure 27 VANPEE NO_2^* $P(E_{int})$ distributions: resolution = 4nm; low energy limit = 6000 cm^{-1}.

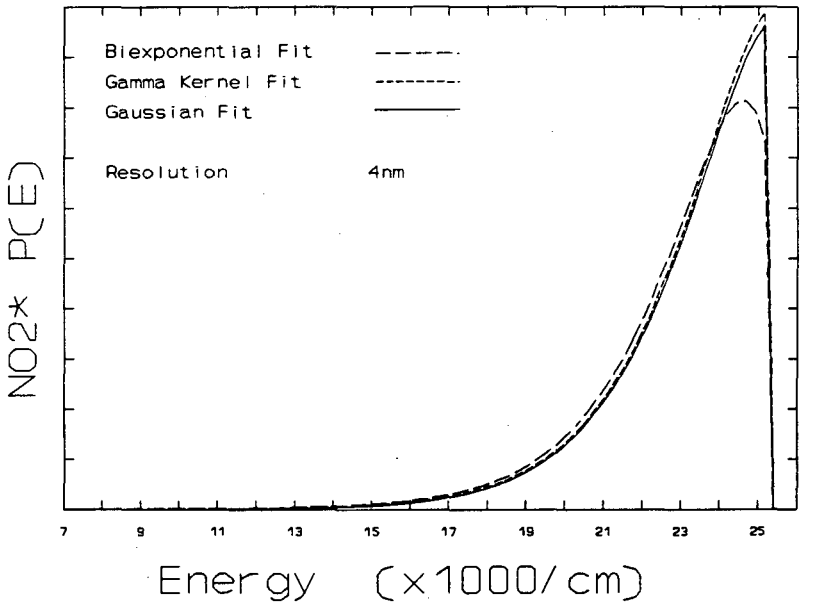

Figure 28 VANPEE NO_2^* $P(E_{int})$ distributions: resolution = 4nm; low energy limit = 7000 cm^{-1}.

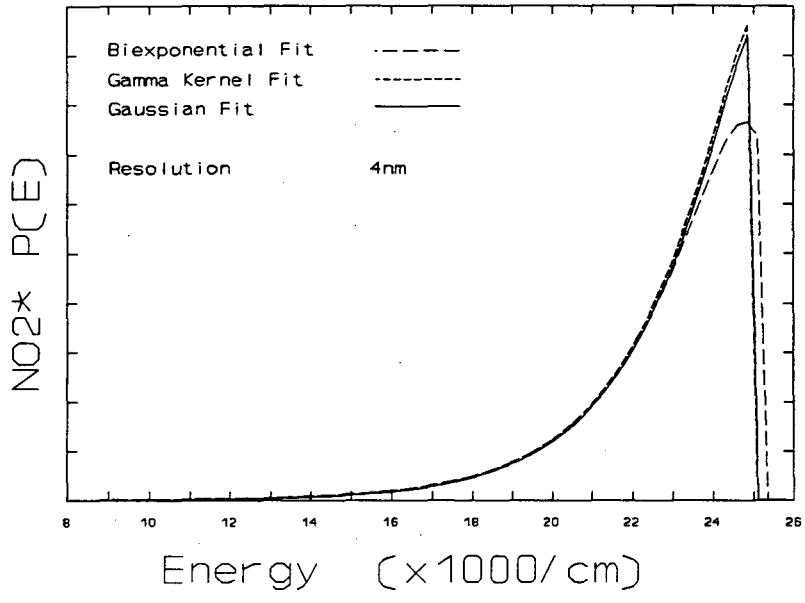

Figure 29 VANPEE NO_2^* $P(E_{int})$ distributions: resolution = 4nm; low energy limit = 8000 cm^{-1}.

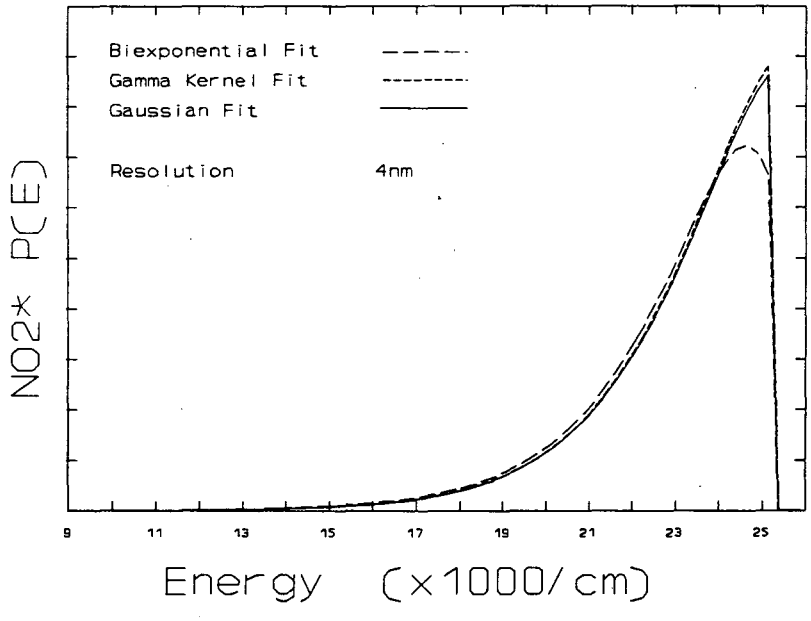

Figure 30 VANPEE NO_2^* $P(E_{int})$ distributions: resolution = 4nm; low energy limit = 9000 cm^{-1}.

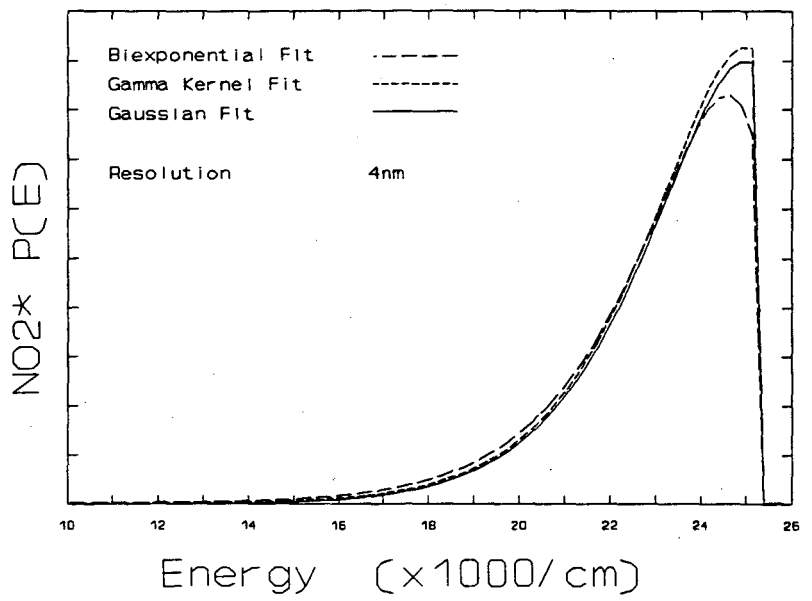

Figure 31 VANPEE NO_2^* $P(E_{int})$ distributions: resolution = 4nm; low energy limit = 10,000 cm^{-1}.

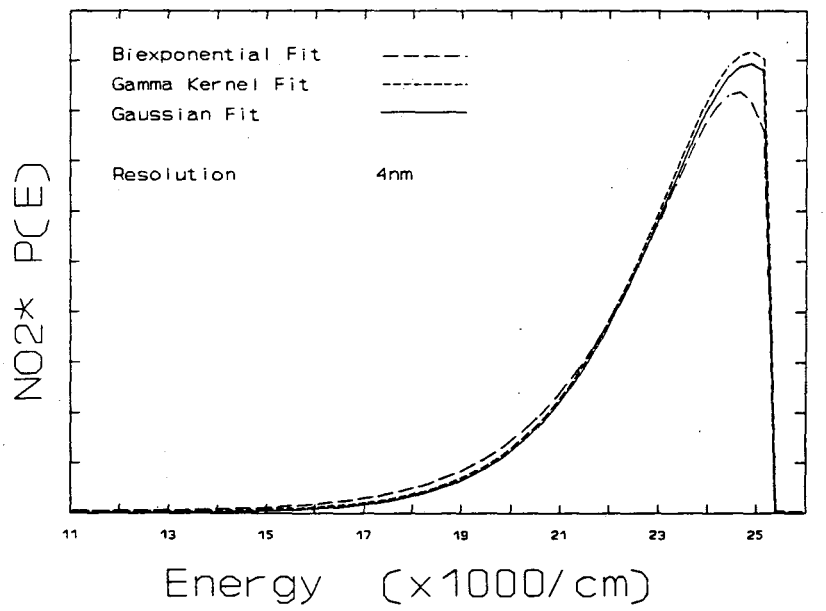

Figure 32 VANPEE NO_2^* $P(E_{int})$ distributions: resolution = 4nm; low energy limit = 11,000 cm^{-1}.

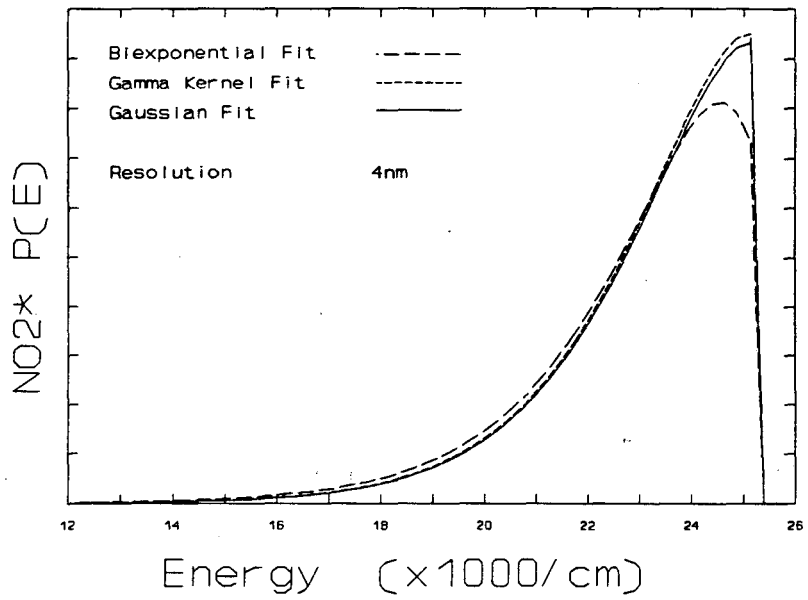

Figure 33 VANPEE NO_2^* $P(E_{int})$ distributions: resolution = 4nm; low energy limit = 12,000 cm^{-1}.

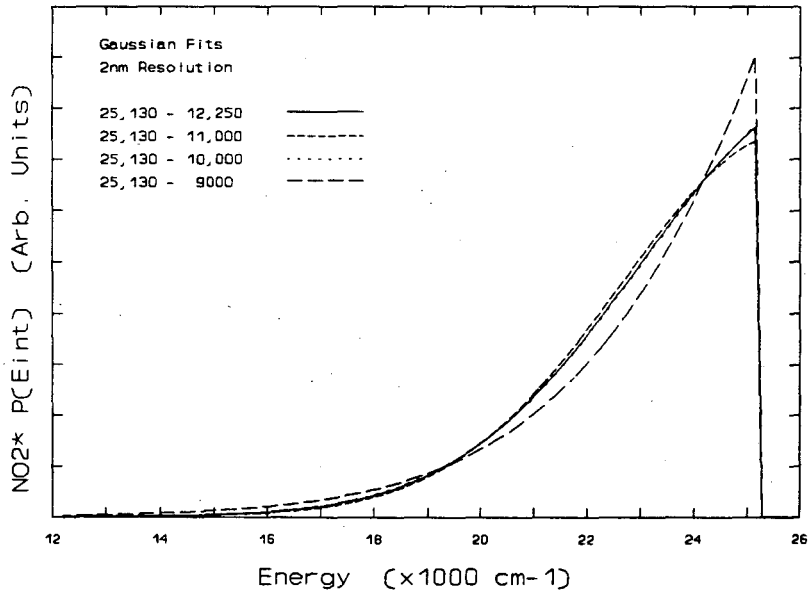

Figure 34 A comparison of all of the Gaussian weighting function fits to the VANPEE data subsets with 2nm resolution.

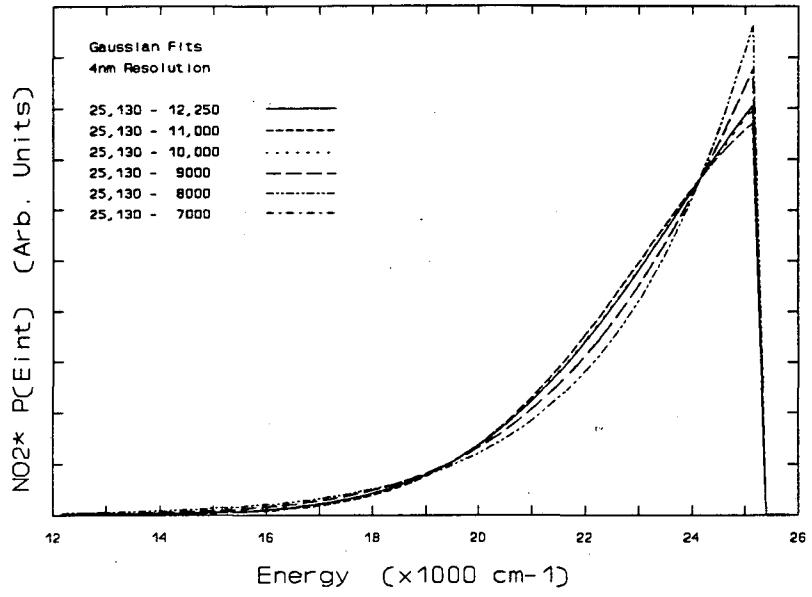

Figure 35 A comparison of all of the Gaussian weighting function fits to the VANPEE data subsets with 4nm resolution.

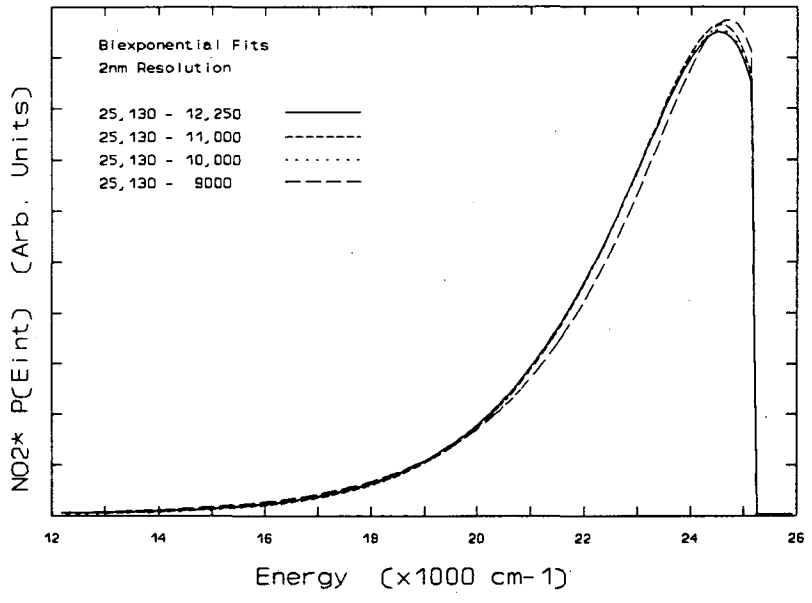

Figure 36 A comparison of all of the biexponential weighting function fits to the VANPEE data subsets with 2nm resolution.

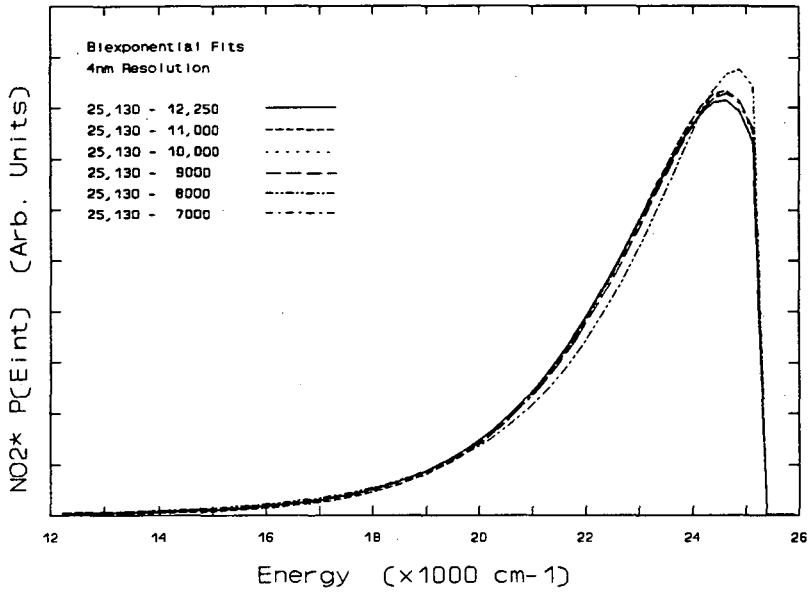

Figure 37 A comparison of all of the biexponential weighting function fits to the VANPEE data subsets with 4nm resolution.

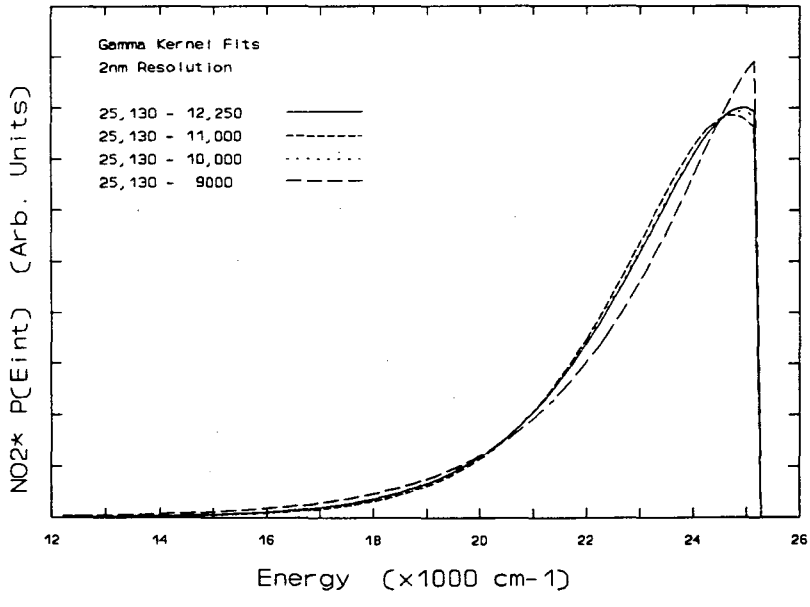

Figure 38 A comparison of all of the gamma kernel weighting function fits to the VANPEE data subsets with 2nm resolution.

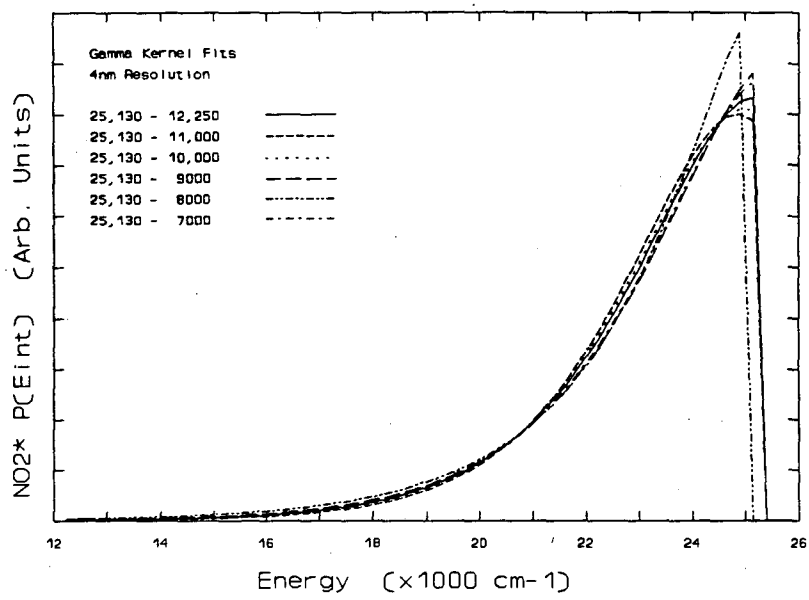

Figure 39 A comparison of all of the gamma kernel weighting function fits to the VANPEE data subsets with 4nm resolution.

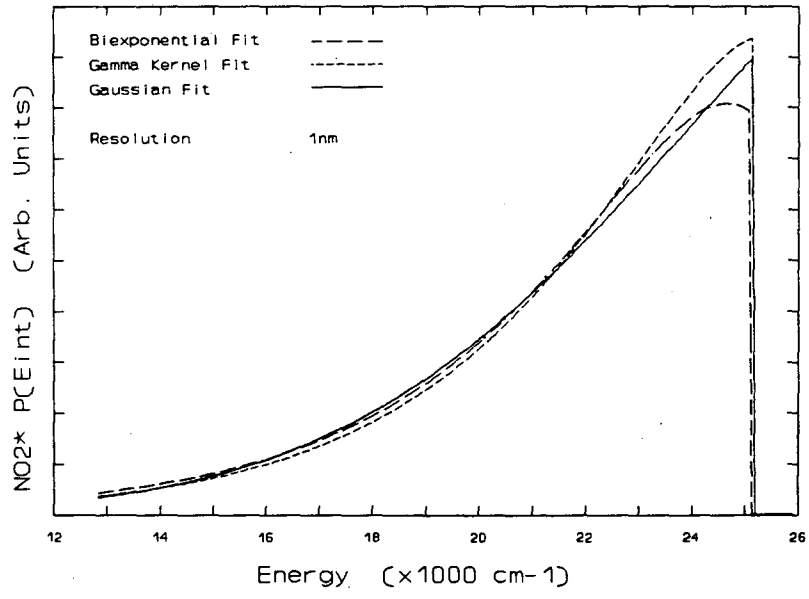

Figure 40 PAULSEN NO_2^* $P(E_{int})$ distributions: resolution = 1nm; low energy limit = 12,740 cm^{-1}.

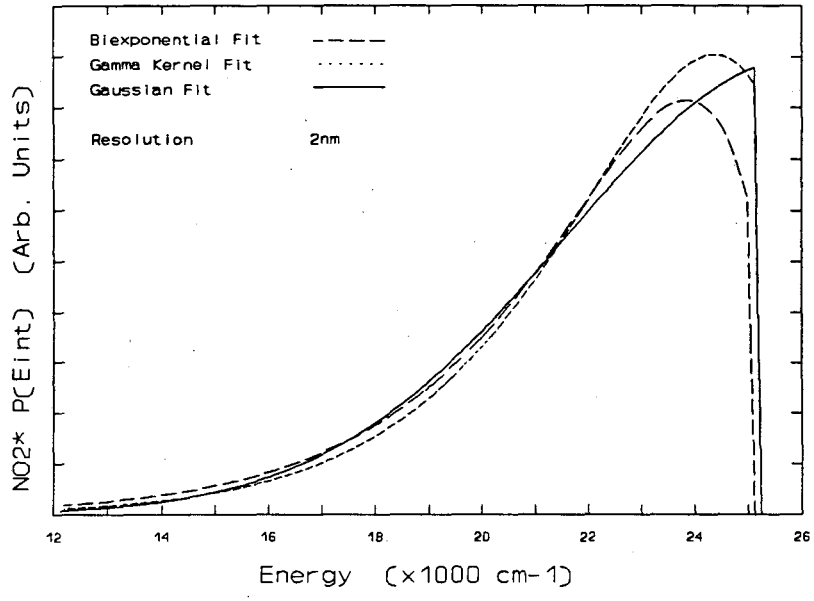

Figure 41 PAULSEN NO_2^* $P(E_{int})$ distributions: resolution = 2nm; low energy limit = 12,250 cm^{-1}.

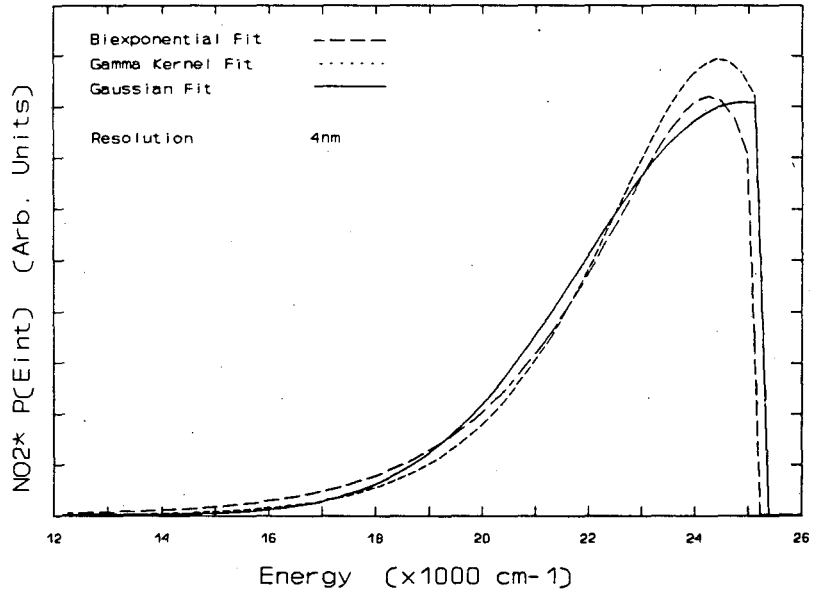

Figure 42 PAULSEN NO_2^* $P(E_{int})$ distributions: resolution = 4nm; low energy limit = 12,250 cm^{-1}.

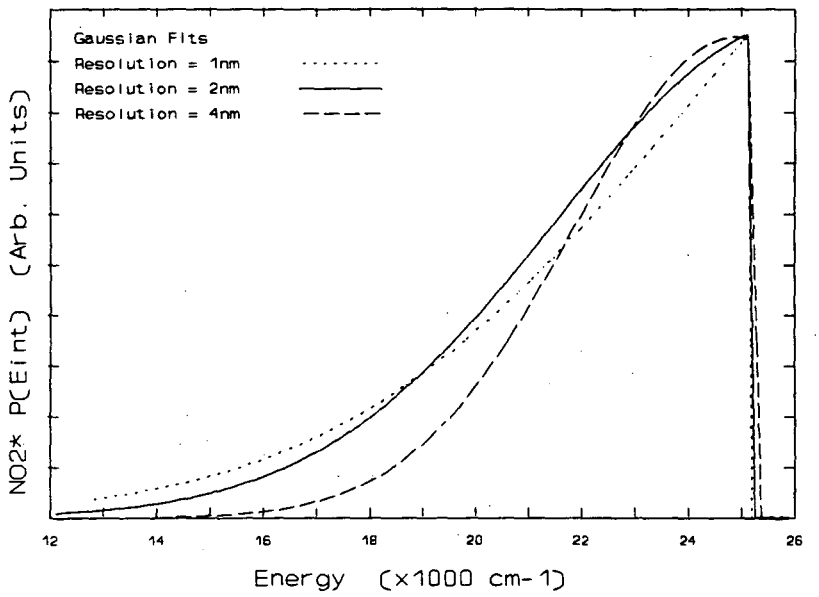

Figure 43 A comparison of all of the Gaussian weighting function fits to the PAULSEN data subsets with 1, 2, and 4nm resolution.

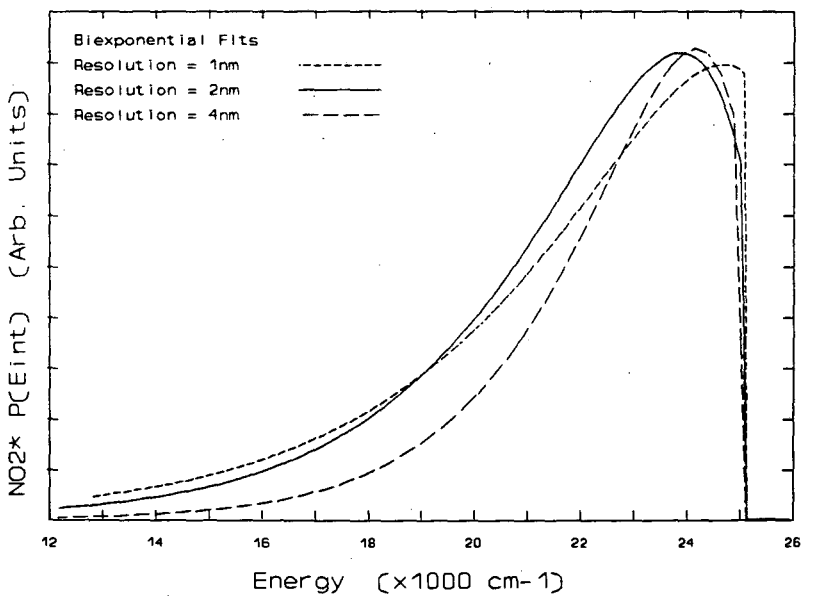

Figure 44 A comparison of all of the biexponential weighting function fits to the PAULSEN data subsets with 1, 2, and 4nm resolution.

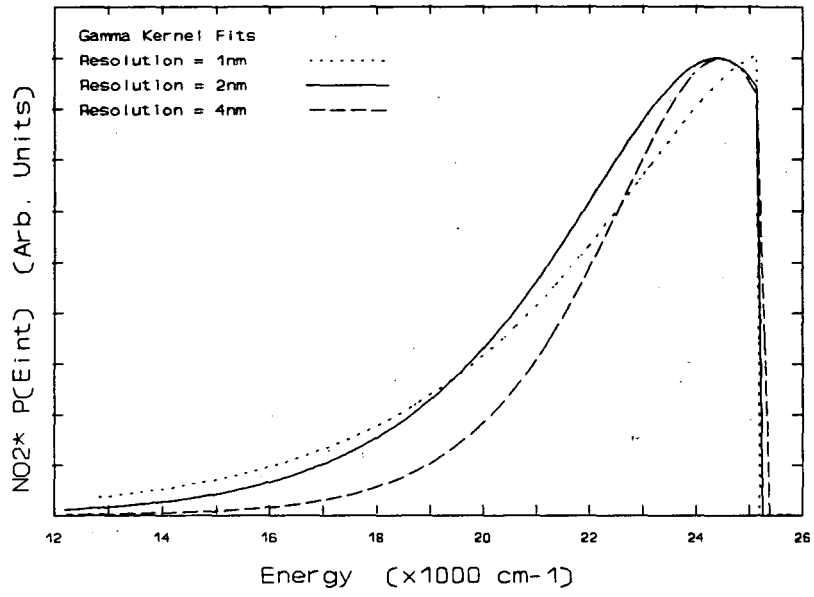

Figure 45 A comparison of all of the gamma kernel weighting function fits to the PAULSEN data subsets with 1, 2, and 4nm resolution.

CHAPTER 2:

ELECTRONICALLY EXCITED NO_2 FROM NITROMETHANE PHOTODISSOCIATION

2.0 ABSTRACT

The photolysis induced fluorescence (PIF) method is used to derive nascent internal energy distributions of rovibronically excited NO_2 fragments (NO_2^* $P(E_{int})$) from nitromethane photodissociation. Experiments conducted at 193.3, 210, 224, and 235nm demonstrates the NO_2^* $P(E_{int})$ contour dependence on the photolysis wavelength. The $P(E_{int})$ transform from inverted distributions sharply peaked at 25,130 cm^{-1} to ones in which a majority of the NO_2^* components have internal energies less than 15,000 cm^{-1} as the single photon excitation energy decreases from 51,000 cm^{-1} to 42,500 cm^{-1}. Despite the change in the $P(E_{int})$ contours, ~65% of the available energy is partitioned into the rovibronic excitation of the NO_2^* fragment at all of the photolysis wavelengths employed. These findings suggest that the dissociations all originate on the $^1B_2$ surface, which results from a ($\pi \rightarrow \pi^*$) electron promotion localized on the NO_2 chromophore, but dissociate via different pathways. The nitromethane results are compared with PIF results also obtained for nitroethane and 1-nitropropane and time of flight measurements obtained for the 193.3nm CH_3NO_2 photolysis.

2.1 INTRODUCTION

The nitroalkanes form a class of energetic materials whose highly exothermic decompositions can serve as the source for fuels, propellants, or explosives. The photochemistry of these molecules has also been implicated in the production of smog and atmospheric alkyl radical generation. Nitromethane, the prototypical molecule of this series, has been the subject of numerous experimental[1,2,3,4,5,6,7,8,9,10,11] and theoretical[12,13,14] photodissociation studies.

The nitromethane absorption spectrum, shown in Figure 1, is a broad continuum extending to a long wavelength limit of 370nm with maxima at 275nm (σ = 3.37x10^{-20} cm^2 $molecule^{-1}$) and 197nm (σ = 1.86x10^{-17} cm^2 $molecule^{-1}$) [10]. Flicker et al. [ref] assign the 275nm feature to a combination of the electric dipole-forbidden 1 $^1A_1 \rightarrow$ 1 $^1A_2$ ($n \rightarrow \pi^*$) and the electric dipole-allowed 1 $^1A_1 \rightarrow$ 1 $^1B_1$ ($\sigma \rightarrow \pi^*$) transitions and the 197nm feature to the 1 $^1A_1 \rightarrow$ 1 $^1B_2$ ($\pi \rightarrow \pi^*$) based on the intensities and angular dependencies of electron scattering experiments. The electronic promotions are highly localized on the NO_2 chromophore, so the transitions are typically discussed in terms of their local C_{2v} symmetries. The extreme localization of the excitation energy in the NO_2 group is further supported by the recent resonance Raman scattering experiments of Lao et al.[11] who observed *only* NO_2 symmetric stretching peaks after 218nm excitation and a combination of NO_2 symmetric stretching and CN stretching after 200nm excitation; no other modes were active. The *ab initio* potential surfaces calculated by Mijoule et al.[13],

and illustrated in Figure 2, verify these assignments. Note the close proximity of the $^1A_2$ and $^1B_1$ surfaces as anticipated by Flicker and that all three excited surfaces correlate to electronically excited NO_2 products. The thermodynamic thresholds for each of the CH_3 + NO_2 product channels is shown in Figure 3.

Several groups have previously reported NO_2 photolysis induced fluorescence (PIF) signals following nitormethane photodissociation in the UV[1,6-9], but none of these reports determined the energy content of the NO_2 fragment. Butler et al.[1] observed dispersed NO_2^* PIF spectra from 193.3nm nitromethane photodissociation (as well as nitroethane and 2-nitropropane) beginning at the 398nm $D_0(NO_2)$ threshold and continuing into the near infrared. Renlund and Trott[8] observed a similar spectrum (as well as nitrobenzene and n-propyl nitrate PIF spectra). Both of these groups also reported intense CH emission at ~425nm from multiphoton processes when higher laser fluences, e.g. 100mJ/pulse, were employed. Schoen et al.[7] and Mialocq and Stevenson[9] have observed a weak PIF signal from 266nm CH_3NO_2 photolysis. These measurements indicate that there is a 70% quantum yield of $NO_2(^2A_1)$ at this wavelength and only 0.1-0.2% NO_2^* production. Additionally, Schoen et al.[9] determined that the yield of $NO_2(^2A_1)$ remained nearly constant for photodissociations at 237, 266, and 296nm, but that the yield of NO_2^* at 237nm had increased by at least an order of magnitude compared to 266nm, and that the NO_2^* yield at 296nm was essentially zero.

Photodissociation studies involving the larger nitroalkanes have been primarily

concerned with identifying the major product channels and the role of HONO elimination in these processes. As an example, Radhakrishnan et al.[15] photolyzed 2-nitropropane at 222, 248.5, and 308nm and observed the production of NO, OH, and HONO. They attribute these products to HONO elimination from 2-nitropropane via a five-membered cyclic transition state. The highly excited HONO product undergoes subsequent dissociation to produce OH and NO. This reactive channel predominates in infrared multiphoton dissociations[3,4] which proceed on S_0 with excitation energies only slightly above the barrier to dissociation.

In this report we present experiments which measure the populations of the fluorescing NO_2 ensemble produced in the photodissociation of nitromethane, nitroethane, and nitropropane. These populations are derived from the dispersed NO_2^* PIF spectra using the integrated fluorescence (IF) method introduced in Chapter 1. By varying the CH_3NO_2 photolysis wavelength between 193.3 and 235nm, we are able to follow the transformation of the of the NO_2^* $P(E_{int})$ as a coarse function of θ, where $\theta = h\nu - D_0(R\text{-}NO_2)$. We also compare the NO_2^* $P(E_{int})$ distributions obtained for photodissocaitons at the same wavelength using different R groups.

2.2 EXPERIMENTAL

The experiments described here represent some of our earliest efforts to record dispersed NO_2 fluorescence spectra following $R\text{-}NO_2$ photodissociation, yet the

experimental apparatus, the collection optics, and the detection electronics are the same as those described in detail in Chapter 3. The major difference between the experiments discussed here and those presented in Chapter 3 is in the laser source. At the time these experiments were conducted, we did not have a tunable UV laser system. Therefore, we were required to use Raman shifting techniques to provide multiple excitation wavelengths to augment the 193.3 and 248.5nm lines available from our excimer laser.

The photodissociation wavelengths used in these experiments were produced by an excimer laser (Questek 2220) operating on the 248.5nm KrF or 193.3nm ArF outputs. By Raman shifting the excimer fundamentals in H_2, we were able to generate 210nm (first Stokes shift of ArF) and 224nm (first anti_Stokes shift of KrF) radiation. This was accomplished by focussing the Excimer beam into a 67cm long stainless steel high pressure cell containing ~ 10 atmospheres of H_2 using a 50cm focal length suprasil lens. The output of the Raman shifting cell was recollimated with another 50cm focal length suprasil lens and sent into a Pellin-Broca prism. The different refractive indices of the Raman shifted wavelengths caused them to spatially separate as the laser beam passed through the prism, resulting in a horizontally dispersed pattern of identifiable laser spots. The diverging Raman wavelengths were softly focussed through the photolysis cell using a 200cm focal length suprasil lens. One could easily distinguish the colors of the visible wavelengths and these were used to help identify the remainder of the wavelengths. The desired Stokes or anti-Stokes wavelength was selected by physically blocking all other beams prior to the photolysis cell.

We produced seven Stokes and two anti-Stokes orders for KrF and eight Stokes orders for ArF using this apparatus. Power conversion efficiencies were about 2% for 210nm production (first Stokes shift from ArF) and 10% at 224nm (first anti-Stokes shift from KrF). We verified the wavelengths of all discernable Raman shifted wavelengths by passing each separated beam into the photolysis cell and monitoring the scattered light spectrum with our optical detection system. We found that the nth order Stokes line was produced by n successive inelastic scattering events incorporating the H_2 $v = 0 \rightarrow 1$ transition rather than a single inelastic photon scattering from the $v = 0 \rightarrow n$ transition. The experimental and calculated line positions agreed to within the bandwidth of the original excimer laser pulse (FWHM = 195 cm^{-1} for KrF and 235 cm^{-1} for ArF). The 235nm nitromethane experiment was conducted using the laser source described in Chapter 3.

Nitromethane (Baker spectral grade and Kodak spectral grade), nitroethane (Kodak), and 1-nitropropane (Baker) were used without further purification. The samples were degassed using repeated freeze-pump-thaw cycles prior to use. The degassed samples were stored under vacuum until required.

2.3 RESULTS

We found that the large absorption cross sections associated with the 193.3, 210, and 224nm experiments led to emissions from multiphoton processes for concentrated

laser fluences, as found previously[1,8]. We were able to eliminate these spurious signals in the 193.3nm experiments by reducing the excimer laser power to ~ 1-5 mJ/pulse and passing the unfocussed beam through the photolysis cell. Clean separation of the Raman shifted laser lines required us to at least partially focus the beam as it passed through the photolysis cell. This caused increased contamination from the multiphoton induced emissions, especially in the crucial 400 to 500nm region. We were able to eliminate these signals, but at the cost of a severely reduced signal-to-noise ratio near the short wavelength fluorescence threshold. This forced us to use higher sample pressures, longer collection gates, and a larger number of averaged shots to obtain the data in these experiments. We also attempted the PIF experiments at 248.5nm for all three nitroalkanes. However, the total PIF signals in each case were prohibitively small (1-3 quanta μs^{-1}) so that we failed to obtained useful spectra.

The PIF spectra presented below have been obtained under nearly collision-free conditions by using sample pressures of 100 millitorr or less and observing the fluorescence signal at times no longer than 100ns after the photodissociation laser pulse. There will be no more than 0.02 hard sphere collisions under these conditions assuming a very conservative hard sphere collision rate of 2 $Torr^{-1}$ μs^{-1} and a 300 K thermal rms velocity for the NO_2 fragments.

For the 224nm and 235nm experiments the energy available to the photofragments is less than $D_0(NO_2)$ and the fluorescence threshold is within our viewing region. We

have edited the data from these experiments so that the fluorescence intensities for all points having energies above $\theta = h\nu - D_0(R\text{-}NO_2)$ are identically equal to zero (the θ sets), or so that all points having energies above $\theta + 1500\ cm^{-1}$ are set to zero (the $\theta+$ sets). We edited the data in an effort to reduce distortions in the IF optimization algorithm due to non-zero fluorescence intensity components in the energetically inaccessible region. Otherwise, these data were fit in the same manner as the full, unedited data.

2.3.A. CH_3NO_2

The 193.3nm CH_3NO_2 PIF spectrum is shown in Figure 4. It has a fluorescence threshold coincident with the 25,130 cm^{-1} $D_0(NO_2)$ energy and quickly gains intensity for energies below 24,000 cm^{-1}. The PIF intensity peaks near 16,000 cm^{-1} and decreases slightly with further decreases in energy, producing a Gaussian-like emission contour. Table I shows that the average $NO_2^{\bullet}$ energy is $\sim$19,500 cm^{-1} and the $P(E_{int})$ peak at 25,130 cm^{-1}. Figure 5 clearly displays this population maximum and illustrates that the weighting of the $NO_2^{\bullet}$ population components has decreased to 20% of its maximum value for $NO_2^{\bullet}$ components having $E_{int} = 12{,}000\ cm^{-1}$. There is good agreement between the weighting functions on the general contour of the $P(E_{int})$, although the sum errors in Table I indicate that the gamma kernel $P(E_{int})$ is slightly preferred over the Gaussian $P(E_{int})$. The biexponential fitting residual is significantly worse for these data. The large fraction of θ retained by the $NO_2^{\bullet}$ fragment indicates that there is only a very small

excitation of the CH_3 internal degrees of freedom and center of mass translational energy release.

The 210nm CH_3NO_2 PIF spectrum is given in Figure 6. θ for this dissociation is 26,500 cm^{-1}. One immediately notes the contrast between this spectrum and the 193.3nm PIF spectrum in Figure 4. The 210nm PIF intensity rises very slowly from its high energy threshold, and does not show significant increase until nearly 20,000 cm^{-1}. We attribute this to an underestimation of the signal intensity due to the decreased 400 - 500nm sensitivity previously mentioned. However, this spectrum also differs from the 193.3nm spectrum at lower energies: the 210nm PIF intensity displays no maximum inside our observation window, although there are indications that its curvature is changing near 14,000 cm^{-1}. The NO_2^* $P(E_{int})$ distribution shown in Figure 7 and numerically evaluated in Table II is correspondingly different from the 193.3nm $P(E_{int})$. The average, rms, and most probable energies for this distribution are all closely spaced near 16,000 cm^{-1}, even though θ is 10,000 cm^{-1} larger. It appears that the NO_2^* ensemble produced in this dissociation has far fewer components with the maximum possible rovibronic energy and an increased contribution from less internally excited components. The fitting residuals for these data are comparable to those for the 193.3nm data.

The 224nm CH_3NO_2 PIF spectrum shown in Figure 8 does not appear drastically different from the 210nm PIF spectrum in Figure 6, although the PIF intensity in the region of 16,000 cm^{-1} seems larger and there is a distinct change in the contour's

curvature with decreasing observation energy. The 23,635 cm^{-1} θ value places the fluorescence threshold within our observation window, although Figure 8 shows that the PIF intensity remains small until 22,000 cm^{-1}. The NO_2^* $P(E_{int})$ in Figure 9 and the numerical information in Table III show that this $P(E_{int})$ is very similar to the 210nm $P(E_{int})$. The population again has average, rms, and most probable energies near 16,000 cm^{-1}. Table III shows that the sum error residuals for the θ subset fits are very low, especially for the biexponential and gamma kernel weighting functions. These $P(E_{int})$ show a nearly uniform distribution of population components for energies below 21,000 cm^{-1}, and rapidly decreasing contributions from NO_2^* components with energies between 21,000 and 23,625 cm^{-1}.

The 21,535 cm^{-1} fluorescence threshold in the 235nm CH_3NO_2 PIF spectrum, Figure 10, clearly demonstrates that there are NO_2^* components having energies up to and including the maximum possible value. This spectrum also clearly represents the least energetic NO_2^* ensemble. There is minimal PIF intensity observed at energies above 17,000 cm^{-1} and no indication of a maximum or curvature change in the PIF contour at energies above 12,000 cm^{-1}. The NO_2^* $P(E_{int})$ in Figure 11 have also transformed into another shape. Whereas the 193.3nm $P(E_{int})$ was inverted and the 210 and 224nm $P(E_{int})$ had maxima inside our observation window, the 235nm CH_3NO_2 $P(E_{int})$ shows only small contributions from NO_2^* components having energies near θ and a significantly increased proportion of the ensemble having rovibronic energies concentrated at the low end of our observation range. The average energy of the $P(E_{int})$ distribution has not decreased

markedly from the averages for the 210 or 224nm $P(E_{int})$, but the 235nm average NO_2^* energy is most likely artificially inflated by our limited observation region. Table IV shows that the optimized $P(E_{int})$ for these data produce another series of very low sum errors.

2.3.B. Nitroethane and 1-Nitropropane

The 193.3nm nitroethane PIF spectrum shown in Figure 12 is reminiscent of the 193.3nm CH_3NO_2 PIF spectrum in Figure 4. The PIF intensity increases immediately from its 25,130 cm^{-1} threshold and reaches a maximum near 15,000 cm^{-1}. The overall emission contour is again Gaussian-like and there is no noticeable vibronic structure. Table V and Figure 13 show that the nitroethane NO_2^* $P(E_{int})$ is also inverted, with a sharp maximum at $D_0(NO_2)$ and an average energy of ~ 19,000 cm^{-1}. The population is concentrated towards higher energies, although it is broad and the NO_2^* components having energies of 12,000 cm^{-1} are weighted 20% of the population maximum. The sum error values show that the biexponential and gamma kernel functions provide better $P(E_{int})$ than the Gaussian weighting function.

The 224nm nitroethane PIF spectrum, Figure 14, and the NO_2^* $P(E_{int})$ derived from these data, Figure 15 and Table VI, are also very similar to their CH_3NO_2 counterparts (see Figures 8 and 9 and Table III). The nitroethane NO_2^* $P(E_{int})$ also display the same contour metamorphosis as the photolysis wavelength decreases from

193.3nm to 224nm. We note that the average energy of the 224nm nitroethane $P(E_{int})$ is about 800 cm^{-1} larger than the average energy of the 224nm CH_3NO_2 $P(E_{int})$, but this may not be significant since the sum errors for the nitroethane experiments are more than twice as large as the corresponding CH_3NO_2 residuals.

The results of the 193.3nm 1-nitropropane PIF experiment are shown in Figure 16 and the NO_2^* $P(E_{int})$ derived from these data are given in Table VII and Figure 17. The emission spectrum again has the Gaussian-like shape, but the nitropropane PIF intensity just reaches its maximum intensity at 12,000 cm^{-1}. This spectral distribution infers a less energetic NO_2^* ensemble than those produced in the 193.3nm photodissociations of CH_3NO_2 or nitroethane. The numerical values support such an assertion. The average energy of the NO_2^* $P(E_{int})$ derived from the 193.3nm nitropropane photolysis is $\sim$18,000 cm^{-1}, nearly 1000 cm^{-1} lower than the CH_3NO_2 and nitroethane average NO_2^* energies. The $P(E_{int})$ in Figure 17 is also much broader and, while it still ha a maximum at 25,130 cm^{-1}, the $P(E_{int})$ for NO_2^* components at 12,0000 cm^{-1} has only decreased to 35% of the maximum. Note as well that the sum errors for the nitropropane fits are substantially larger than those for the CH_3NO_2 or nitroethane $P(E_{int})$.

DISCUSSION

2.4.A. CH_3NO_2 Dissociation Mechanism

The NO_2^* $P(E_{int})$ derived from the CH_3NO_2 PIF spectra exhibit a very interesting dependence on the photodissociation wavelength. For the 235nm photodissociation the energy available to the fragments, $\theta = h\nu - D_0(CH_3\text{-}NO_2)$, is 21,535 cm^{-1}, yet the $P(E_{int})$ is dominated by NO_2^* components with rovibronic energies less than 18,000 cm^{-1}; very few NO_2^* components have energies approaching θ (Figure 11). The 224 and 210nm CH_3NO_2 photodissociations produces θ values in the 24,000 - 26,000 cm^{-1} range and $P(E_{int})$ which are still dominated by NO_2^* components having energies below θ, but the population distribution is more energetic and nearly uniform (Figures 9 and 7). These $P(E_{int})$ also show an increasing fraction of the NO_2^* components have rovibronic energies at or near θ. The 30,715 cm^{-1} θ associated with the 193.3nm photolysis is far above the energy required for secondary dissociation of the NO_2 fragment and the $P(E_{int})$ from these experiments is now inverted, peaking at 25,130 cm^{-1}. NO_2^* components with energies above 20,000 cm^{-1} dominate this population (Figure 5), in stark contrast to the $P(E_{int})$ derived for longer wavelength photodissociations.

It can be seen from Figure 1 that all of the photolysis wavelengths used in this study access portions of the intense absorption feature attributed to the $^1B_2$ potential surface and a $\pi \rightarrow \pi^*$ electronic promotion localized on the NO_2 chromophore. Mijoule et al.[13] conclude that the transition dipole moment for this transition is polarized in the C-NO_2 plane and oriented almost perpendicularly to the C-N bond. Figure 2 shows that the $^1B_2$ surface is predissociated by a repulsive B_2 surface corresponding to an excitation which is repulsive in the C-N bond. Kaufman et al.[12] have similarly noted the CN(σ^*)

molecular orbital replaces the $NO_2(\pi^*)$ orbital as the HOMO for R_{C-N} values greater than 2 Å. Lao et al.[11] have concluded that this predissociation is responsible for the CN stretching progression they observe in the 200nm CH_3NO_2 resonance Raman spectrum. The 218nm Raman spectrum showed no CN stretching activity presumably because there was insufficient energy to reach the B_2/B_2 intersection portion of the potential surface. However, Mijoule's *ab initio* calculations also conclude that the vertical excitation energy required to reach the $^1B_2$ surface is 53,500 cm^{-1}, the equivalent of a 187nm photon and Figure 2 shows that the $^1B_2$ surface is not significantly less energetic anywhere else in the Franck-Condon region. The $^1B_1$ ($\sigma \rightarrow \pi^*$) and $^1A_2$ ($n \rightarrow \pi^*$) have significantly lower calculated vertical transition energies - 36,940 and 34,000 cm^{-1}, respectively - and are thought responsible for the less intense absorption feature around 275nm. Thus, the absorption spectrum suggests that the 235-193nm CH_3NO_2 photodissociation experiments all occur via the same transition, but the behavior of the NO_2^* $P(E_{int})$ and the energetic information obtained from the Mijoule calculations[13] suggest that multiple potential surfaces are involved in these transitions. The problem remains to rectify this discrepancy.

The 193.3nm NO_2^* $P(E_{int})$ is clearly unique. We suspect that this photodissociation is governed by the repulsive B_2 surface after initial excitation via the $^1B_2$ ($\pi \rightarrow \pi^*$) transition. The concentration of energy in the initially excited NO_2 portion of the CH_3NO_2 parent is consistent with a simple bond rupture mechanism. The strong PIF signals observed from this photolysis wavelength are indicative of a transition which

correlates directly with electronically excited NO_2 products, as the repulsive B_2 surface does.

The curve crossing which characterizes the 193.3nm photodissociation dynamics is energetically inaccessible in the 224 and 235nm experiments. The 218nm Raman spectrum[11], which displays activity only in the NO_2 symmetric stretching mode, verifies this conclusion. The resulting NO_2^* $P(E_{int})$ have greatly reduced average energies and are no longer inverted. If we assume that the ($\pi \rightarrow \pi^*$) excitation to the $^1B_2$ surface is still responsible for the oscillator strength in these excitations, then the NO_2^* populations probably result from the predissociation of the $^1B_2$ surface by one (or both) of the lower energy CH_3NO_2 excited electronic surfaces. We note that electric dipole transitions to the $^1B_1$ surface are allowed in both the local C_{2v} symmetry of the NO_2 chromophore and in nitromethane's molecular C_s symmetry. Further, we note that Mijoule et al.[13] find significant change in the NO_2 bondlengths and bond angle upon promotion into this state, but no change in the C-N bond length which would explain the 218nm Raman spectrum. The $^1B_1$ surface also correlates directly to electronically excited NO_2 products. Dissociations along this surface would also encounter the steeply repulsive B_2 surface, but this crossing would occur at large R_{C-N} distances in the exit channel. The lack of substantial PIF signal at 248.5 nm indicates the initial photoexcitation must exceed 40,000 cm^{-1} in order to access electronically excited NO_2 products directly.

The less energetic NO_2^* $P(E_{int})$ from such a predissociative mechanism reflect the

longer lifetime of the excited CH_3NO_2 molecule. Rather than undergoing immediate dissociation with the majority of the initial excitation energy still concentrated in the NO_2 chromophore, the CH_3NO_2 molecules excited with 224 or 235nm photons survive for several vibrational periods. During this time the excitation energy can more readily randomize itself throughout the molecule. The proposed dissociation mechanism then suggests that the CH_3 fragments created in 224 and 235nm CH_3NO_2 photolysis contain proportionately more rovibrational excitation than CH_3 fragments created in 193nm photodissociation.

The 210nm CH_3NO_2 photodissociation is an intermediate case. The $NO_2^{\bullet}$ $P(E_{int})$ associated with this process are similar to those derived for the 224nm photolysis, but the initial excitation energy is possibly sufficient to access the B_2/B_2 surface intersection. The lack of inversion in the $P(E_{int})$ suggests that if there is any competition between the two proposed dissociation mechanisms in this experiment predissociation through the $^1B_1$ state dominates.

2.4.B. CH_3NO_2 Dissociation Energetics

The θ values of the 193.3 and 210 nm CH_3NO_2 photodissociations (30,715 and 26,600 cm^{-1}) exceed $D_0(NO_2)$ and prevent us from quantitatively evaluating the entire $NO_2^{\bullet}$ $P(E_{int})$ distribution, since NO_2 fragments with $E_{int} > 25,130$ cm^{-1} dissociate rather

than fluoresce. The statistical values obtained from the IF NO_2^* $P(E_{int})$, therefore represent a lower limit for the energetics of the complete NO_2^* $P(E_{int})$. However, the IF $P(E_{int})$ represent the energy distribution of the fluorescing NO_2 ensemble with E_{int} between 25,130 and 12,500 cm^{-1}.

The 193.3nm NO_2^* $P(E_{int})$ distribution is sharply peaked at 25,130 cm^{-1} and decays to 20% of its maximum value at 12,250 cm^{-1}, as seen in Figure 5. Table I shows that the average energy of the NO_2^* ensemble is ~ 19,000 cm^{-1}, or 62% of θ. Extrapolation of the high energy portion of the $P(E_{int})$ indicates that a significant fraction of the NO_2^* fragments are created with internal energies larger than $D_0(NO_2)$, and these NO_2^* components are not detected in the PIF spectrum.

This time of flight translational energy distribution (TOF $P(E_T)$) derived from the 193.3nm CH_3NO_2 photodissociation[1] is given in Figure 18. One immediately observes that the $P(E_T)$ is largely concentrated at low translational energies and that the maximum translational energy release never exceeds 16,000 cm^{-1} although there is 30,715 cm^{-1} available. Blais[2] found that the most probable kinetic energy release from 193.3nm CH_3NO_2 photolysis is 7% (2150 cm^{-1}) and that the average translational energy is 19% (5835 cm^{-1}). This means that the most probable $\{E_{int}(CH_3) + E_{int}(NO_2)\}$ is 28,565 cm^{-1} and the average $\{E_{int}(CH_3) + E_{int}(NO_2)\}$ is 24,880 cm^{-1}. The average energy of our PIF NO_2^* $P(E_{int})$ distributions approaches 76% of this value. This emphasizes the point that even without including the NO_2^* components with the highest possible E_{int}, the IF NO_2^*

$P(E_{int})$ still correctly concludes that the NO_2 fragment retains most of the available energy in this dissociation.

We note from the maximum translational energy release in Figure 18 that the CH_3 and NO_2 fragments retain a minimum of 14,000 cm^{-1} in internal excitation after 193.3nm CH_3NO_2 photodissociation. If we assume that the equilibrium geometry of the CH_3 group in CH_3NO_2 is preserved on the CH_3NO_2 excited PES prior to dissociation, then the metamorphosis of the CH_3 fragment from nearly tetrahedral to trigonal planar configurations has a classical energy of 2500 cm^{-1} associated with it according to the Yamada[16] potential. The lack of CH_3 ν_2 activity in the resonance Raman spectra[11] support the conclusion that this mode is not Franck-Condon active and that the CH_3 geometry on the $^1B_2$ surface is essentially identical to that of the equilibrium configuration. This implies that we should consider an effective θ value for CH_3NO_2 photodissociation which incorporates the required partitioning of 2500 cm^{-1} into CH_3 reorganization where $\theta_{eff} = \theta - 2500\ cm^{-1} = h\nu - D_0(R\text{-}NO_2) - 2500\ cm^{-1}$.

Figure 19 compares the PIF NO_2^* $P(E_{int})$ and TOF $P(E_{int})$ distributions. We obtained the TOF $P(E_{int})$ over the energy region of interest by making the transformation $E_{int} = \theta - E_T$ and using the setting $P(E_T) = P(E_{int} = \theta\text{-}E_T)$. Note that a direct quantitative comparison of the two distributions is incorrect since the TOF measurement contains information about both fragments while the PIF distribution only reflects the NO_2^* $P(E_{int})$. However, a qualitative comparison of the two curves illustrates that the PIF NO_2^* $P(E_{int})$

correctly mirrors the TOF distribution. We continue our efforts to discover the correct manipulations required to enable a direct comparison of PIF and TOF results, but at this date this formulation is unknown.

The 210nm NO_2^* $P(E_{int})$ statistics in Table II show that this photolysis also partitions 16,000 cm^{-1} of the 26,000 cm^{-1} available into the NO_2 fragment. However, as has been mentioned above, these results should be regarded warily because of uncertainties in the 210nm PIF spectrum in the 400 to 500nm region. Despite this problem, we determine that a minimum of 62% of θ (68% of θ_{eff}) is locked into NO_2 internal degrees of freedom.

The 224 and 235nm CH_3NO_2 photodissociations are the first examples of R-NO_2 PIF experiments in which θ is less than $D_0(NO_2)$ and the entire NO_2^* $P(E_{int})$ distribution can be analyzed. The PIF spectra shown in Figures 9 and 11 confirm that these dissociations have NO_2^* components with internal energies up to the maximum possible value, θ. The 224nm data produce optimized NO_2^* $P(E_{int})$, Figure 9, which peak in the middle of our observation window and decrease to lower energies. The 235nm data generate optimized NO_2^* $P(E_{int})$ which are concentrated at much lower energies and probably peak at an energy below our low energy observation limit. The average energy of the 224nm NO_2^* $P(E_{int})$ distribution is 16,330 cm^{-1}, or 69% of the 23,625 cm^{-1} available to the fragments. The fraction of energy partitioned into the NO_2 fragment increases to 77.4% if θ is lowered by 2500 cm^{-1} to account for the classical

reorganization energy required by the CH_3 fragment. Assuming that the average CH_3 internal energy is 2500 cm^{-1}, then the average translational energy produced in this dissociation 4775 cm^{-1}, or 20% of θ. Note that this is in excellent agreement with the translational energy partitioning found by Blais[2] at 193.3nm. The 15,408 cm^{-1} average $NO_2^{\bullet}$ energy found for the 235nm CH_3NO_2 $P(E_{int})$ again reflects a partitioning of 70% of θ into the NO_2 fragment. However, the average energy for this distribution is subject to inaccuracies since the $P(E_{int})$ suggests there are significant contributions from $NO_2^{\bullet}$ components with below our observation window.

2.4.C. Nitroethane and 1-Nitropropane Energetics

As with the nitromethane experiments, the θ values associated with the 193.3nm photodissociations of nitroethane and 1-nitropropane are too large for us to make complete quantitative evaluations on the energy partitioning, but we may again draw qualitative conclusions. The reader is directed to Figures 5, 13, and 17 for the $P(E_{int})$ distributions and Tables I, V, and VII for the appropriate statistics. The $NO_2^{\bullet}$ $P(E_{int})$ derived from the respective PIF spectra also have average $NO_2^{\bullet}$ energies between 18,000 and 20,000 cm^{-1}, peak at $D_0(NO_2)$, and consist mostly of $NO_2^{\bullet}$ components with energies above 18,000 cm^{-1}, as with nitromethane. These $P(E_{int})$ distributions demonstrate that ~ 65% of θ is partitioned into NO_2 internal degrees of freedom after the C-N bond breaks. As above, this value is again a lower limit on the actual partitioning, but is in good agreement with the average energy inferred to be in the NO_2 fragment from TOF

experiments[1,2]. Within the uncertainties of the IF method, we observe no differences in the nitromethane, nitroethane, and 1-nitropropane photodissociations at 193.3nm.

The 224nm nitroethane experiment provides a better chance to compare the NO_2^* $P(E_{int})$ distributions from two different nitroalkanes. The C-N bond energies in CH_3NO_2 and $C_2H_5NO_2$ differ by only 140 cm^{-1}, so the θ values in these experiments are virtually identical. Any differences in the $P(E_{int})$ distributions should, therefore, be caused by the influence of the alkyl radical. Figures 9 and 15 illustrate that the $P(E_{int})$ are quite similar. The most noticeable difference is a slight increase in the concentration of NO_2^* components with energies near θ for the nitroethane 224nm $P(E_{int})$. The statistics in Tables II and VI show this increase more clearly in the average and rms energies of each distribution. This small increase in the nitroethane NO_2^* $P(E_{int})$ probably reflects the reduced reorganizational energy of the C_2H_5 radical compared to CH_3: the free C_2H_5 molecule should retain the tetrahedral geometry it has in $C_2H_5NO_2$ while the free CH_3 molecule necessarily assumes a planar geometry. Additionally, the CH_3 group in CH_3NO_2 is oriented in such a manner that it is mechanically more efficient for its ν_2 umbrella bending motion to absorb the recoil force generated by C-N repulsion than any normal mode of the kinked C_2H_5.

2.5 CONCLUSIONS

We have photodissociated nitromethane at 193.3, 210, 224, and 235nm and

determined the internal energy distributions associated with the production of electronically excited NO_2 fragments by direct measurement. Using the integrated fluorescence method we find that the energy partitioned into NO_2 internal degrees of freedom during the C-N bond cleavage represents ~65-70% of the available energy. Despite the relatively constant fraction of the available energy partitioned into the NO_2^* $P(E_{int})$, we find that the nature of these distributions changes significantly with the photodissociation wavelength. The 193.3nm CH_3NO_2 dissociation appears to be dominated by a steeply repulsive B_2 surface which predissociates the $^1B_2$ ($\pi \rightarrow \pi^*$) surface reached by the initial photoexcitation. The $P(E_{int})$ derived from the 210, 224, and 235nm photodissociations are consistent with a predissociation to lower energy surfaces that also correlate to electronically excited NO_2 products. Experiments determining the 193.3 and 224nm nitroethane and 193.3nm 1-nitropropane NO_2^* $P(E_{int})$ distributions showed no drastic differences when compared to the nitromethane $P(E_{int})$. This leads us to conclude that the potential energy surface(s) associated with the generation of NO_2^* products in nitroalkane photodissociation near 200nm are virtually independent of the identity of the alkyl group and depend principally on the characteristics of the NO_2 group and its electronic states.

REFERENCES

[1] L.J. Butler, D. Krajnovich, and Y.T. Lee, J. Chem. Phys. **79**, 1708 (1983).

[2] N.C. Blais, J. Chem. Phys. **79**, 1723 (1983).

[3] A.M. Wodtke, E.J. Hintsa, and Y.T. Lee, J. Phys. Chem. **90**, 3549 (1986).

[4] B.H. Rockney and E.R. Grant, J. Chem. Phys. **79**, 708 (1983).

[5] W.M. Flicker, O.A. Mosher, and A. Kuppermann, J. Chem. Phys. **72**, 2788 (1980).

[6] K.G. Spears and S.F. Brugge, Chem. Phys. Lett. **54**, 373 (1978).

[7] P.E. Schoen, M.J. Marrone, J.M. Schnur, and L.S. Goldberg, Chem. Phys. Lett. **90**, 272 (1982).

[8] A.M. Renlund and W.M. Trott, Chem. Phys. Lett. **107**, 555 (1984).

[9] J.L. Mialocq and J.C. Stevenson, Chem. Phys. **106**, 281 (1986).

[10] W.D. Taylor, T.D. Allston, M.J. Moscato, G.B. Fazekas, R. Kozlowski, and G.A. Takacs, Int. J. Chem. Kin. **XII**, 231 (1980).

[11] K.Q. Lao, E. Jensen, P.W. Kash, and L.J. Butler, J. Chem. Phys. **93**, 3958 (1990).

[12] J.J. Kaufman, P.C. Hariharan, C. Chabalowski, and M. Hotokka, Int. J. Quantum Chem: Quantum Chem. Symp. 19, 221 (1986).

[13] C. Mijoule, S. Odiot, S. Fliszar, and J.M. Schnur, J. Mol. Struct./Theochem **149**, 311 (1987).

[14] P. Pernot, O. Atobek, J.A. Beswick, and B. Levy, Int. J. Quantum Chem. **XXXIIV**, 161 (1988); P. Pernot, O. Atobek, J.A. Beswick, and Ph. Millie, J. Phys. Chem. **91**, 1397 (1987).

[15] G. Radhakrishnan, T. Parr, and C. Wittig, Chem. Phys. Lett. **111**, 25 (1984).

[16] C. Yamada, E. Hirota, K. Kawaguchi, J. Chem. Phys. **75**, 5256 (1981).

Table I. 193.3nm CH_3NO_2 photolysis: θ = 30,715 cm^{-1}. Optimized weighting function parameters from IF analysis. See also Figure 5.

Set	M	A	B	Sum Error ($x10^{-3}$)	E_{ave}	E_{rms}	E_{max}
Gaussian Weighting Function							
Full	30,715	26,520	6343.7	1.8841	19,243	19,568	25,125
Biexponential Weighting Function							
Full	30,715	197,000	3906.2	2.4309	18,952	19,319	25,125
Gamma Kernel Weighting Function							
Full	30,715	6404.3	2.8200	1.7296	19,497	19,817	24,390

*The "Set" label identifies edited and unedited data, as described in the text.
*The definitions of the Gaussian, biexponential, and gamma kernel weighting functions are given in Chapter 1, Equations (1) - (3).
*The sum error is a measure of the calculated - experimental fitting residual. This is the figure of merit to use when comparing different optimized weighting function results.
*The average, rms, and most probable energies of the NO_2^* $P(E_{int})$ distribution are given in these columns in the units of cm^{-1}.

Table II. 210nm CH_3NO_2 photolysis: θ = 26,000 cm^{-1}. Optimized weighting function parameters from IF analysis. See also Figure 7.

Set	M	A	B	Sum Error ($x10^{-3}$)	E_{ave}	E_{rms}	E_{max}
Gaussian Weighting Function							
Full							
Biexponential Weighting Function							
Full							
Gamma Kernel Weighting Function							
Full	26,000	9671.9	3.1625	2.0483	16,015	16,261	15,797

Table III. 224nm CH_3NO_2 photolysis: θ = 23,625 cm^{-1}. Optimized weighting function parameters from IF analysis. See also Figure 9.

Set	M	A	B	Sum Error ($x10^{-3}$)	E_{ave}	E_{rms}	E_{max}
Gaussian Weighting Function							
Θ	23,625	16,954	4750	1.1387	16,163	16,402	15,923
Θ+	23,625	16,922	4875	1.0905	16,153	16,395	15,822
Biexponential Weighting Function							
Θ	23,800	4871.2	11,350	0.7168	16,071	16,315	15,060
Gamma Kernel Weighting Function							
Full	23,800	6150	0.78125	1.4300	16,257	16,527	16,260
Θ	23,625	5715.3	0.80312	0.7277	16,331	16,591	16,891
Θ+	24,500	6862.8	1.4437	0.8430	16,377	16,640	17,006

Table IV. 235nm CH_3NO_2 photolysis: θ = 21,535 cm^{-1}. Optimized weighting function parameters from IF analysis. See also Figure 11.

Set	M	A	B	Sum Error ($x10^{-3}$)	E_{ave}	E_{rms}	E_{max}
Gaussian Weighting Function							
Θ	22,000	14,464	4421.9	1.1905	15,201	15,371	13,440
Biexponential Weighting Function							
Θ	22,406	41,500	12,700	1.2805	15,141	15,314	12,195
Gamma Kernel Weighting Function							
Θ	24,000	9838.5	2.5775	1.1451	15,408	15,596	13,337

Table V. 193nm Nitroethane photolysis: θ = 30,575 cm^{-1}. Optimized weighting function parameters from IF analysis. See also Figure 13.

Set	M	A	B	Sum Error ($x10^{-3}$)	E_{ave}	E_{rms}	E_{max}
Gaussian Weighting Function							
Full	25,130	99,750	24,000	1.6161	18,537	18,926	25,125
Biexponential Weighting Function							
Full	30,575	500	6743.2	1.3657	18,647	19,038	25,125
Gamma Kernel Weighting Function							
Full	30,575	41.968	6.25E-3	1.3705	18,849	19,233	25,125

Table VI. 224nm nitroethane photolysis: θ = 23,485 cm^{-1}. Optimized weighting function parameters from IF analysis. See also Figure 15.

Set	M	A	B	Sum Error ($x10^{-3}$)	E_{ave}	E_{rms}	E_{max}
Gaussian Weighting Function							
Θ	23,485	17,562	4328.1	2.3062	16,396	16,631	16,772
Θ+	23,485	17,547	4578.1	2.1289	16,369	16,610	16,611
Biexponential Weighting Function							
Θ	22,760	636.3	20,800	1.3082	16,212	16,458	19,455
Gamma Kernel Weighting Function							
Θ	23,485	4694.8	0.90625	1.5705	16,571	16,829	18,450
Θ+	23,485	4687.5	0.78750	1.6887	16,540	16,802	18,315

Table VII. 193nm Nitropropane photolysis: θ = 31,130. Optimized weighting function parameters from IF analysis. See also Figure 17.

Set	M	A	B	Sum Error ($\times 10^{-3}$)	E_{ave}	E_{rms}	E_{max}
Gaussian Weighting Function							
Full	25,130	2.882E6	176,000	2.5165	*	*	*
Biexponential Weighting Function							
Full	31,130	500	10,820	2.5142	17,833	18,229	25,125
Gamma Kernel Weighting Function							
Full	31,130	26.830	3.125E-3	2.7061	18,378	18,771	25,125

* These fitting parameters caused numerical overflow errors in the population calculation algorithm.

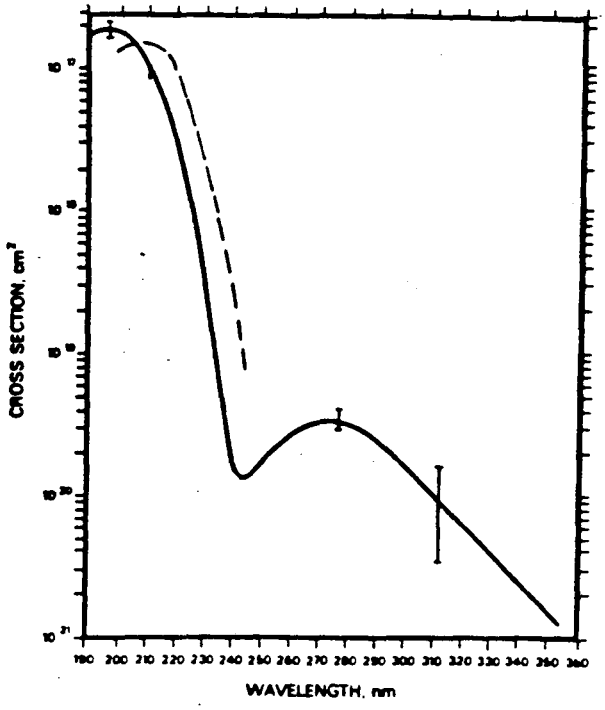

Figure 1. CH_3NO_2 absorption cross sections [Ref. 10].

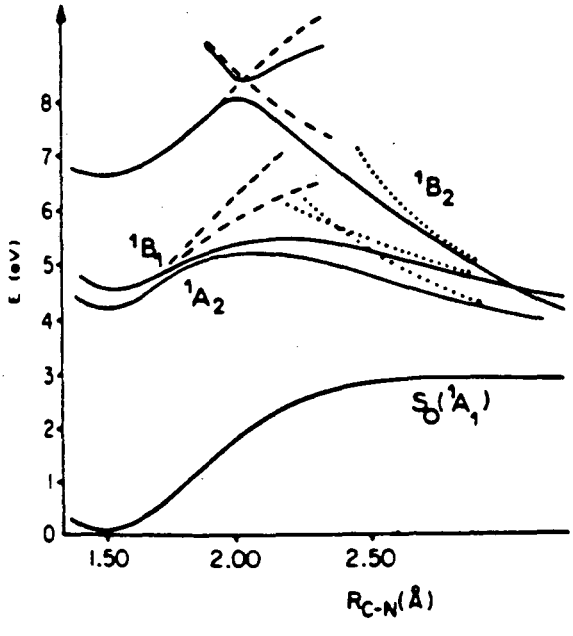

Figure 2. CH_3NO_2 potential energy surfaces for energies from 0 to 8 eV as calculated by Mijoule et al. [Ref 13].

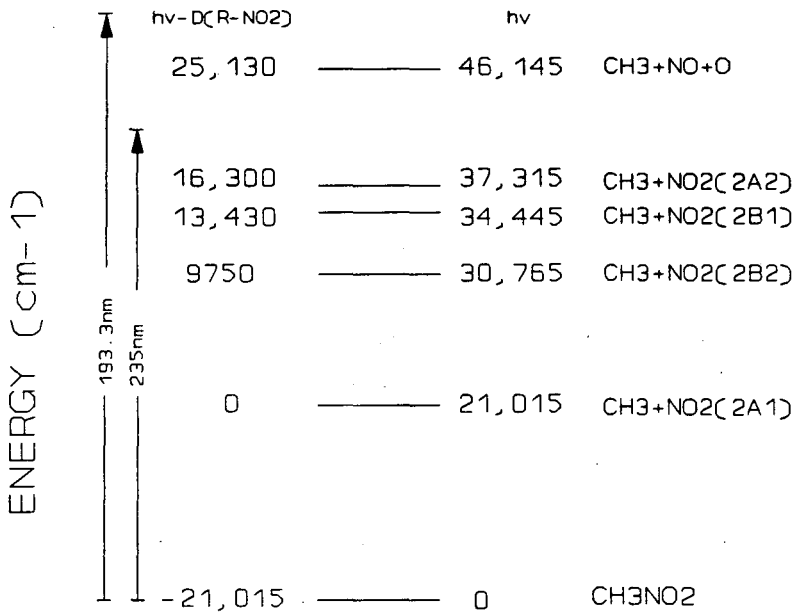

Figure 3. Thermodynamic thresholds for the production of CH_3 and NO_2 products in nitromethane photodissociation.

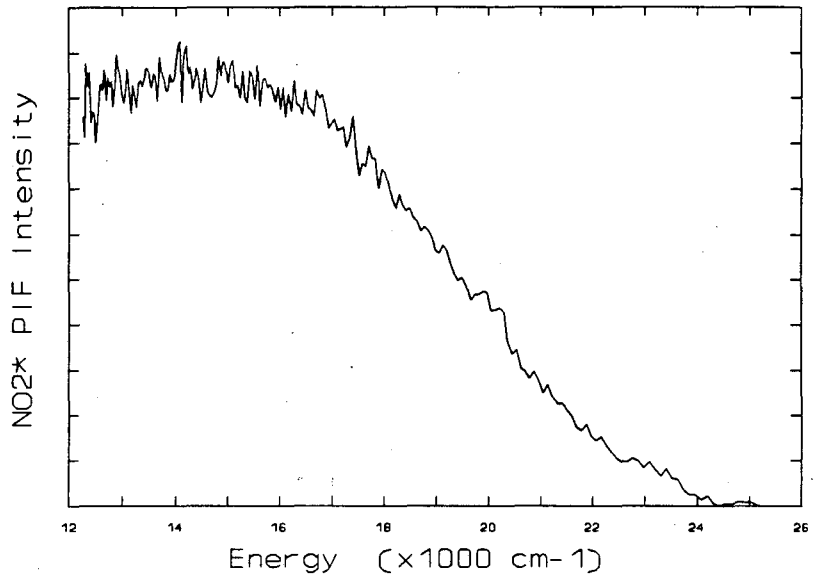

Figure 4. 193.3nm CH_3NO_2 PIF spectrum.

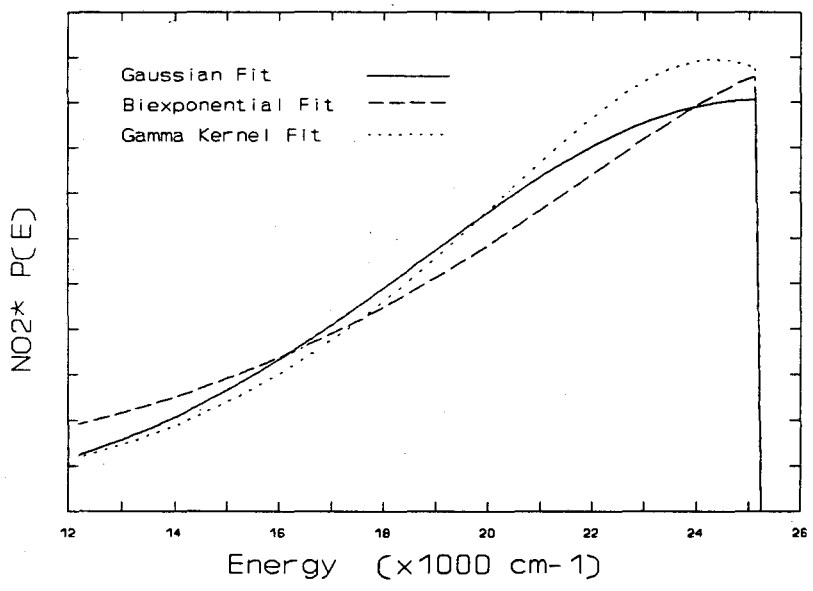

Figure 5. 193.3nm CH_3NO_2 NO_2^* $P(E_{int})$: θ = 30,715 cm^{-1}. See also Table I.

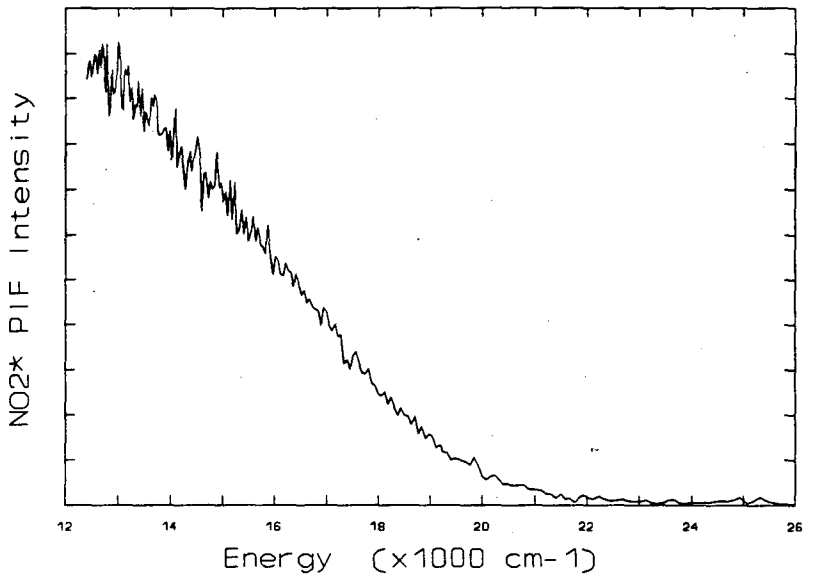

Figure 6. 210nm CH_3NO_2 NO_2^* PIF spectrum.

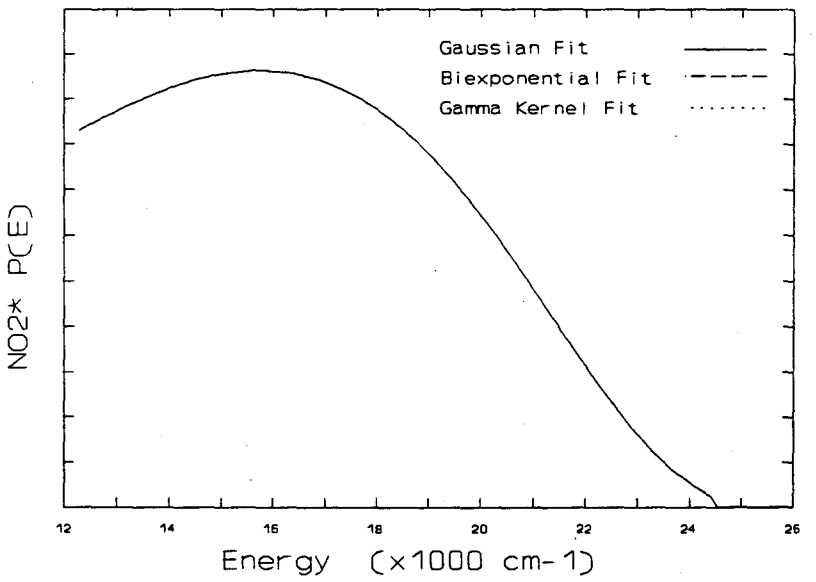

Figure 7. 210nm CH_3NO_2 NO_2^* $P(E_{int})$: θ = 26,000 cm^{-1}. See also Table II.

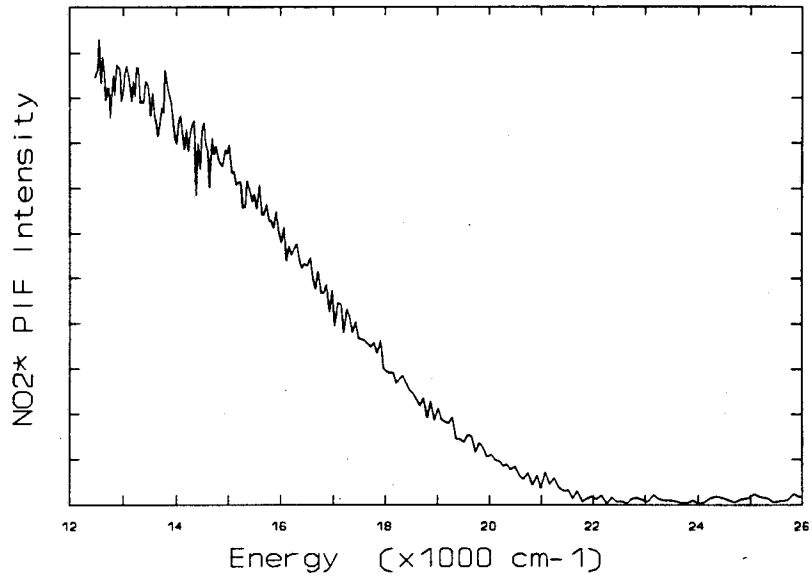

Figure 8. 224nm CH_3NO_2 NO_2^* PIF spectrum.

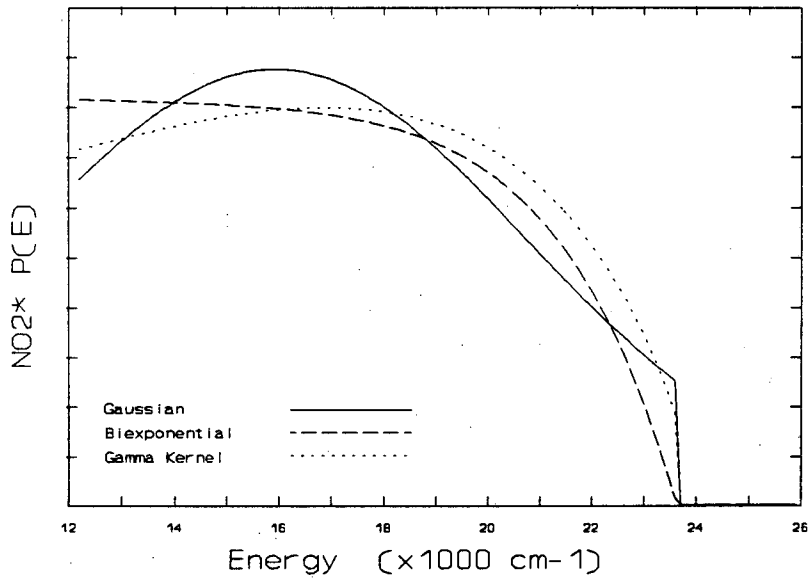

Figure 9. 224nm CH_3NO_2 NO_2^* $P(E_{int})$: θ = 23,625 cm^{-1}. See also Table III.

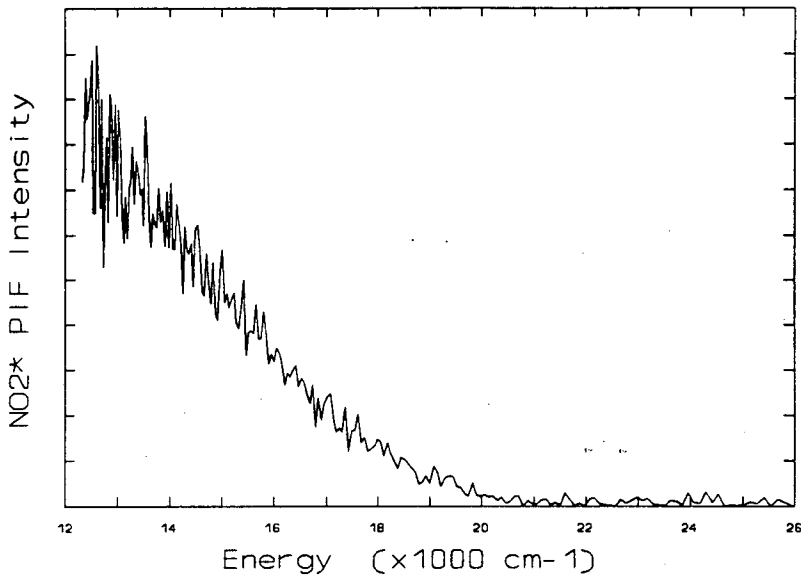

Figure 10. 235nm CH_3NO_2 NO_2^* PIF spectrum

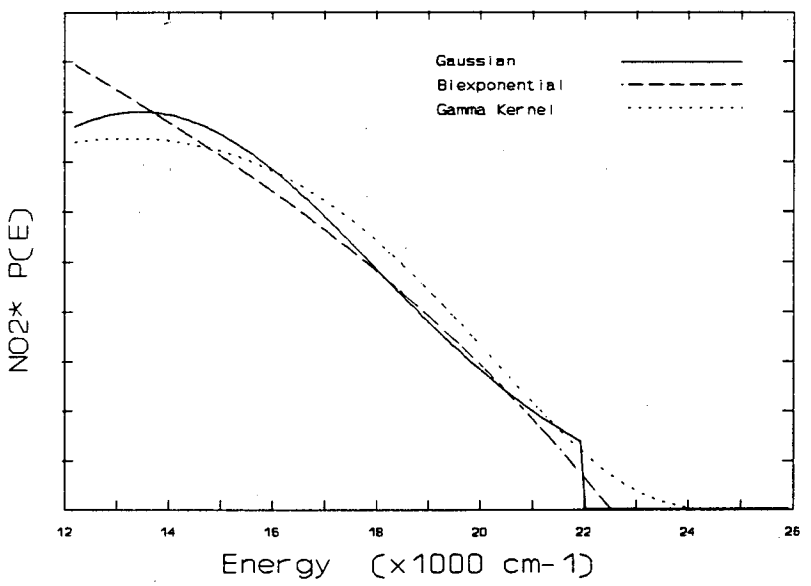

Figure 11. 235nm CH_3NO_2 NO_2^* $P(E_{int})$: θ = 21,535 cm^{-1}. See also Table IV.

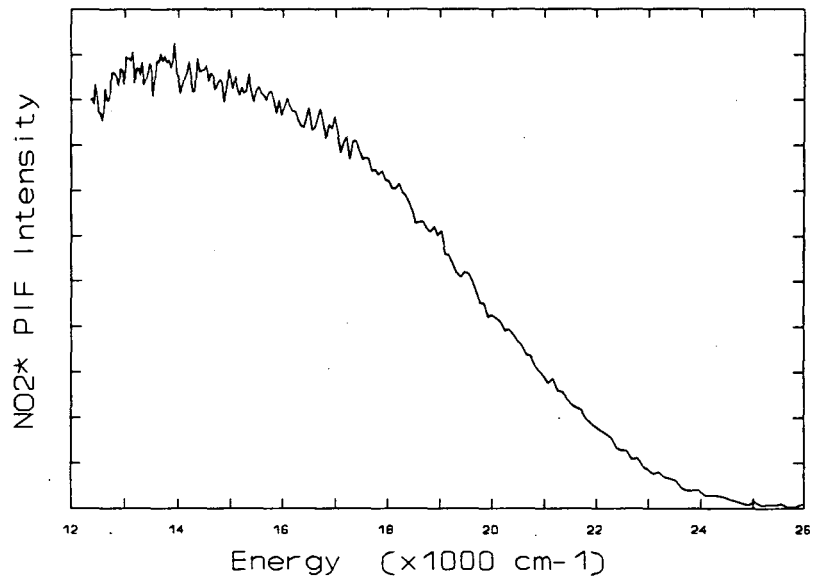

Figure 12. 193.3nm Nitroethane NO_2^* PIF spectrum.

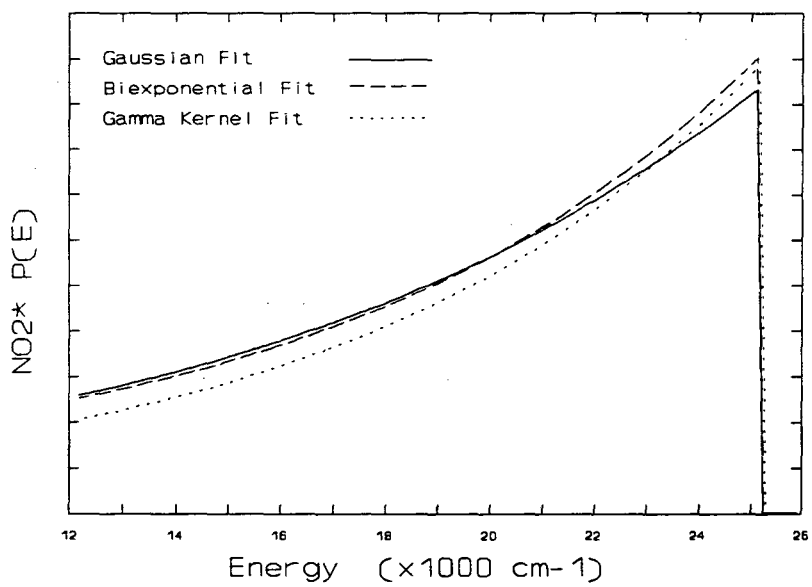

Figure 13. 193.3nm nitroethane NO_2^* $P(E_{int})$: θ = 30,475 cm^{-1}. See also Table V.

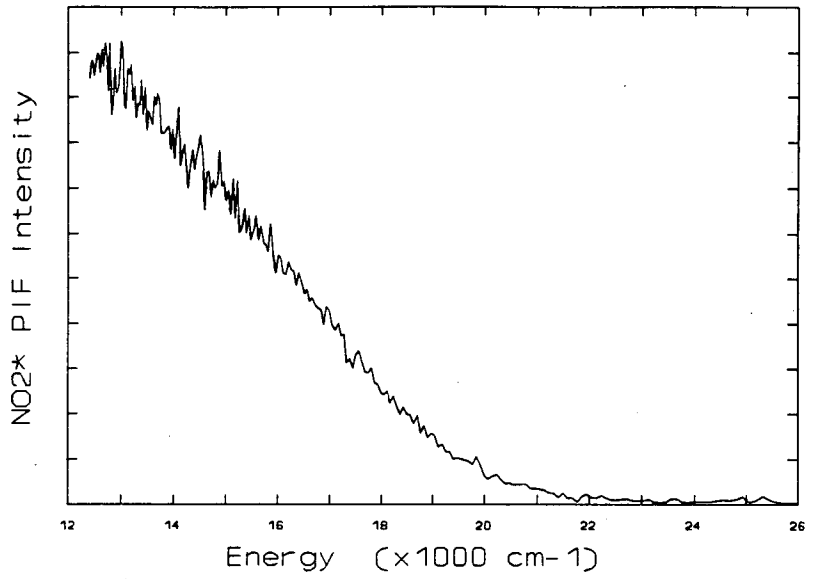

Figure 14. 224nm Nitroethane NO_2^* PIF spectrum.

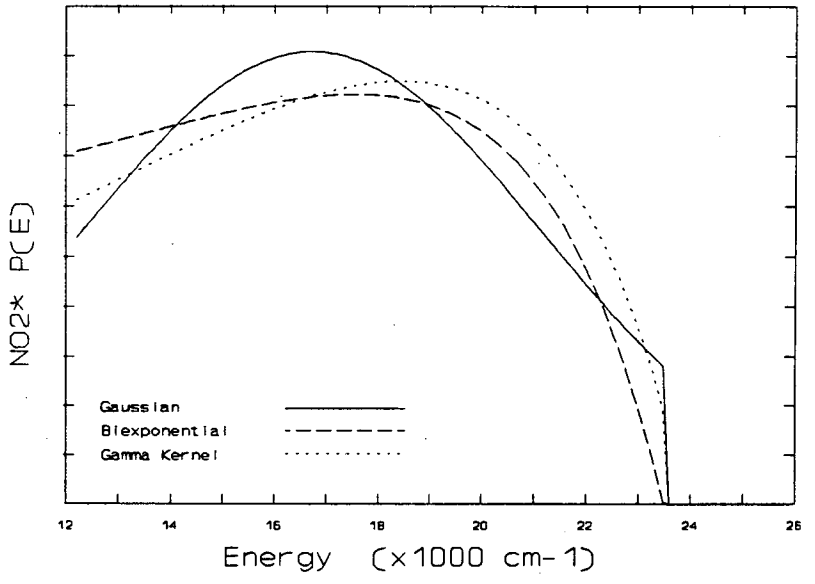

Figure 15. 224nm Nitroethane NO_2^* $P(E_{int})$: θ = 23,485 cm^{-1}. See also Table VI.

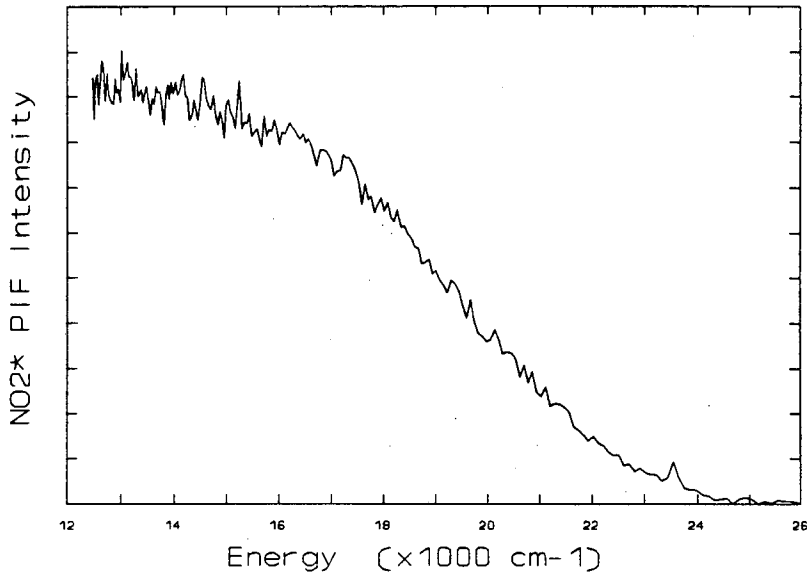

Figure 16. 193.3nm Nitropropane NO_2^* PIF spectrum.

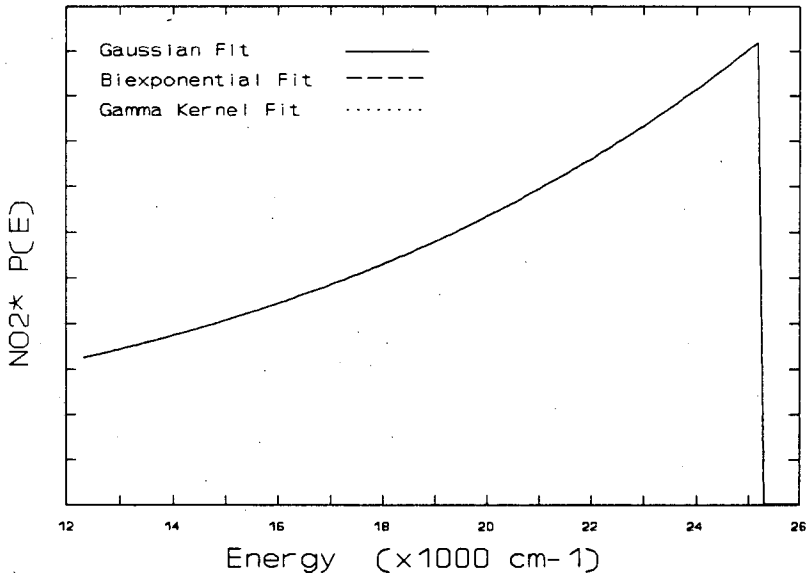

Figure 17. 193.3nm 1-nitropropane NO_2^* $P(E_{int})$: θ = 31,130 cm^{-1}. See also Table VII.

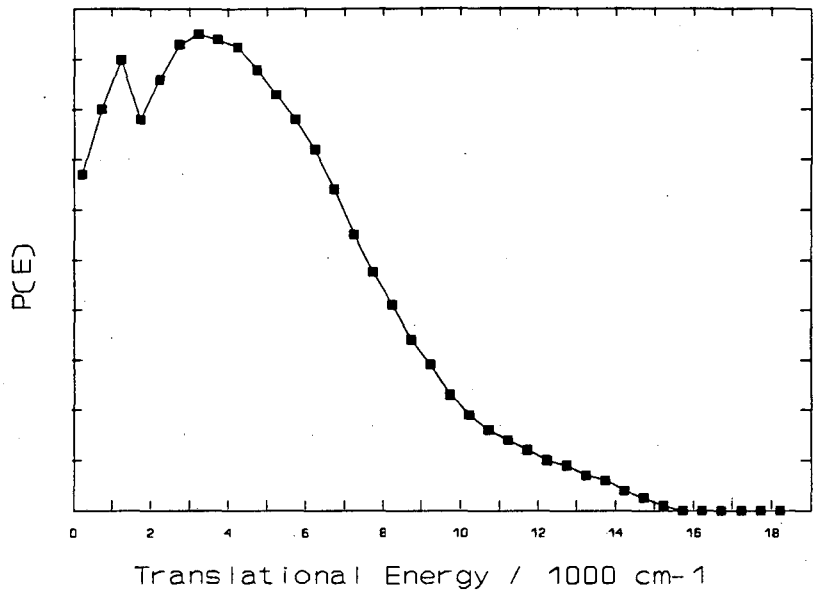

Figure 18. TOF $P(E_T)$ derived for 193.3nm CH_3NO_2 photodissociation [Ref. 1]. θ = 30,715 cm^{-1}.

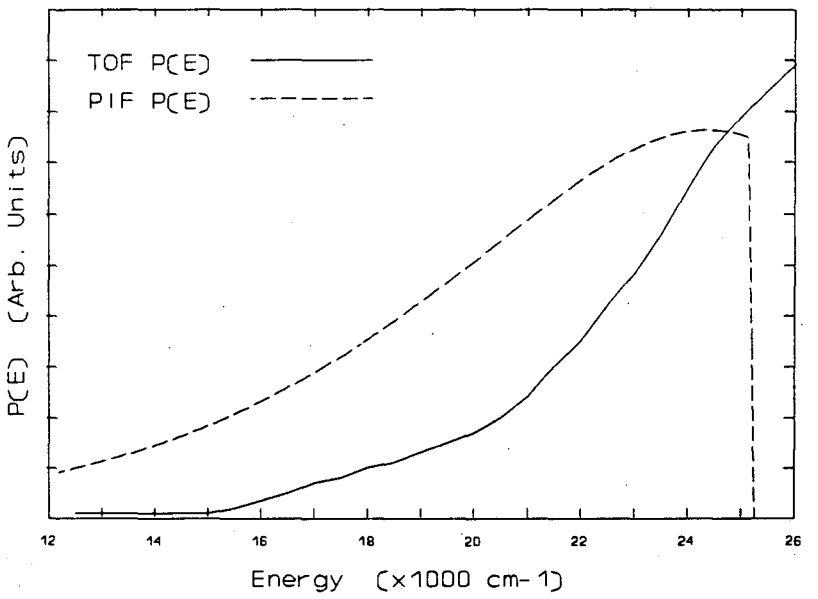

Figure 19. IF NO_2^* $P(E_{int})$ and TOF $P(E_{int})$ [adapted from Ref. 1] derived for 193.3nm CH_3NO_2 photodissociation. θ = 30,715 cm^{-1}.

CHAPTER 3:

Variable Wavelength Photodissociation of $ClNO_2$ and $HONO_2$

3.0 ABSTRACT

The photolysis induced fluorescence (PIF) method is used to derive internal energy distributions, $P(E_{int})$, for the fluorescing NO_2 ensembles (NO_2^*) from $ClNO_2$ and $HONO_2$ photodissociations as a function of the photolysis wavelength. The NO_2^* $P(E_{int})$'s for $ClNO_2$ evolve from distributions peaked at 25,130 cm^{-1} to those having a majority of the NO_2^* components with internal energies less than 15,000 cm^{-1} as the energy available to the photofragments decreases from 30,000 to 20,000 cm^{-1}. The NO_2^* $P(E_{int})$ distributions derived for $HONO_2$ are dominated by components with energies less than 15,000 cm^{-1} and only for photolysis wavelengths shorter than 255nm do the distributions have significant contributions from NO_2^* components approaching the maximum available energy. The PIF $P(E_{int})$ derived from 308nm $ClNO_2$ photodissociation are compared to the $P(E_T)$ distribution derived from time of flight experiments, and the $HONO_2$ PIF $P(E_{int})$ distributions are compared to energy partitioning measurements made after 241 and 280nm photolysis. Examination of the $ClNO_2$ and $HONO_2$ absorption spectra in conjunction with the observed energy partitioning and theoretical calculations demonstrates that the R group perturbation on the local C_{2v} symmetry of the NO_2 chromophore determines the differences between $ClNO_2$ and $HONO_2$ photolysis.

3.1 INTRODUCTION

Nitric acid is an important molecule in atmospheric photochemistry cycles, including the catalytic decomposition of ozone, serving as storehouse for both HO_x and NO_x [1]. Graham and Johnston[2] found that the $HONO_2$ UV absorption spectrum, shown in Figure 1, consists of a broad, structureless continuum with maxima at 200 (σ = 1 x 10^{-17} cm^2) and 270 nm (σ = 1 x 10^{-20} cm^2). Johnston, Chang, and Whitten[3] measured unit quantum yield for the production of NO_2 from $HONO_2$ photodissociation between 200 and 300nm. Jolly et al.[4] measured a 0.89 $\pm$ 0.08 OH quantum yield at 222 nm and inferred an identical NO_2 production. Nelson, Schiffman, and Nesbitt[5] determined ϕ(OH) = 0.42 at 193.3nm and 0.8 - 1.0 at 248.5nm using infrared detection of the OH radical. In an interesting study Suto and Lee[6] measured the $HONO_2$ cross sections for absorption and NO_2 fluorescence and found that the quantum yield for NO_2^* emission rises nearly linearly from a value of 0.1% at 180nm to a value of 0.35% at 200nm. The cross section for NO_2^* production peaks at 195nm ($\sigma(NO_2^*)$ = 4x10^{-20} cm^2 $molecule^{-1}$) and is less than 1x10^{-20} cm^2 $molecule^{-1}$ at 220nm. Thermodynamic thresholds for relevant dissociation channels are given in Figure 2.

There are two important $HONO_2$ photodissociation studies using near UV wavelengths. Crim and coworkers[7] employed a sequential two-color vibrationally mediated photodissociation (VMP) via the third OH stretching overtone in $HONO_2$ (755nm overtone excitation + 355 nm photolysis) and an isoenergetic single photon

excitation at 241 nm with LIF detection of the OH fragment. They infer that the NO_2 fragment has about 21,000 cm^{-1} of internal energy after single photon dissociation, but only 19,500 cm^{-1} after VMP from the scalar properties of the OH LIF measurements. They also detected NO_2^* fluorescence during each process. August et al.[8] used OH LIF probing to investigate the 280nm $HONO_2$ photodissociation. Their energy partitioning results infer that the NO_2 fragments have a Gaussian distribution of internal energies with a mean value of 12,590 cm^{-1} and a FWHM of 6570 cm^{-1}.

Bai and Segal[9] have used large scale *ab initio* configuration interaction calculations to determine the potential energy surfaces corresponding to the four lowest singlet states of $HONO_2$ along the dissociation paths correlating to OH ($^2\Pi$) and NO_2 in its X $^2A_1$ and A $^2B_2$ states. The results of this calculation are given in Figure 3 and Tables I and II. One can see that extrapolation of the potential surfaces in Figure 3 that the two lowest $HONO_2$ surfaces correlate to $NO_2(^2A_1)$ while the 2 $^1A''$ (and the unshown $2^1A'$) surface correlates to $NO_2(^2B_2)$ products. These calculations verify the conclusion of August et al.[8] that 280nm excitation of $HONO_2$ accesses an electronic transition of A′ symmetry and that the transition is promoted primarily by a vibronic mechanism involving pyramidal distortion of the $HONO_2$ molecule. The vertical transition energies and oscillator strengths from this calculation are in good agreement with the experimental absorption spectrum and indicate that the $HONO_2$ absorptions in the 230 - 280nm range contain transitions only to the A $1^1A''$ and B $2^1A''$ surfaces. Transitions to the C $2^1A'$ surface are not energetically possible over this range.

Nitryl chloride, $ClNO_2$, is another molecule important to atmospheric photochemistry cycles. In addition to contributing to the NO_x pool, $ClNO_2$ photolysis releases chlorine atoms which can catalytically destroy ozone[1]. The $ClNO_2$ UV absorption spectrum[10,11,12], illustrated in Figure 4, is more intense and extends to longer wavelengths than the $HONO_2$ spectrum. Hunter and Johnston[12] have found that in addition to the three broad maxima centered at 190nm (σ = $5x10^{-17}$ cm^2 $molecule^{-1}$), 225nm (σ = $5x10^{-18}$ cm^2 $molecule^{-1}$), and 300nm (σ = $2x10^{-19}$ cm^2 $molecule^{-1}$) there is a previously unreported vibronic progression with 318 cm^{-1} spacing superimposed on the absorption continuum between 270 and 230nm. This spacing resembles the ν_5 mode in the $ClNO_2$ groundstate, which is a planar NO_2 wagging motion. Thermodynamic thresholds for relevant dissociation channels are given in Figure 5.

Despite the fact that $ClNO_2$ is isovalent to $HONO_2$, there have been relatively few investigations of its photochemistry reported in the literature. Nelson[11] measured the Cl and O atom quantum yields for 355nm $ClNO_2$ photolysis and found $\phi(Cl) = 0.93 \pm 0.15$ and $\phi(O) < 0.02$. Oh[13], Sisk[14], and Johnston et al.[15] have investigated the $ClNO_2$ photodissociation at 193.3, 248.5, and 266nm at room temperature and in a supersonically cooled molecular jet. The results of these studies suggest that the NO_2^* $P(E_{int})$ distributions from 193.3 and 248.5nm photodissociations are peaked at 25,130 cm^{-1} and decrease to one fourth their maximum value for components having ~12,500 cm^{-1} of internal energy. The 266nm NO_2^* $P(E_{int})$ was found to peak near 22,000 cm^{-1} and have a nearly gaussian contour. Covinsky[16] derived $P(E_T)$ distributions for the 248.5 and

308nm $ClNO_2$ photodissociations from time of flight measurements. Both $P(E_T)$ showed that the NO_2 distribution is distinctly bimodal and that the 248.5nm PIF $P(E_{int})$ displayed the correct qualitative features of the NO_2^* portion of the distribution (12,000 cm^{-1} < E_{int} < 25,130 cm^{-1}). The bimodality of the $P(E_{int})$ was attributed to a branching of the dissociation pathway into channels correlating groundstate electronically excited NO_2 products.

The present study is a continuation of our laboratory's investigation of R-NO_2 photodissociation and is principally concerned with determining the dependence of NO_2^* $P(E_{int})$ distributions on the available energy, $\theta = h\nu - D_0(R\text{-}NO_2)$. The θ values of interest are between 20,000 and 30,000 cm^{-1}. We wish to understand how the NO_2^* $P(E_{int})$ evolves as θ approaches the 25,130 cm^{-1} NO_2 predissociation limit, and if there are any noticeable transformations in $P(E_{int})$ when $\theta \approx D_0(NO_2)$. Additionally, we can control the photodissociation wavelengths to generate $ClNO_2$ and $HONO_2$ dissociations having nearly equivalent θ and appraise the influence of the R fragment on the energy partitioning.

3.2 EXPERIMENTAL

Experiments were conducted with the standard PIF/collisional deactivation cell configuration and collection optics[17]. The R-NO_2 sample flowed through a pyrex cell at pressures between 10 and 200 millitorr. Pressures are regulated by placing the sample

in a low temperature bath (0 to -30 C, variable, Neslab cryogenic cooling unit) and controlling the sample flow rate into the photolysis cell. The photodissociation laser passes through two collinear windows which are mounted at Brewster's angle to minimize scattering of the laser light. The collection window is orthogonal to the other two and opposite a large Wood's horn to further suppress the collection of scattered light.

The tunable light used in these experiments is generated from an excimer pumped dye laser system (Questek 2220 excimer pumping a Lumonics HyperDye 300 dye laser) and produces visible light with a bandwidth of 0.1 cm^{-1}. The frequency of the dye laser is harmonically doubled using a BBO non-linear mixing crystal. The visible and UV frequencies are separated using a commercial unit (Lumonics HyperTrak HT-1000). The UV output of this system was typically 1-2 millijoules per pulse ($\sim$10% conversion efficiency) and had an ellipsoidal beam shape measuring roughly 1mm by 3mm. The laser system duty cycle was usually 20 Hz.

A 13cm f/1.0 lens collects and images the fluorescence profile from the photolysis cell onto the entrance slit of a one meter grating monochromator (Interactive Technologies using a 1200 lines/mm grating blazed at 500nm). The large diameter/short focal length collection lens is required to exploit the full 5cm slit height available on the monochromator. Slit lenses on both the entrance and exit slits maintain proper focussing of the fluorescence image through the monochromator. A 7cm f/1.5 lens images the exit slit image onto the photocathode of a PMT (RCA C31034-A or Hammamatsu R1447).

The fluorescence signal is amplified by an Avantec amplifier and passed to a boxcar integrator (Stanford Research Systems SR250) for collection.

Time synchronization is established by the signal from a silicon photodiode which samples a portion of the laser beam immediately after it passes through the photolysis cell. This photodiode signal is also integrated to provide pulse-to-pulse laser power normalization for the fluorescence signal. An IBM AT computer controls the entire data acquisition process using a Data Translation DT2801-A D/A board. Typical experimental trials consist of 220 points collected at 2nm intervals from 380 to 820nm. The NO_2^* fluorescence intensity at each wavelength is the average of 100 to 200 laser shots and has been corrected for laser power fluctuations.

The optical collection system was calibrated for absolute spectral sensitivity using a tungsten lamp to provide black body radiation. The temperature of the source was determined with an optical pyrometer, and was generally near 1600 C; the uncertainty in this measurement is typically $\pm$ 20 C. Spectra of the tungsten lamp emission were then recorded over the 380 - 820nm range used in PIF experiments. The system response profile was determined from these scans and the literature values for tungsten lamp emissivity[18]. The averaged PIF spectra were corrected for the system's wavelength dependent spectral sensitivity prior to analysis. The PMT's used in these experiments had quantum efficiencies which decreased rapidly for wavelengths longer than 780nm, therefore the system response correction mainly increases the fluorescence intensities

observed below 15,000 cm^{-1}.

The specific conditions for each photodissociation experiment are given in Tables III and IV. Larger sample pressures and longer gate widths were generally required to compensate for the decreasing yield of NO_2^* signal as the photodissociation wavelength was increased. Note from Figures 1 and 4 that the absorption cross sections decrease with increasing wavelength, although it appeared in some cases that the total NO_2^* signal was decreasing faster than the absorption cross sections might indicate.

$ClNO_2$ was synthesized using the procedures outlined by Nelson[19]. Anhydrous HCl (Matheson) was streamed over a 196 K cold trap (dry ice/acetone) to remove any traces of water or other volatile impurities. The HCl then passed through a porous glass frit into a vigorously stirring mixture of 25 ml 90% $HONO_2$ (Baker), 60 ml 95% H_2SO_4 (Fischer), and 70 ml fuming H_2SO_4 (30% SO_3; Fischer). The $ClNO_2$ evolving above the stirring mixture was collected in a second 196 K trap, while the non-condensing gases were discarded. A $CaSO_4$ scrubber prevented water vapor from backstreaming into the trap containing the raw $ClNO_2$ product. The reaction was carried out at ambient pressure inside a fume hood. The flow rate of HCl was regulated to maintain a positive pressure inside the apparatus and insure adequate mixing in the acid solution. The reaction was continued until about 8 - 10 ml of product had been obtained.

The unrefined $ClNO_2$ product was separated from other reaction products (ClNO,

Cl_2) by fractional distillation on a standard vacuum line. The unprocessed product mixture was placed in a 175 K liquid nitrogen/methanol slush and the sample was drawn through a 77 K (liquid nitrogen) collection trap. The initial 3ml fraction is discarded due to high Cl_2 impurity, the middle third is kept for experiments, and the remnants in the 175 K trap are discarded due to NO_2 contaminants. After fractionation, the refined $ClNO_2$ was still a pale yellow, but it had lost the greenish tint that characterized the raw product; there is a slight Cl_2 impurity that is virtually impossible to remove due to the similar temperature dependencies of Cl_2 and $ClNO_2$ vapor pressures. The samples used in this study were estimated to be 90% $ClNO_2$ based on comparisons of absorption cross sections with literature values[8-10]. Samples were stored at 77 K when not in use to avoid thermal decomposition. Nelson[19] provides an excellent discussion of the reaction mechanism and the potential problems encountered in the synthesis and purification procedures.

Anhydrous $HONO_2$ was synthesized using established procedures[20]. About 10 g of pulverized KNO_3 was added to 250 ml of 95% H_2SO_4 (Fischer) in a 500 ml roundbottom flask. The acid mixture is stirred vigorously and heated slightly above room temperature (35 - 40 C). The reaction is initiated by subjecting the contents to a slight vacuum. A noticeable frothing of the reaction mixture signals $HONO_2$ production. $HONO_2$ evolves from the reaction mixture and is collected in a -40 C cold trap. Care must be taken not to heat the reaction mixture to temperatures above 40 C to avoid distilling water and H_2SO_4 into the collection trap. The reaction expires after 20 - 30

minutes. The pure $HONO_2$ contained in the collection trap is stored at 77 K and in the dark until required. Great caution must be exercised when handling the pure $HONO_2$ because it is highly corrosive. Therefore, the amount of stainless steel in the sample introduction line was always minimized prior to $HONO_2$ experiments. When $NaNO_3$ is used in this synthesis, it also generates gaseous NO_2, making it an inappropriate substitute for KNO_3.

3.3 RESULTS

Individual PIF spectra averaging 200 laser shots per point were corrected for the optical system's spectral sensitivity and accumulated into single files for analysis. The accumulated PIF spectrum represents between 600 and 1200 laser shots averaged per point, depending on the specific experiment. These spectra were then analyzed using the integrated fluorescence (IF) method and weighting functions described in Chapter 1.

Preliminary data analysis revealed that the small noise levels recorded in those experiments which had fluorescence thresholds inside the observation region ($25{,}130 > \theta > 12{,}500$ cm^{-1}) were corrupting the parameter optimization algorithm by generating non-zero contributions to the cumulative integrated fluorescence function at energies above θ. We addressed this problem by manually zeroing all fluorescence intensity elements having energies either above $\theta + 1500$ cm^{-1}, designated the $\theta+$ files, or above θ, designated the θ files. This eliminates fluorescence contributions from the

inaccessible energy regions. Optimized parameter sets for the IF weighting functions were subsequently determined for these edited data.

The Gaussian weighting function presented in Chapter 1 was modified slightly to incorporate the possibility of θ values less than 25,130 cm^{-1}. The modification requires the inclusion of a parameter M, as in the biexponential and gamma kernel functions, except that M in this case serves only as a boundary marker. All population components having energies greater than M identically equal zero. Population components having energies less than M remain unaffected. This modification enables the IF optimization algorithms to seek the best set of fitting parameters without being penalized for calculating contributions to the cumulative integrated fluorescence intensity function at energies above θ.

3.3.A. $HONO_2$

The $HONO_2$ PIF spectra for photodissociations between 235 and 280nm are presented in Figures 6 - 17. As θ decreases from 26,055 cm^{-1} for the 235nm photolysis (Figure 6) to 19,215 cm^{-1} for the 280nm photolysis (Figure 17), the high energy threshold for fluorescence also decreases. In each experiment there are some NO_2^* components with energies up to θ, but the majority of the emission is found for energies less than 16,000 cm^{-1} regardless of θ. The concentration of fluorescence intensity in low energy NO_2^* components is increasingly evident for photolysis wavelengths longer than 255nm

(Figures 12-17). The $HONO_2$ PIF spectra have proportionately more of their NO_2 fluorescence intensity in the 12,000 - 16,000 cm^{-1} portion of the spectrum than any other nascent R-NO_2 PIF spectra recorded to date. As seen in Figures 12-17, the spectra obtained using photodissociation wavelengths longer than 255nm appear to have fluorescence maxima at energies below 12,000 cm^{-1}. Note, however, that in each experiment the onset of fluorescence corresponds almost exactly to θ. The expected increase in fluorescence intensity as the observation bin decreases from θ is also uncharacteristically small. This marked red shift of the PIF spectra persists even for the experiments at 235 and 238nm (Figures 6 and 7) in which the channels corresponding to secondary dissociation of the NO_2 fragment into NO + O are energetically accessible.

Figures 18 and 19 provide comparisons of the $P(E_{int})$ derived from the gamma kernel weighting function for 245 and 265nm $HONO_2$ photodissociations. These figures show that the $P(E_{int})$ derived from the edited and unedited data are qualitatively and quantitatively quite similar. We attribute the small differences between the distributions to unrealistic discrepancies forced on the optimization algorithm for the unedited data due to noise contributions to the cumulative IF function at energies above θ. The $P(E_{int})$ derived from the θ edits of the data should, therefore, be regarded as the most physically correct populations. These data were chosen as the best representation of the experiments because they have been manually zeroed for observation bins above the energetic threshold for fluorescence, so that the IF optimization is not corrupted by non-zero noise levels.

The optimized IF analysis fitting parameters derived from the full and edited data presented are given in Tables V-XVI. In addition to the actual fitting parameters, these Tables provide fitting residuals and statistical measures for each NO_2^* $P(E_{int})$ distribution. These numbers are useful for comparing the agreement between the calculated and experimental cumulative integrated fluorescence functions and NO_2^* $P(E_{int})$ distributions derived for each photodissociation wavelength. A quick survey of Tables V (235nm PIF) and XVI (280nm PIF) shows that the 235nm parameters produce lower sum errors, hence slightly better fits, than the 280nm parameters. One also notices that while both $P(E_{int})$ distributions peak at 12,195 cm^{-1}, the low observation energy boundary, the 235nm $P(E_{int})$ has an average energy which is about 2000 cm^{-1} larger than the 280nm $P(E_{int})$. Looking again at the 235 and 280nm $HONO_2$ PIF spectra in Figures 6 and 17, it is obvious that the 235nm photodissociation produces a more energetic NO_2^* ensemble, but one requires the information in Tables V and XVI to quantify this difference. A comparison of the $HONO_2$ PIF experiments corresponding to the largest and smallest θ values exaggerates the trends seen in Figures 6-17 and Tables V - XVI, but there is a very real shift in the NO_2 PIF spectra as a function of θ and the average and rms energies of the $P(E_{int})$ distributions mirror this gradual change.

Figures 20-31 provide sketches of the preferred NO_2^* $P(E_{int})$ distributions and are complementary to the information contained in Tables V-XVI. These plots depict the full NO_2^* $P(E_{int})$ distributions calculated from the optimized IF parameters. For the 235 and 238nm experiments θ is greater than $D_0(NO_2)$, so the data were not edited and Figures

20 and 21 illustrate the $P(E_{int})$ derived from each weighting function for these experiments. One can clearly see the decreasing energy associated with the NO_2^* ensemble as the $HONO_2$ photolysis wavelength increases.

The $HONO_2$ $P(E_{int})$ distributions in Figures 22-31 indicate an even more pronounced concentration of the NO_2^* components at energies below 15,000 cm^{-1} than suggested by the PIF spectra in Figures 6-17. Further examination of the $P(E_{int})$ in Figures 22-31 reveals that there are apparently two sets of NO_2^* $P(E_{int})$ distributions derived from the $HONO_2$ experiments. Photodissociations using wavelengths shorter than 255nm (θ > 22,700 cm^{-1}) produce a $P(E_{int})$ maximum inside the observation window and have non-negligible NO_2^* components with energies greater than 20,000 cm^{-1} (see Figures 20-24). Experiments having photodissociation wavelengths longer than 255nm (θ < 22,700 cm^{-1}) produce $P(E_{int})$ distributions with most of the NO_2^* components at energies lower than the 17,000 cm^{-1}. Figures 26-31 show that these $P(E_{int})$ distributions have minimal contributions from NO_2^* components with energies near θ and maxima at the lowest energy allowed by the IF boundary constraints, suggesting that the true population maxima are found at energies below 12,000 cm^{-1}. The statistical measures for this second category of NO_2^* $P(E_{int})$ distributions, given in Tables XI-XVI, should thus be considered as upper bounds to the full $HONO_2$ NO_2^* $P(E_{int})$ distributions for these experiments.

The optimized weighting functions generate similar $P(E_{int})$ distributions for any given experiment. Despite the fact that the gamma kernel is the most flexible functional

form, Tables V - XVI show that the Gaussian weighting function produces slightly lower fitting residuals for most of the $HONO_2$ experiments.

3.3.B. $ClNO_2$

The $ClNO_2$ PIF spectra for photodissociations between 235 and 308nm are presented in Figures 32-43. These spectra are more characteristic of the previously recorded R-NO_2 PIF spectra: the NO_2 PIF intensity increases rapidly from its short wavelength onset, reaches a maximum, and begins to decrease within the experimental observation window. This pattern is obvious in Figures 32-40 for $ClNO_2$ photodissociations with wavelengths shorter than 280nm. These figures also illustrate the shift in the NO_2^* spectral distributions with decreasing θ as the fluorescence intensity maximum moves to successively lower energies, and finally out of the observation window. The low θ values associated with the 290, 300, and 308nm $ClNO_2$ photodissociations (Figures 41-43) produce PIF spectra reminiscent of the $HONO_2$ PIF spectra, where most of the fluorescence is observed at energies below 16,000 cm^{-1}. It is important to note that all of the $ClNO_2$ PIF spectra have NO_2^* components fluorescing at energies up to θ. This again provides evidence that the NO_2^* $P(E_{int})$ distributions are very energetic and that there will be minimal energy partitioned into other degrees of freedom during the dissociation.

The optimized fitting parameters derived from the IF analysis for the full and

edited $ClNO_2$ data are given in Tables XVII - XXVIII and the associated plots of the complete NO_2^* $P(E_{int})$ distributions are shown in Figures 44-56. This information quantifies the differences between $ClNO_2$ and $HONO_2$ photodissociation energy partitioning which we inferred from the PIF spectra. The $ClNO_2$ NO_2^* $P(E_{int})$ distributions show a much more interesting θ dependence than the $HONO_2$ $P(E_{int})$ because $ClNO_2$ dissociation deposits substantially more energy in the NO_2 fragment.

The $ClNO_2$ NO_2^* $P(E_{int})$ distributions metamorphisize through several distinguishable contours as θ varies. When θ is well above $D_0(NO_2)$, the resulting NO_2^* $P(E_{int})$ peaks at $D_0(NO_2)$ and decreases "exponentially" to about 20% of the peak value for less energetic NO_2^* components - see Figures 44-49 for the 235 to 260nm $P(E_{int})$. When θ is near $D_0(NO_2)$, the $P(E_{int})$ maximum moves to energies within the observation window and is well represented by Gaussian-like contours, as shown for the 275 and 280nm experiments in Figures 52 and 53. The $P(E_{int})$ distributions for $\theta <$ 23,000 cm^{-1}, see Figures 54-56, have maxima which are near or below the 12,000 cm^{-1} low energy limit of the IF analysis. However, contrary to the $HONO_2$ NO_2^* $P(E_{int})$ distributions, even the lowest θ $ClNO_2$ $P(E_{int})$ have significant contributions from NO_2^* components near θ.

As with the $HONO_2$ IF analysis, the Gaussian and gamma kernel $P(E_{int})$ agree very well. For those experiments with θ less than $D_0(NO_2)$, the chopped Gaussian and gamma kernel are nearly equivalent. Even the biexponential weighting function $P(E_{int})$

distributions agree well with the other $P(E_{int})$ for the 260, 270, and 280nm photodissociations. The agreement of all three weighting functions and the significant NO_2^* PIF signals observed above 20,000 cm^{-1} indicate that the NO_2^* ensemble is highly inverted. This is probably also true for shorter wavelength dissociations, but we can only infer NO_2^* populations for energies greater than $D_0(NO_2)$.

3.4 DISCUSSION

We undertook these experiments for two main reasons. Firstly, we wished to determine the θ dependence for the NO_2^* $P(E_{int})$ from the photodissociation of a single R-NO_2 molecule. Secondly, we wanted to compare the $P(E_{int})$ distributions derived from different R-NO_2 photodissociations which produce nearly equivalent θ values. Nitryl chloride and nitric acid are ideal for this purpose. $ClNO_2$ is an example of the simplest possible R-NO_2 photodissociation since the atomic Cl fragment receives only translational excitation during the energy partitioning process. (This assumption neglects the participation of Cl spin-orbit excitation in energy partitioning, a possible error of 882 cm^{-1}.) Nitric acid, with its diatomic OH fragment, is the simplest example of R-NO_2 photodissociation where R has internal degrees of freedom that can participate in energy partitioning. The R-NO_2 bond dissociation energies of $ClNO_2$ and $HONO_2$, 11,866 and 16,500 cm^{-1} respectively, also generate θ values of $D_0(NO_2) \pm 6000$ cm^{-1} as the photodissociation wavelength is varied from 235 - 308nm.

3.4.A. $HONO_2$

The small absorption cross sections between 250 and 280nm, the low NO_2^* PIF intensities, and the overwhelming concentration of the NO_2^* components at energies below 15,000 cm^{-1} indicate that the dominant channel in near UV $HONO_2$ photodissociation does not correlate to electronically excited NO_2 products. The *ab initio* calculations of Bai and Segal[9] reveal that only transitions to the $1^1A''$ and $2^1A''$ electronically excited $HONO_2$ potential energy surfaces are possible for photon energies below 40,000 cm^{-1}. As suggested by the curves in Figure 3, the $1^1A'$ and $1^1A''$ surfaces correlate to $OH(^2\Pi)$ + $NO_2(^2A_1)$ while the $2^1A''$ surface correlates to $OH(^2\Pi)$ + $NO_2(^2B_2)$. The $1^1A' \rightarrow 1^1A''$ and $1^1A' \rightarrow 2^1A''$ vertical transitions are calculated to have energies of 37,000 and 45,000 cm^{-1} and oscillator strengths of $2x10^{-6}$ and $4x10^{-5}$, respectively. Bai and Segal[9] also calculated that $1^1A' \rightarrow 1^1A''$ transitions which accessed the favored pyramidal geometries on the $1^1A''$ surface had oscillator strengths of $1x10^{-4}$, 50 times larger than the vertical transition. This result is in agreement with the vector correlation measurements of August et al.[8] who concluded that the 280nm $HONO_2$ photodissociation occurs via a vibronic transition that pyramidally distorts the $HONO_2$ molecule from its equilibrium configuration.

Dissociation along the $1^1A''$ surface would also be consistent with the exceptionally low internal energies seen in the NO_2^* $P(E_{int})$ distributions. We treat the apparent contradiction of electronically excited NO_2 products from excitations to the $1^1A''$

surface by noting that this transition is an $n \rightarrow \pi^*$ type localized on the NO_2 moiety and would correlate to the production of NO_2^* products if the local C_{2v} geometry of the NO_2 chromophore was preserved in the $HONO_2$ molecule. The calculated geometries presented in Tables I and II illustrate this point. The $HONO_2$ $1^1A''$ minimum energy configurations have local NO_2 geometries resembling $NO_2(^2B_2)$ - R_{NO} = 1.28 Å, ϕ = 102° - rather than $NO_2(^2A_1)$ - R_{NO} = 1.19 Å, ϕ = 134°. Table II also illustrates the presence of C_s symmetry induced avoided crossing in the exit channel of the $1^1A''$ surface. The $\angle$ ONO increases by 20° and the R_{NO} bond length decreases by 0.08 Å in the NO_2 chromophore as R_{HO-N} increases from 1.60 to 2.00 Å along the $HONO_2$ dissociation coordinate. Non-adiabatic mixing in the exit channel could cause some reactive trajectories to preserve the NO_2^* character of the bound portion of $1^1A''$ surface. This type of leakage in the exit channel is also supported by the fact that the calculated minimum of the $1^1A''$ surface lies 1000 cm^{-1} above the energetic threshold for the production of $NO_2(^2B_2)$.

The increase in NO_2^* components having energies greater than 15,000 cm^{-1} for $HONO_2$ photodissociation wavelengths shorter than 255nm, as seen in Figures 20-25, suggests that dissociation channels correlating directly to NO_2^* products provide increased contributions to these $HONO_2$ dissociations. The change in the NO_2^* $P(E_{int})$ behavior can also be seen in Figure 56 which displays the average energy of the NO_2^* ensemble as a function of θ. The sudden increase in $<E(NO_2^*)>$ at $\theta \sim 23{,}000$ cm^{-1} matches the observed change in the NO_2^* $P(E_{int})$ contours which begins at 22,715 cm^{-1} (255nm).

Interpolation of the surface points given in Table II shows that the $1^1A' \rightarrow 2^1A''$ vertical transition when $R_{HO\text{-}N}$ = 1.39 Å has an energy of 39,400 cm^{-1}, corresponding to a 253.8nm photolysis wavelength. The PIF $P(E_{int})$ distributions imply that the $2^1A''$ surface does not substantially influence $HONO_2$ photodissociation dynamics until single photon excitation energies approach 39,000 cm^{-1}, although the calculated minimum energy for this surface is 36,600 cm^{-1}. This conclusion is supported by the sudden increase in absorption cross sections seen in Figure 1 beginning at 240nm or ~42,000 cm^{-1}.

The $HONO_2$ NO_2^* $P(E_{int})$ distributions derived for photodissociation wavelengths shorter than 255nm exhibit increasing contributions from the $2^1A''$ surface and its more energetic NO_2^* products, but the contributions of low energy NO_2^* components implies that dissociations on the $1^1A''$ surface are still important. We attribute the lack of a NO_2^* population inversion in experiments where $\theta > D_0(NO_2)$ to the tempering of this expected result by the lower surface. The $1^1A' \rightarrow 2^1A'$ transition associated with the intense 180nm absorption feature is not predicted to contribute to the reaction dynamics until single photon excitation energies exceed 45,000 cm^{-1}.

The PIF NO_2^* $P(E_{int})$ distribution derived from 241nm $HONO_2$ photodissociation (Figure 22 and Table VII) agrees qualitatively with the results inferred for the NO_2 fragment from the OH fragment LIF measurements recorded by Crim and coworkers[7]. For this dissociation θ = 24,995 cm^{-1}, very close to the $D_0(NO_2)$ limit, and there may be some dissociations which produce secondary NO_2 dissociation due to additional thermal

energy in the system. Crim et al.[7] found that only 5% of θ appears as rotational excitation of the OH radical and that there is negligible OH vibrational excitation. From the Doppler profiles of the OH fluorescence lines, it was determined that the center of mass translational energy release from this dissociation is 2600 cm^{-1} ($E_T(OH)$ = 1900 cm^{-1} and $E_T(NO_2)$ = 700 cm^{-1}). Their results imply that the NO_2 fragment retains 21,500 cm^{-1} or 85.5% of the energy available after HO-NO_2 bond rupture. Table VII shows that the PIF $P(E_{int})$ distribution has an average NO_2^* energy of 16,000 cm^{-1}, or 64% of θ, and a maximum at 12,195 cm^{-1}, the minimum energy in our observation window. While Figure 22 illustrates that there are significant contributions from the NO_2^* components with energies above 20,000 cm^{-1}, our results suggest that the 241nm $HONO_2$ photodissociation is still strongly influenced by dissociations leading to electronically excited NO_2 products with minimal rovibrational excitation, or highly rovibrationally excited $^2A_1$ NO_2 products which couple to the bright state manifold and fluoresce. The lower energy PIF $P(E_{int})$ distribution reflects a broader and slightly slower translational energy distribution than the one inferred by Crim et al. from their Doppler profile measurements. All of these results are consistent with a transition involving contributions from both the $1^1A''$ *and* $2^1A''$ surfaces. The increased translational energy release observed by Crim et al. for the energetically equivalent VMP experiment ($E_T(OH)$ + $E_T(NO_2)$ = 4690 cm^{-1}) would thus be explained by a preferential excitation to the $1^1A''$ surface in the vibrationally mediated excitation.

A comparison of the PIF NO_2^* $P(E_{int})$ derived from 280nm $HONO_2$

photodissociation (Figure 31, Table XVI) with the results of August et al.[8] is more straightforward since they transform their measured OH population and translational energy distribution into a NO_2^* distribution. The August NO_2^* $P(E_{int})$ is described by a Gaussian distribution with a mean of 12,590 cm^{-1} and a FWHM of 6570 cm^{-1} (the values reported here are those for OH<N″>). This result is determined from OH LIF measurements which showed that the average OH rotational excitation accounts for 5% (890 cm^{-1}) and center of mass translational energy release for 29% (4090 cm^{-1} in OH; 1510 cm^{-1} inferred in NO_2 from momentum conservation) of the 19,470 cm^{-1} available (This θ value incorporates thermal excitation of the $HONO_2$ parent). The NO_2 fragment retains the remaining 65% (12,590 cm^{-1}) of the available energy as internal excitation. August et al. also note that the OH translational energy distribution is very broad: $\langle E_T \rangle = 4090$ cm^{-1}, $\Delta E_T = 4980$ cm^{-1}. We note that the NO_2^* $P(E_{int})$ distribution defined by August is equivalent to our Gaussian weighting function if M = 19,470; A = 12,590; and B = 2790.

Figure 57 shows that the PIF NO_2^* $P(E_{int})$ agrees very well with the August NO_2 $P(E_{int})$ between 12,000 and 19,000 cm^{-1}. Both distributions have been calculated at energy intervals corresponding to the 2nm increment used in the PIF experiments and both are normalized to account only for the population components in the displayed energy region. The apparent divergence of the two distributions below 13,000 cm^{-1} is reconciled by noting that this is the portion of the observation window in which the IF method is most suspect and that this behavior may be incorrect. The excellent agreement

between these two $P(E_{int})$ suggests that there is minimal difference between the NO_2 $P(E_{int})$ and the NO_2^* $P(E_{int})$ at these rovibronic energies. This apparent observation of the indistinguishablility of NO_2 internally excited ensembles supports one of the most basic assumptions of the IF model.

3.4.B. $ClNO_2$

The $ClNO_2$ absorption spectrum, Figure 4, displays simple behavior over the 230 - 310nm range employed in the PIF experiments. The absorption cross section increases slowly from 1.25×10^{-19} cm^2 $molecule^{-1}$ at 310nm to 3.72×10^{-19} cm^2 $molecule^{-1}$ at 270nm; abruptly it climbs rapidly, reaching a value of 2.5×10^{-18} cm^2 $molecule^{-1}$ at 230nm[10-12]. The broad undulations on the rising edge of the intense absorption feature are spaced at 320 cm^{-1} - which roughly corresponds to the ν_5 mode of the electronic ground state - and probably correspond to an excited state vibrational progression in a coordinate orthogonal to the dissociation coordinate. The lack of resolved rotational structure in this progression suggests that the bound motion persists for no more than a few vibrational periods before dissipating into dissociative motions.

The $ClNO_2$ absorption spectrum clearly shows that there are at least two potential energy surfaces contributing to absorption in the 230 - 310nm region: a moderately strong transition to the lower energy surface which gives rise to the nearly continuous absorption for wavelengths longer than 270nm and has its maximum near 330nm, and a strongly

allowed transition which has its long wavelength onset near 270nm ($h\nu$ = 37,000 cm^{-1})and peaks near 220nm[10-12]. It is interesting to note that for both $ClNO_2$ and $HONO_2$ the onset of the intense absorption features occurs at wavelengths corresponding to the sum of the R-NO_2 and $D_0(NO_2)$ dissociation energies: 270nm ($\sim$37,000 cm^{-1}) for $ClNO_2$ and 240nm ($\sim$41,500 cm^{-1}) for $HONO_2$.

Oh[13] attempted to analyze previous $ClNO_2$ photodissociation results using an analogy to the molecular orbital structure and calculated vertical transitions of the isovalent $HONO_2$ molecule[21,22]. While this may be qualitatively correct, we note that the strong electronegativity of the Cl atom, as well as its additional core electrons and 882 cm^{-1} spin-orbit splitting, should alter the energies and behavior of the $ClNO_2$ potential energy surfaces relative to their $HONO_2$ analogs. In a worst-case scenario, the Cl atom spin-obit splitting doubles the number of potential surfaces. Additionally, $ClNO_2$ possesses C_{2v} symmetry[23] (or its CNPI equivalent) while the planar $HONO_2$ molecule belongs to the C_s point group[24], although its NO_2 chromophore retains local C_{2v} character. It is the reduction from C_{2v} to C_s symmetry in $HONO_2$ that forces the avoided crossing in the exit channel and causes the $1^1A''$ surface to correlate to $OH(^2\Pi)$ + $NO_2(^2A_1)$ rather than the $OH(^2\Pi)$ + $NO_2(^2B_2)$ products expected from the nature of the $n \rightarrow \pi^*$ electron promotion localized on the NO_2 chromophore. $ClNO_2$ will not be subject to such avoided crossings as long as its electronically excited potential energy surfaces retain the C_{2v} symmetry found in the electronic groundstate.

Based on the Bai and Segal's ab initio study of the $HONO_2$ potential surfaces[9] and keeping the above caveats in mind, we expect and observe[10-12] three electronic transitions in the $ClNO_2$ UV absorption spectrum. All three transitions correlate to the production of electronically excited NO_2 products and are the result of electron promotion in molecular orbitals localized on the NO_2 chromophore. The two low energy $n \rightarrow \pi^*$ transitions, corresponding to thee maxima at 330 and 220nm, should have transition dipole moments of a_2 and b_1 symmetry. The a_2 transition probably occurs at lower energies and is less intense since it would be a forbidden electric dipole transition in C_{2v} symmetry. The third transition corresponds to the $\pi \rightarrow \pi^*$ promotion which creates the very intense absorption feature centered near 190nm characteristic of R-NO_2 molecules. We expect this transition to have an a_1 transition dipole moment, although the $HONO_2$ *ab initio* calculations also show contributions from a transition dipole moment having b_2 symmetry. Thus, analogy with the $HONO_2$ potential energy surfaces suggests that $ClNO_2$ will exhibit a_2 and b_1 transitions in the 235-310nm range and that both excitations correlate to electronically excited NO_2 products.

The NO_2^* $P(E_{int})$ distributions derived from the $ClNO_2$ PIF experiments indicate that the NO_2^* ensembles created in these photodissociations are far more energetic than their $HONO_2$ counterparts. Figures 44-49 show that the $ClNO_2$ $P(E_{int})$ for photolysis wavelengths from 235 to 260nm are inverted, peaking at the maximum possible NO_2^* energy. The $P(E_{int})$ distributions also exhibit a smooth transformation in their contours as θ decreases from 30,000 cm^{-1} through $D_0(NO_2)$ to 20,000 cm^{-1} - see Figures 44-55 for

the complete trend. Tables XVII-XXVIII and Figure 58 show that the average energy of the $ClNO_2$ NO_2^* $P(E_{int})$ distributions scales linearly with θ. The NO_2 fragment constantly retains 70 - 75% of θ, and the $P(E_{int})$ maxima shift to progressively lower energies as θ decreases. This figure also shows the correlation between thee most probable NO_2^* energy and the average energy of the ensemble: the transition region between the two $P(E_{int})$ behaviors occurs for θ between 23,000 and 25,000 cm^{-1} (single photon excitation energies of 34,865 - 36,865 cm^{-1} or wavelengths of 287 - 271nm). The accelerated transformation between the $P(E_{int})$ distributions found for the 280 and 290nm photodissociations, Figures 52 and 53, roughly coincides with the intensity change in the $ClNO_2$ absorption spectrum and the expected change in the identity of the dominant potential energy surface reached by the transition. The concentration of NO_2^* components below 15,000 cm^{-1} for the 290 - 308nm $P(E_{int})$ distributions, Figures 53-55, seems to represent a continuation in the evolution of the $ClNO_2$ NO_2^* $P(E_{int})$ distributions with decreasing θ, although it may indicate that the dissociation now also produces a significant amount of highly rovibrationally excited $^2A_1$ NO_2 as well as NO_2^*.

Covinsky[16] has determined the $P(E_T)$ distributions for 248.5 and 308nm $ClNO_2$ photodissociation using time of flight detection. Oh[13] and Sisk[14] have previously discussed the comparison of the 248.5nm PIF NO_2^* $P(E_{int})$ and the TOF $P(E_T)$, and good qualitative agreement of the PIF $P(E_{int})$ with the appropriate portion of the TOF $P(E_T)$. However, these comparisons suffer from two drawbacks. Firstly, 248.5nm $ClNO_2$ photolysis has a θ value of 28,375 cm^{-1}, or 3245 cm^{-1} more energy than required for

subsequent dissociation of the NO_2 fragment. The possible contributions of the three body dissociation, whether concerted or sequential, to the NO_2^* ensemble means that the PIF method is incapable of analyzing the total NO_2^* population in this process. The PIF $P(E_{int})$ distribution should still be correct over its applicable energy range, however.

Furthermore, it appears that the distinction between the TOF and PIF measurements is more subtle than has been previously acknowledged and a direct comparison of the TOF $P(E_T)$ and the PIF $P(E_{int})$ is incorrect. The TOF $P(E_T)$ measures the contributions from the entire NO_2 product ensemble, while the PIF $P(E_{int})$ only reflects the population distribution of those NO_2 molecules which fluoresce. A direct comparison of the TOF and PIF NO_2^* distributions is only valid if the fluorescing fraction of the NO_2^* population is a constant function of the NO_2 internal energy. This seems unlikely given the marked geometric differences in the $NO_2(^2A_1)$ groundstate and its electronically excited states and the strong couplings which create a total admixture of states.

Comparisons between TOF and PIF NO_2^* $P(E_{int})$ for 308nm $ClNO_2$ photodissociation are not complicated by the possibility of secondary dissociation of the NO_2 fragment, as is the case for the 248.5nm photolysis, since θ = 20,600 cm^{-1}. However, Figure 59 shows that the PIF $P(E_{int})$ peaks at the lowest possible energy - 12,195 cm^{-1} - and probably indicates a population that has its maximum at even lower energies. We transformed the 308nm $ClNO_2$ TOF $P(E_T)$ into an NO_2 internal energy

distribution using $E_{int} = \theta - E_T$. Figure 59 shows that these results are far less encouraging than the comparison of the 280nm $HONO_2$ NO_2^* $P(E_{int})$ with the August NO_2 $P(E_{int})$. We attempted to correct the apparent discrepancy between the TOF and PIF distributions by adjusting the TOF NO_2 $P(E_{int})$ for the internal energy dependent fractional volume of phase space occupied by nominally $^2B_2$ NO_2 electronic configurations. This produced no better agreement between the two contours. We do not yet understand the proper manner in which to compare these two types of measurements, but we continue investigating possible solutions to this problem.

We offer a few ideas on the possible reasons for the failure of the PIF $P(E_{int})$ to reproduce the TOF $P(E_{int})$. As mentioned above, this failure is due primarily to the measurement process and the species being measured. The time of flight method has universal detection, that is it detects all products of the designated mass only as a function of their recoil velocity. These experiments detect products entering the detector region at a specific time regardless of internal energy content or electronic state. Practical calculations using the flight times and distances involved in the Covinsky experiments show that the TOF $P(E_{int})$ distribution is essentially determined by the first few picoseconds of the dissociation process. This contrasts with the PIF $P(E_{int})$ determinations which measure the $P(E_{int})$ distribution only for the fluorescing fraction of the NO_2^* ensemble. The detection of the NO_2^* fluorescence is done in real time, but this occurs on a tens of nanoseconds timescale. This results in a measurement of the asymptotic energy distribution of the dissociation in contrast to the TOF measurement.

The NO_2^* ensemble evolves during the time interval that separates the TOF and PIF interrogations. Presumably, the photodissociation creates NO_2^* molecules in non-stationary eigenstates and their time evolution changes the nature of the NO_2^* ensemble in a non-trivial manner. Even the conceptually simple task of extracting the fraction of the $P(E_T)$ distribution proportional to the phase space volume of the bright state suffers from uncertainties due to the complicated nature of the NO_2 electronic structure.

3.4.C. $HONO_2$ and $ClNO_2$ photodissociations with equivalent θ

Prior to this study, we hypothesized that the nature of a given PIF NO_2^* $P(E_{int})$ distribution depended on θ, where $\theta = h\nu - D_0(R\text{-}NO_2)$, and the R-$NO_2$ bond strength because the transitions excited in these photodissociations are invariably localized on the NO_2 chromophore. We believed that the R group influenced the energy partitioning in R-NO_2 photolysis based solely on its ability to acquire internal excitation from the highly energized NO_2 chromophore during the rapid R-N bond dissociation. It was thought that the relatively weak R-NO_2 bond energies would cause minimal redistribution of the excitation energy prior to bond rupture and that the energy partitioning would be determined by the efficiency of R in coupling to the NO_2 group and the reorganizational energy required to form the isolated R radical. We chose to compare $ClNO_2$ and $HONO_2$ because they are isovalent and the Cl and OH groups undergo minimal change between their R-NO_2 and unbound geometries, making the energy partitioning predominantly dependent on the mechanical properties of the R group. The comparisons are shown for

θ = 25,000 to 20,000 cm^{-1} in Figures 60 - 65.

However, as has been presented above, it appears that the R group exerts a subtler influence on the energy partitioning. The R group manifests its influence not through the presence or absence of internal degrees of freedom, but through the total symmetry constraints it forces on the molecule. Both the Cl atom and the OH diatom lie along the NO_2 C_2 axis, however, the spherically symmetric Cl atom leaves the local C_{2v} symmetry of the NO_2 chromophore intact while non-linear H-O-N configurations in $HONO_2$ reduce the local C_{2v} symmetry to C_s in the molecule. It is the total molecular symmetry and its effect on the excited potential energy surfaces which actually governs the NO_2^* $P(E_{int})$ in $ClNO_2$ and $HONO_2$ photodissociations between.

3.5 CONCLUSIONS

The variable wavelength photodissociation of $HONO_2$ and $ClNO_2$ has illustrated the impact of the R group on the energy partitioning into the NO_2 fragment. The effect is not based on the mechanical properties of the R group, such as the presence or absence of internal degrees of freedom to participate in the energy partitioning during dissociation, but on the manner in which the R group influences the total symmetry of the R-NO_2 molecule. The retention of the NO_2 chromophore's local C_{2v} symmetry in $ClNO_2$ produces excited electronic potential energy surfaces which correlate to electronically excited NO_2; this leads to inverted NO_2^* $P(E_{int})$ distributions and a smooth

transition of the $P(E_{int})$ distribution to lower energies as θ decreases. The reduced C_s symmetry of $HONO_2$ leads to an avoided surface crossing which forces $1^1A''$, the first electronically excited potential surface, to correlate with $NO_2(^2A_1)$ rather than $NO_2(^2B_2)$ products. The photodissociation wavelengths used in this study favor $HONO_2$ excitations dominated by transitions to the $1^1A''$ surface, with the NO_2^* production presumably generated by non-adiabatic interactions. The resulting NO_2^* $P(E_{int})$ distributions still show that the NO_2 fragment retains 65 - 70 % of θ, but the $P(E_{int})$ distributions are no longer inverted and are highly concentrated for $E_{int} < 15{,}000\ cm^{-1}$. The $HONO_2$ NO_2^* $P(E_{int})$ distributions exhibit increased contributions from NO_2^* components near θ when the photodissociation wavelength is shorter than 255nm due to dissociations which occur on the $2^1A''$ and correlate directly to NO_2^* products.

REFERENCES

[1] World Meteorological Organization, Global Ozone Research and Monitoring Project, Report No. 16 (1985); Report No. 20 (1990).

[2] R.A. Graham, Ph.D. Thesis, Department of Chemistry, University of California, Berkeley, (1974); H.S. Johnston and R.A. Graham, J. Phys. Chem. **77**, 62 (1973); H.S. Johnston and R.A. Graham, Can. J. Chem. **52**, 1415 (1974).

[3] H.S. Johnston, S-G. Chang, and G. Whitten, J. Phys. Chem. **78**, 1 (1974).

[4] G.S. Jolly, D.L. Singleton, D.J. McKenney, and G. Paraskevopoulos, J. Chem. Phys. **84**, 6662 (1986).

[5] D.D. Nelson, A. Schiffman, and D. J. Nesbitt, J. Chem. Phys., **90**, 5445 (1989).

[6] M. Suto and L.C. Lee, J. Chem. Phys. **81**, 1294 (1984).

[7] A. Sinha, R.L. Vander Wal, L.J. Butler, and F.F. Crim, J. Phys. Chem. **86**, 6171 (1987); M.D. Likar, A. Sinha, T.M. Ticich, R.L. Vander Wal, and F.F. Crim, Ber. Bunsenges. Phys. Chem. **92**, 289 (1988); M.D. Likar, J.E. Baggott, A. Sinha, T.M. Ticich, R.L. Vander Wal, and F.F. Crim, J. Chem. Soc., Far. Trans. 2 **84**, 1483 (1988); A. Sinha, R.L. Vander Wal, and F.F. Crim, J. Chem. Phys. **91**, 2929 (1989).

[8] J. August, M. Brouard, and J.P. Simons, J. Chem. Soc., Far. Trans. 2, **84**, 587 (1988); J. August, M. Brouard, M.P. Docker, A. Hodgon, C.J. Milne, and J.P. Simons, Ber. Bunsenges. Phys. Chem. **92**, 264 (1988).

[9] Y.Y. Bai and G.A. Segal, J. Chem. Phys., **92**, 7479 (1990).

[10] A.J. Illies and G.A. Takacs, J. Photochem. **6**, 35 (1972).

[11] H.H. Nelson and H.S. Johnston, J. Phys. Chem. **85**, 3891 (1981).

[12] P. Hunter and H.S. Johnston, manuscript in preparation.

[13] B.Y. Oh, Ph.D. Thesis, Department of Chemistry, University of California, Berkeley (1988).

[14] W.N. Sisk Ph.D. Thesis, Department of Chemistry, University of California, Berkeley (1990).

[15] H.S. Johnston, C.E. Miller, B.Y. Oh, K.O. Patten, Jr., and W.N. Sisk, manuscript in preparation (Methods series).

[16] M. Covinsky, Ph.D. Thesis, Department of Chemistry, University of California, Berkeley, (1991).

[17] K.O. Patten, Jr., Ph.D. Thesis, Department of Chemistry, University of California, Berkeley, (1991).

[18] J.C. Devos, Physica **XX**, 690 (1954).

[19] H.H. Nelson, Ph.D. Thesis, Department of Chemistry, University of California, Berkeley, (1981) p. 23; see also W.N. Sisk Ph. D. Thesis, p. 110 and CEM Notebook #6, p. 28.

[20] Hunter Notebook #2, p.146; CEM Notebook #6, p. 75.

[21] L.E. Harris, J. Chem. Phys. **58**, 5615 (1973).

[22] D.A. Kleier and M.A. Lipton, J. Mol. Struct. (Theochem) **109**, 39 (1981).

[23] L. Clayton, Q. Williams, and T.L. Weatherly, J. Chem. Phys. **30**, 1328 (1959). The structural parameters derived in this study are: $R_{N\text{-}O}$ = 1.21 Å, $R_{Cl\text{-}N}$ = 1.83 Å, and ∠ONO = 129.5°.

[24] L.R. Maxwell and V.M. Moseley, J. Chem. Phys. **8**, 738 (1940). The equilibrium structural parameters are: R_{OH} = 0.95 Å, $R_{HO\text{-}N}$ = 1.41 Å, R_{NO} = 1.22 Å, ∠HONO = 114.5°, and ∠ONO = 130°.

Table I. *Ab initio* equilibrium state geometries and energies for nitric acid from Bai and Segal J. Chem. Phys., **92**, 7479 (1990).

Calculated optimum geometries and minimum energies								
State	T_e (cm^{-1})	R_{OH}	R_{NO1}	R_{NO2} R_{NO3}	$\angle O_1NO_2$	$\angle O_2NO_3$	ϕ_1	$\phi_{2,3}$
1 $^1A'$	0.00	0.95	1.39	1.22	115.0	130.0	0.0	planar
1 $^1A''$	27,420	0.95	1.46	1.30	108.6	108.8	-90.0	30.9
2 $^1A''$	36,615	0.95	1.46	1.32	104.9	123.8	-90.0	30.9
2 $^1A'$	45,728	0.95	1.47	1.30	108.6	112.8	-90.0	30.9
Expt.	0.00	0.95	1.41	1.22	114.5	130	0.0	planar
Distances in Å. $\angle HO_1N$ = 103.3° for all states.								

R_{NO1}	$R_{NO2,3}$	$\angle O_1NO_2$	$\angle O_2NO_3$	ϕ_1	ϕ_2	Energy
			$1\ ^1A'$			
1.10	1.25	115.0	130.0	0.0	0.0	22,098
1.39	1.22	115.0	130.0	0.0	0.0	0.0
1.60	1.22	114.7	130.0	-20.0	3.6	2985
1.80	1.22	112.1	134.0	-45.0	6.7	8065
2.00	1.22	110.9	134.0	-90.0	9.7	13,065
2.30	1.21	110.2	134.0	-90.0	11.2	16,695
			$1\ ^1A''$			
1.10	1.32	108.6	108.8	-90.0	30.9	55,325
1.46	1.30	108.6	108.8	-90.0	30.9	27,420
1.60	1.30	108.6	108.8	-90.0	30.9	28,470
1.80	1.25	108.6	108.8	-90.0	30.9	29,920
2.00	1.22	106.5	130.0	-90.0	19.1	26,050
2.30	1.21	105.8	134.0	-90.0	16.9	22,580
			$2\ ^1A''$			
1.10	1.32	108.6	112.8	-90.0	28.5	65,890
1.46	1.32	104.9	123.8	-90.0	24.1	36,615
1.60	1.31	104.9	123.8	-90.0	24.1	36,695
1.80	1.26	107.6	112.8	-90.0	29.1	37,825
2.00	1.26	112.1	108.8	-90.0	28.7	35,730
2.30	1.26	112.1	108.8	-90.0	28.7	34,115

Geometries optimized as a function of R_{NO1}. Distances in Å. Angles in degrees. Energies in cm^{-1}. $\angle O_1NO_2 = \angle O_1NO_3$, R_{OH} =0.95 Å, $\angle HO_1N$ =103.3°, $\phi_2 = \phi_3$ for all states.

Table II. Calculated points on the three lowest $HONO_2$ potential energy surfaces.

Table III $HONO_2$ PIF Data Acquisition Parameters

File	λ_{ex} (nm)	#Shots/ point	Press (mT)	Sens. (mV/V)	Gate Delay (ns)	Gate Width (ns)	P*Time (us T)	PMT (V)
CM681	235	1200	90	20	30	100	0.009	-1100
CM688	238	1200	80	20	30	100	0.008	-1100
CM682	241	800	45	20	30	100	0.0045	-1100
CM683	245	1000	90	20	30	100	0.009	-1100
CM691	250	1000	110	10	30	500	0.055	-1150
CM692	255	1000	110	10	30	1000	0.11	-1150
CM698	260	1000	100	10	30	500	0.05	-1100
CM696	265	1000	150	10	30	500	0.075	-1200
CM693	270	1000	120	10	30	500	0.060	-1150
CM697	275	1200	150	10	30	500	0.075	-1200
CM695	280	1000	150	10	30	500	0.075	-1200

Table IV: $ClNO_2$ PIF Experimental Parameters

File	λ_{ex}	# Shots/ Point	Press (mT)	Sens. (mV/V)	Gate Delay (ns)	Gate Width (ns)	P*Time (us T)	PMT (V)
CM677	235	1000	10	50	30	100	0.001	-1000
CM689	240	1200	10	50	30	100	0.001	-1000
CM684	245	800	10	50	30	100	0.001	-1000
CM665	250	1000	10	20	30	100	0.001	-1000
CM664 /699	255	1000	10	20	30	100	0.001	-1000
CM663	260	1000	10	50	30	100	0.001	-1000
CM661	270	1000	10	20	30	100	0.001	-1000
CM658	275	1000	5	50	30	100	0.0005	-1000
CM660	280	1000	10	20	30	100	0.001	-1000
CM707	290	1000	20	20	30	250	0.005	-1050
CM600	300	1000	20	20	30	100	0.002	-1150
CM655	308	1200	25	50	30	100	0.0025	-1000

Table V 235nm $HONO_2$ PIF Analysis: Optimized Fitting Parameters. θ = 26,055 cm^{-1}. See also Figure 20.

Set	M	A	B	Sum Error ($x10^{-3}$)	E_{ave}	E_{rms}	E_{max}
Gaussian Weighting Function							
Full	25,130	12,361	12,750	1.4339	16,385	16,720	12,195
Biexponential Weighting Function							
Full	26,055	2309.6	172,500	2.1850	17,213	17,594	25,125
Gamma Kernel Weighting Function							
Full	26,055	54,750	0.26562	1.3412	16,411	16,749	12,195

*The "Set" label identifies edited and unedited data, as described in the text.
*The definitions of the Gaussian, biexponential, and gamma kernel weighting functions are given in Chapter 1, Equations (1) - (3).
*The sum error is a measure of the calculated - experimental fitting residual. This is the figure of merit to use when comparing different optimized weighting function results.
*The average, rms, and most probable energies of the NO_2^* $P(E_{int})$ distribution are given in these columns in the units of cm^{-1}.

Table VI 238nm $HONO_2$ PIF Analysis: Optimized Fitting Parameters. θ = 25,515 cm^{-1}. See also Figure 21.

Set	M	A	B	Sum Error ($x10^{-3}$)	E_{ave}	E_{rms}	E_{max}
Gaussian Weighting Function							
Full	25,130	15,267	7468.7	1.9096	16,282	16,589	13,513
Biexponential Weighting Function							
Full	25,515	2822.3	136,500	1.8398	17,233	17,615	25,125
Gamma Kernel Weighting Function							
Full	25,515	14,031	0.5500	1.5405	16,302	16,619	12,195

Table VII 241nm $HONO_2$ PIF Analysis: Optimized Fitting Parameters. θ = 24,995 cm^{-1}. See also Figure 22.

Set	M	A	B	Sum Error ($x10^{-3}$)	E_{ave}	E_{rms}	E_{max}
Gaussian Weighting Function							
Full	25,130	15,689	5562.5	1.4068	16,114	16,388	14,759
Θ	24,995	15,874	5468.7	1.5183	16,003	16,267	14,409
Biexponential Weighting Function							
Full	24,995	3823.2	89,500	1.5071	17,244	17,261	25,000
Gamma Kernel Weighting Function							
Full	24,995	12,593	0.7375	1.2942	16,098	16,387	12,195
Θ	24,995	11,266	0.8125	1.4477	16,138	16,426	12,195

Table VIII 245nm $HONO_2$ PIF Analysis: Optimized Fitting Parameters. θ = 24,315 cm^{-1}. See also Figure 23.

Set	M	A	B	Sum Error ($x10^{-3}$)	E_{ave}	E_{rms}	E_{max}
Gaussian Weighting Function							
Full	25,130	16,350	4632.8	1.9054	16,057	16,308	15,337
Θ	25,130	16,631	4242.2	1.3402	16,122	16,365	15,822
Biexponential Weighting Function							
Full	24,315	2783.2	65,500	2.8240	17,054	17,397	24,271
θ	24,455	77,000	8637.5	1.7235	15,929	16,180	12,195
Gamma Kernel Weighting Function							
Full	25,115	9484.4	1.2187	2.3574	16,158	16,435	12,886
Θ	25,130	8510.7	1.5562	1.5761	16,231	16,501	15,384

Table IX 248.5nm $HONO_2$ PIF Analysis: Optimized Fitting Parameters. θ = 23,740 cm^{-1}. See also Figure 24.

Set	M	A	B	Sum Error ($x10^{-3}$)	E_{ave}	E_{rms}	E_{max}
Gaussian Weighting Function							
θ	23,740	17,829	3867.2	1.0982	16,601	16,832	17,182
θ+	23,740	17,826	3929.7	1.1537	16,591	16,823	17,182
Biexponential Weighting Function							
θ	23,559	63,000	4650	1.3695	16,415	16,658	18,050
Gamma Kernel Weighting Function							
θ	25,130	6580.8	2.6625	1.0295	16,836	17,092	18,518
θ+	25,130	6584.5	2.5875	1.1499	16,826	17,083	18,450

Table X 250nm $HONO_2$ PIF Analysis: Optimized Fitting Parameters. θ = 23,500 cm^{-1}. See also Figure 25.

Set	M	A	B	Sum Error ($x10^{-3}$)	E_{ave}	E_{rms}	E_{max}
Gaussian Weighting Function							
Full	25,130	14,734	4648.4	1.4726	15,499	15,717	13,623
Θ	24,000	14,282	5140.6	1.2686	15,449	15,664	12,886
Θ+	24,500	14,456	4906.2	1.3237	15,461	15,677	13,192
Biexponential Weighting Function							
Θ	24,363	41,563	27,500	1.3958	15,356	15,574	12,195
Gamma Kernel Weighting Function							
Full	25,100	17,125	1.3750	1.7658	15,582	15,821	12,195
Θ	27,000	14,077	3.0875	1.3069	15,625	15,859	12,195
Θ+	28,000	15,063	3.7875	1.3515	15,621	15,857	12,195

Table XI 255nm $HONO_2$ PIF Analysis: Optimized Fitting Parameters. θ = 22,715 cm^{-1}. See also Figure 26.

Set	M	A	B	Sum Error ($x10^{-3}$)	E_{ave}	E_{rms}	E_{max}
Gaussian Weighting Function							
Full	23,500	9016.1	6812.5	0.7871	14,945	15,135	12,195
θ	23,000	3842.8	8875	0.6351	14,905	15,093	12,195
θ+	23,000	1743.2	9562.5	0.5845	14,899	15,088	12,195
Biexponential Weighting Function							
θ	23,909	4.262E6	8.32E6	2.0206	14,975	15,160	12,195
Gamma Kernel Weighting Function							
Full	25,115	210,750	1.3547	1.0349	15,095	15,300	12,195
θ	26,000	38,984	1.9375	1.3117	15,087	15,291	12,195
θ+	26,000	47,500	1.8500	1.1578	15,080	15,284	12,195

Table XII 260nm $HONO_2$ PIF Analysis: Optimized Fitting Parameters. θ = 21,960 cm^{-1} See also Figure 27.

Set	M	A	B	Sum Error ($x10^{-3}$)	E_{ave}	E_{rms}	E_{max}
Gaussian Weighting Function							
Full	23,000	108.40	9156.2	1.1452	14,716	14,890	12,195
Θ	23,000	4868.2	7687.5	0.9670	14,720	14,890	12,195
Θ+	23,000	2641.6	8375	0.8177	14,710	14,882	12,195
Biexponential Weighting Function							
Θ	23,163	4.5525E6	8.42E6	3.3371	14,843	15,010	12,195
Gamma Kernel Weighting Function							
Full	25,060	225,250	1.5922	1.9569	14,919	15,106	12,195
Θ	26,000	55,938	2.1375	1.3438	14,893	15,079	12,195
Θ+	26,000	98,125	1.9875	1.1186	14,883	15,069	12,195

Table XIII 265nm $HONO_2$ PIF Analysis: Optimized Fitting Parameters. θ = 21,235 cm^{-1}. See also Figure 28.

Set	M	A	B	Sum Error ($x10^{-3}$)	E_{ave}	E_{rms}	E_{max}
Gaussian Weighting Function							
Full	22,000	7318.7	6781.2	1.0271	14,660	14,813	12,195
Θ	22,000	29.297	8746.1	1.4973	14,564	14,715	12,195
Θ+	22,000	14.648	8773.4	1.4522	14,569	14,720	12,195
Biexponential Weighting Function							
Θ	22,375	1.664E7	3.33E7	3.9246	14,698	14,846	12,195
Gamma Kernel Weighting Function							
Full	24,000	65,250	1.6187	1.2140	14,820	14,988	12,195
Θ	24,500	485,000	1.7187	2.0513	14,733	14,898	12,195
Θ+	24,500	605,000	1.7047	1.9273	14,738	14,904	12,195

Table XIV 270nm $HONO_2$ PIF Analysis: Optimized Fitting Parameters. θ = 20,537 cm^{-1}. See also Figure 29.

Set	M	A	B	Sum Error ($x10^{-3}$)	E_{ave}	E_{rms}	E_{max}
Gaussian Weighting Function							
Full	22,000	11,331	4671.9	1.6885	14,575	14,712	12,195
Θ	21,000	8168.9	6250	1.2081	14,541	14,676	12,195
Θ+	21,000	6313.5	6937.5	1.2370	14,530	14,666	12,195
Biexponential Weighting Function							
Θ	21,748	3.573E6	6.44E6	1.5513	14,581	14,714	12,195
Gamma Kernel Weighting Function							
Full	24,500	22,688	2.7626	1.5125	14,696	14,847	12,195
Θ	22,500	49,531	1.4062	1.3182	14,704	14,851	12,195
Θ+	22,500	162,500	1.2937	1.2243	14,692	14,840	12,195

Table XV 275nm $HONO_2$ PIF Analysis: Optimized Fitting Parameters. θ = 19,865 cm^{-1}
See also Figure 30.

Set	M	A	B	Sum Error ($x10^{-3}$)	E_{ave}	E_{rms}	E_{max}
Gaussian Weighting Function							
Full	20,500	32.813	7640.6	3.1606	14,232	14,345	12,195
θ	20,500	29.297	7418	4.1355	14,181	14,290	12,195
θ+	21,000	29.297	7257.8	3.9291	14,138	14,245	12,195
Biexponential Weighting Function							
θ	20,522	1.762E6	3.39E6	6.5843	14,339	14,446	12,195
Gamma Kernel Weighting Function							
Full	23,000	100,000	1.8094	3.7564	14,504	14,639	12,195
θ	23,000	435,000	2.0453	4.6821	14,335	14,455	12,195
θ+	24,000	425,000	2.4344	4.3815	14,309	14,431	12,195

Table XVI 280nm $HONO_2$ PIF Analysis: Optimized Fitting Parameters. θ = 19,215 cm^{-1}. See also FIgure 31.

Set	M	A	B	Sum Error ($x10^{-3}$)	E_{ave}	E_{rms}	E_{max}
Gaussian Weighting Function							
Full	20,500	4289.8	5875	2.4453	14,061	14,160	12,195
θ	19,500	19.531	7367.2	2.1088	14,095	14,191	12,195
θ+	20,000	712.89	6875	1.9181	14,062	14,159	12,195
Biexponential Weighting Function							
θ	19,900	8.322E6	1.66E7	4.2284	14,210	14,303	12,195
Gamma Kernel Weighting Function							
Full	23,000	70,250	2.5125	2.2017	14,231	14,341	12,195
θ	21,500	445,000	1.7375	2.5112	14,240	14,347	12,195
θ+	22,000	445,000	1.9406	2.2645	14,227	14,334	12,195

Table XVII 235nm $ClNO_2$ PIF Analysis: Optimized Fitting Parameters. θ = 30,690 cm^{-1}. See also FIgure 44.

Set	M	A	B	Sum Error ($x10^{-3}$)	E_{ave}	E_{rms}	E_{max}
Gaussian Weighting Function							
Full	25,130	555,630	55,500	8.2111	19,226	19,597	25,125
Biexponential Weighting Function							
Full	30,865	468.75	5296.9	4.7120	19,814	20159	25,125
Gamma Kernel Weighting Function							
Full	26,000	1.9398	3.66E-4	4.7134	19,434	19,798	25,125

Table XVIII 240nm $ClNO_2$ PIF Analysis: Optimized Fitting Parameters. θ = 29,800 cm^{-1}. See also Figure 45.

Set	M	A	B	Sum Error ($x10^{-3}$)	E_{ave}	E_{rms}	E_{max}
Gaussian Weighting Function							
Full	25,130	394,380	89,500	8.5873	18,232	18,626	25,125
Biexponential Weighting Function							
Full	29,800	468.75	8671.9	5.7421	18,764	19,149	25,125
Gamma Kernel Weighting Function							
Full	26,000	2.1172	2.44E-4	5.2510	18,365	18,758	25,125

Table XIX 245nm $ClNO_2$ PIF Analysis: Optimized Fitting Parameters. θ = 28,950 cm^{-1}. See also Figure 46.

Set	M	A	B	Sum Error ($x10^{-3}$)	E_{ave}	E_{rms}	E_{max}
Gaussian Weighting Function							
Full	25,130	545,630	61,500	9.0895	18,716	19,103	25,125
Biexponential Weighting Function							
Full	28,950	312.50	6617.2	5.9760	19,283	19,652	25,125
Gamma Kernel Weighting Function							
Full	28,950	6.4621	9.76E-4	5.9474	18,888	19,271	25,125

Table XX 250nm $ClNO_2$ PIF Analysis: Optimized Fitting Parameters. θ = 28,135 cm^{-1}. See also Figure 47.

Set	M	A	B	Sum Error ($x10^{-3}$)	E_{ave}	E_{rms}	E_{max}
Gaussian Weighting Function							
Full	25,130	278,750	50,750	9.4304	18,518	18,551	25,125
Biexponential Weighting Function							
Full	28,135	234.37	9015.6	6.5549	19,117	19,492	25,125
Gamma Kernel Weighting Function							
Full	28,135	7.4921	7.81E-4	7.0339	18,203	18,598	25,125

Table XXI 255nm $ClNO_2$ PIF Analysis: Optimized Fitting Parameters. θ = 27,350 cm^{-1}. See also Figure 48.

Set	M	A	B	Sum Error ($x10^{-3}$)	E_{ave}	E_{rms}	E_{max}
Gaussian Weighting Function							
Full	25,130	356,250	66,500	9.9714	17,804	18,198	25,125
Biexponential Weighting Function							
Full	27,350	234.37	11,875	7.3581	18,987	19,366	25,125
Gamma Kernel Weighting Function							
Full	27,350	5.6692	7.81E-4	5.2235	18,682	19,070	25,125

Table XXII 260nm $ClNO_2$ PIF Analysis: Optimized Fitting Parameters. θ = 26,595 cm^{-1}. See also Figure 49.

Set	M	A	B	Sum Error ($x10^{-3}$)	E_{ave}	E_{rms}	E_{max}
Gaussian Weighting Function							
Full	25,130	35,699	11,250	3.4269	18,647	19,019	25,125
Biexponential Weighting Function							
Full	26,595	3598.6	4687.5	1.5514	19,043	19,390	23,696
Gamma Kernel Weighting Function							
Full	26,595	2953.1	0.8375	1.5935	19,071	19,414	23,809

Table XXIII 270nm $ClNO_2$ PIF Analysis: Optimized Fitting Parameters. $\theta = 25,170\ cm^{-1}$. See also Figure 50.

Set	M	A	B	Sum Error ($x10^{-3}$)	E_{ave}	E_{rms}	E_{max}
Gaussian Weighting Function							
Full	25,130	100,130	49,750	4.0677	17,207	17,590	25,125
Θ	25,130	156,250	61,500	2.6363	17,064	17,444	12,195
Biexponential Weighting Function							
Full	25,170	14.648	25,688	2.5092	17,285	17,670	25,125
Gamma Kernel Weighting Function							
Full	25,170	5.2338	1.95E-4	2.4777	17,262	17,647	25,125
Θ	25,170	5.3864	1.95E-4	2.6082	17,249	17,633	25,125

Table XXIV 275nm $ClNO_2$ PIF Analysis: Optimized Fitting Parameters. θ = 24,500 cm^{-1}. See also Figure 51.

Set	M	A	B	Sum Error ($x10^{-3}$)	E_{ave}	E_{rms}	E_{max}
Gaussian Weighting Function							
Full	24,500	21,267	4250	2.0747	18,414	18,679	20,576
Θ	24,500	21,272	4359.4	2.2520	18,337	18,607	20,576
Biexponential Weighting Function							
Full	24,500	2661.1	4156.2	1.4317	18,606	18,899	22,222
θ	23,530	71.094	5600	1.0396	18,061	18,362	23,148
Gamma Kernel Weighting Function							
Full	24,500	2551.8	0.85625	1.4703	18,640	18,927	22,123
Θ	24,500	2547.9	0.8125	1.5368	18,551	18,843	22,123

Table XXV 280nm $ClNO_2$ PIF Analysis: Optimized Fitting Parameters. θ = 23,850 cm^{-1}. See also Figure 52.

Set	M	A	B	Sum Error ($x10^{-3}$)	E_{ave}	E_{rms}	E_{max}
Gaussian Weighting Function							
Full	23,850	25,674	10,625	1.311	17,044	17,358	21,551
Θ	23,850	22,651	7875	1.1952	17,147	17,452	20,235
Θ+	23,850	32,071	8250	1.0932	17,137	17,443	20,491
Biexponential Weighting Function							
Full	23,850	218.51	13,313	1.0701	17,233	17,558	23,148
θ	23,525	29.063	11,700	0.7441	17,063	17,374	23,364
Gamma Kernel Weighting Function							
Full	23,850	1217.8	0.11562	1.1492	17,217	17,537	22,624
Θ	23,850	1694.3	0.20937	0.9244	17,329	17,643	22,123
Θ+	23,850	1603.5	0.19062	0.8638	17,318	17,634	22,222

Table XXVI 290nm $ClNO_2$ PIF Analysis: Optimized Fitting Parameters. θ = 22,620 cm^{-1}. See also Figure 53.

Set	M	A	B	Sum Error ($x10^{-3}$)	E_{ave}	E_{rms}	E_{max}
Gaussian Weighting Function							
Full	23,500	13,843	9187.5	0.7292	15,860	16,120	12,195
Θ	22,620	11,875	56,500	3.0533	15,942	16,193	12,195
Θ+	22,620	14,375	5625	3.2430	15,448	15,651	12,658
Biexponential Weighting Function							
Θ	24,463	2631.6	1.04E6	1.0855	15,856	16,114	12,195
Gamma Kernel Weighting Function							
Full	24,000	16,281	0.4031	0.8164	16,028	16,303	12,195
Θ	23,500	285,000	0.20117	0.7529	16,006	16,277	12,195
Θ+	23,500	245,000	0.20469	0.7789	16,002	16,272	12,195

Table XXVII 300nm $ClNO_2$ PIF Analysis: Optimized Fitting Parameters. θ = 21,470 cm^{-1}. See also Figure 54.

Set	M	A	B	Sum Error ($x10^{-3}$)	E_{ave}	E_{rms}	E_{max}
Gaussian Weighting Function							
Full	23,000	5687.3	9187.5	1.1592	15,097	15,300	12,195
θ	22,500	29.297	11,734	1.5682	15,090	15,288	12,195
θ+	22,500	19.531	11,961	1.2693	15,117	15,317	12,195
Biexponential Weighting Function							
θ	24,225	465,380	86,000	2.0181	15,104	15,302	12,195
Gamma Kernel Weighting Function							
Full	24,500	146,750	1.0203	1.6248	15,273	15,491	12,195
θ	24,000	375,000	0.88281	1.9638	15,279	15,494	12,195
θ+	24,000	255,000	0.86562	1.6310	15,303	15,520	12,195

Table XXVIII 308nm $ClNO_2$ PIF Analysis: Optimized Fitting Parameters. θ = 20,600 cm^{-1}. See also Figure 55.

Set	M	A	B	Sum Error ($x10^{-3}$)	E_{ave}	E_{rms}	E_{max}
Gaussian Weighting Function							
Full	23,000	14,529	4656.2	1.7723	15,343	15,535	13,404
Θ	21,500	253.91	14,563	1.1968	15,197	15,385	12,195
Θ+	22,000	11,875	7187.5	1.1049	15,223	15,413	12,195
Biexponential Weighting Function							
Θ	22,756	4134	427,900	1.5453	15,247	15,434	12,195
Gamma Kernel Weighting Function							
Full	25,130	12,031	2.4875	1.6341	15,490	15,701	12,195
Θ	22,000	295,000	0.37891	1.3637	15,388	15,586	12,195
Θ+	22,500	40,000	0.5500	1.1308	15,384	15,588	12,195

Table XXIX A comparison of the available energies for several sets of $ClNO_2$ and $HONO_2$ PIF experiments.

$ClNO_2$ λ_{ex} (nm)	$ClNO_2$ E_{avl} = $h\nu$ - $D_0(Cl\text{-}NO_2)$ (cm^{-1})	$HONO_2$ λ_{ex} (nm)	$HONO_2$ E_{avl} = $h\nu$-$D_0(HO\text{-}NO_2)$ (cm^{-1})	ΔE = $E_{avl}(ClNO_2)$ - $E_{avl}(HONO_2)$
270	25,170	241	24,995	175
275	24,500	245	24,315	185
280	23,850	250	23,500	350
290	22,615	255	22,716	-100
300	21,465	265	21,235	230
308	20,600	270	20,535	65

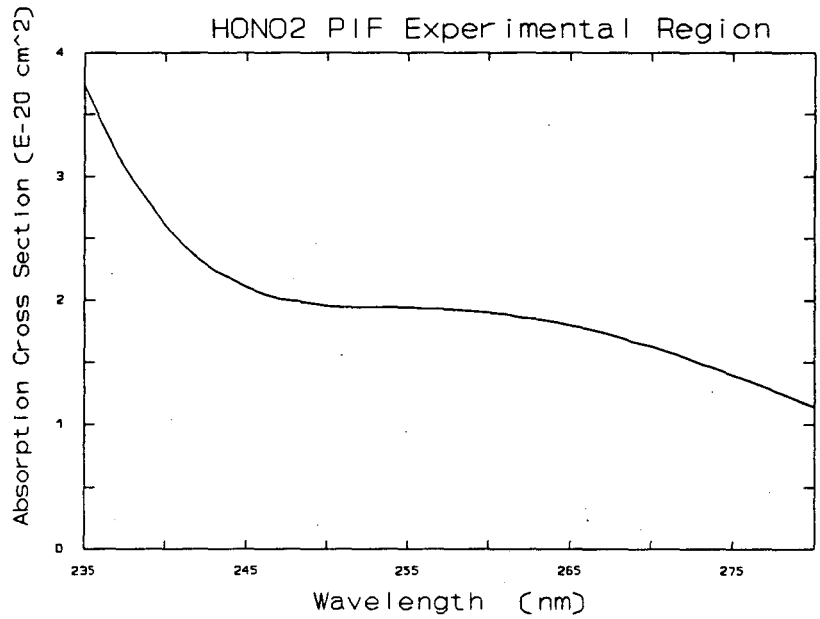

Figure 1 $HONO_2$ absorption cross sections between 230 and 280nm [Ref. 2].

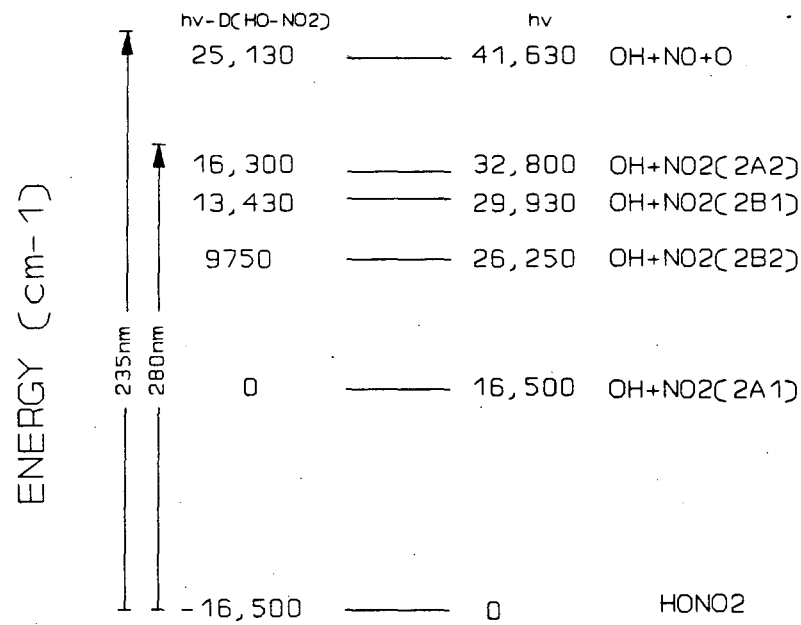

Figure 2. $HONO_2$ Photodissociation Thermodynamic Thresholds.

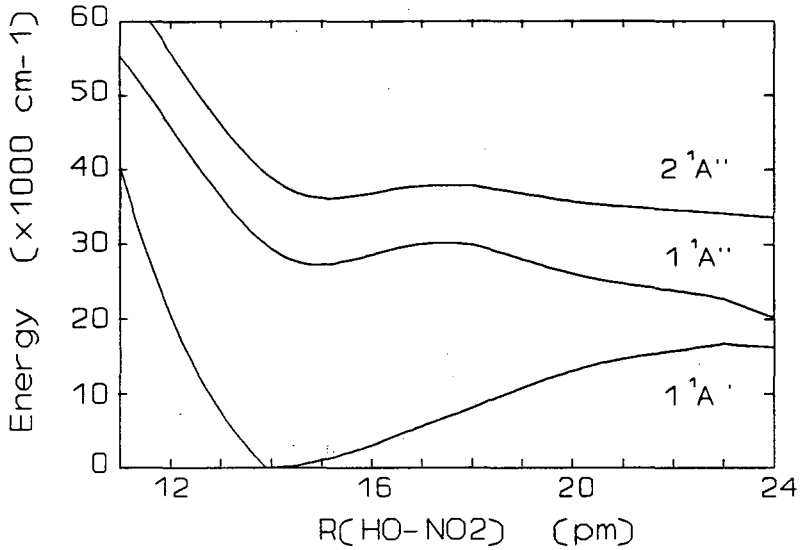

Figure 3 The *ab initio* $HONO_2$ potential energy surfaces [Ref. 7]: $1^1A'$ and $1^1A''$ correlate to $NO_2(^2A_1)$; $2^1A''$ correlates to $NO_2(^2B_2)$.

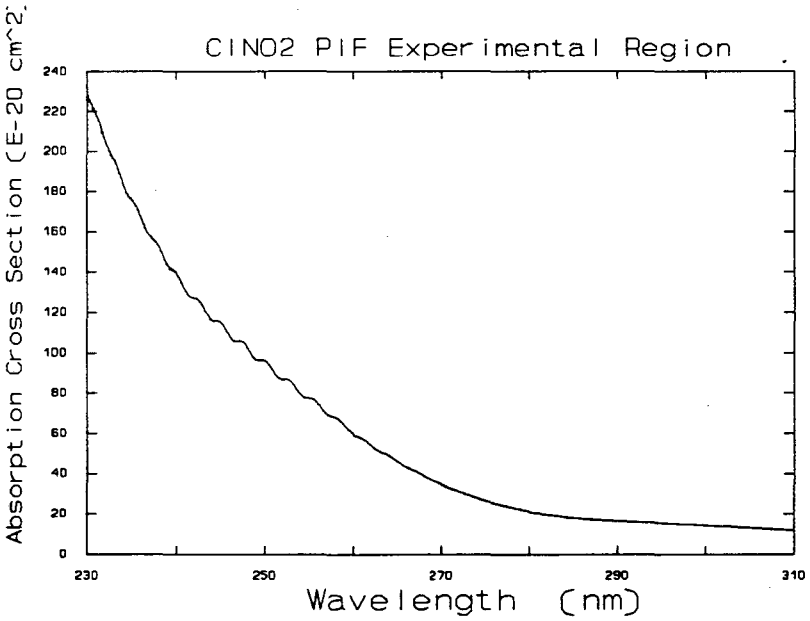

Figure 4 $ClNO_2$ absorption cross sections between 230 and 310nm [Ref 12].

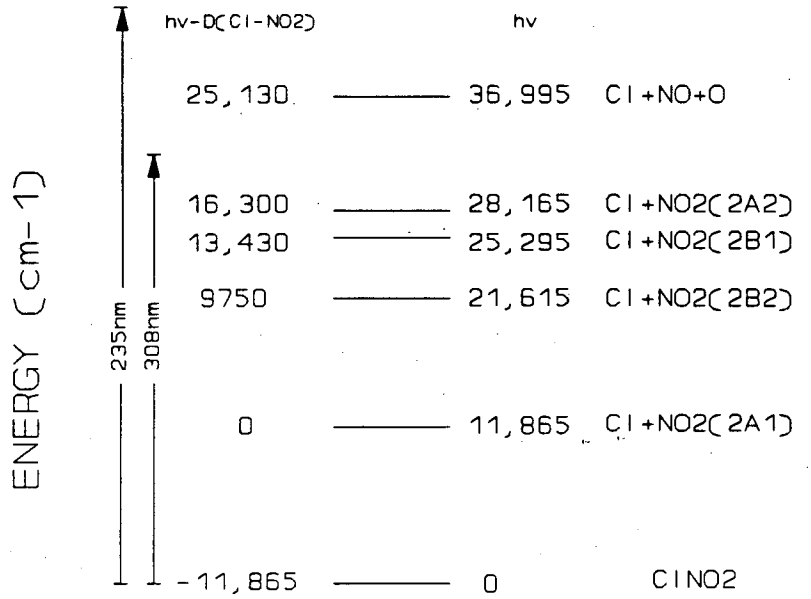

Figure 5. $ClNO_2$ Photodissociation Thermodynamic Thresholds.

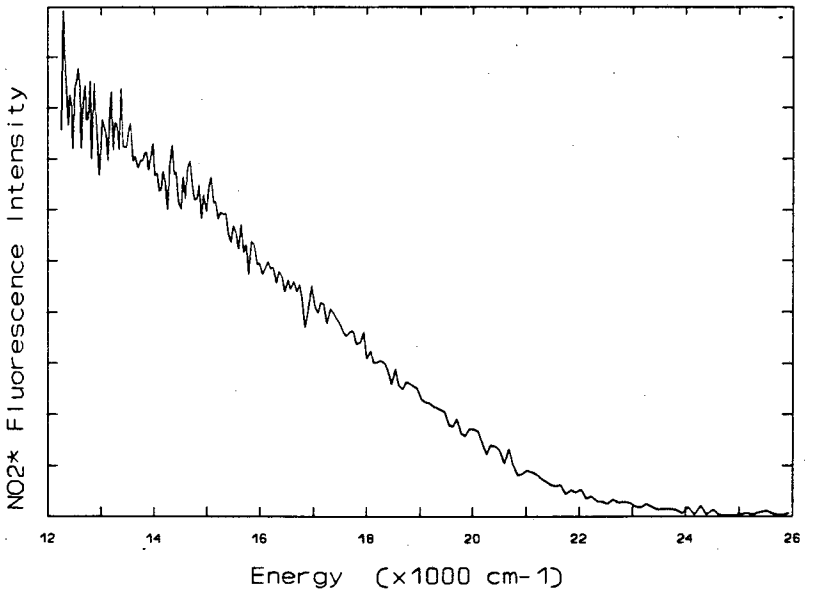

Figure 6. NO_2^* PIF signal from 235nm $HONO_2$ photodissociation.

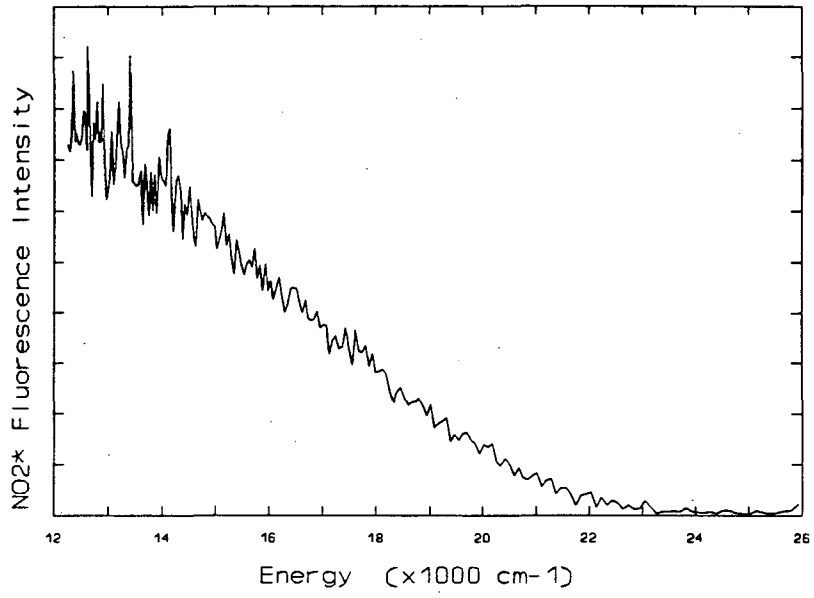

Figure 7. NO_2^* PIF signal from 238nm $HONO_2$ photodissociation.

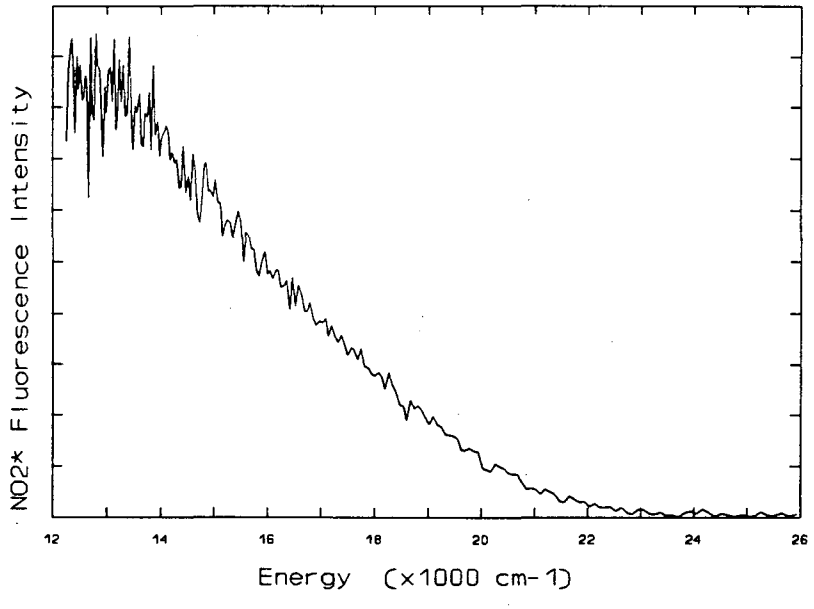

Figure 8. NO_2^* PIF signal from 241nm $HONO_2$ photodissociation.

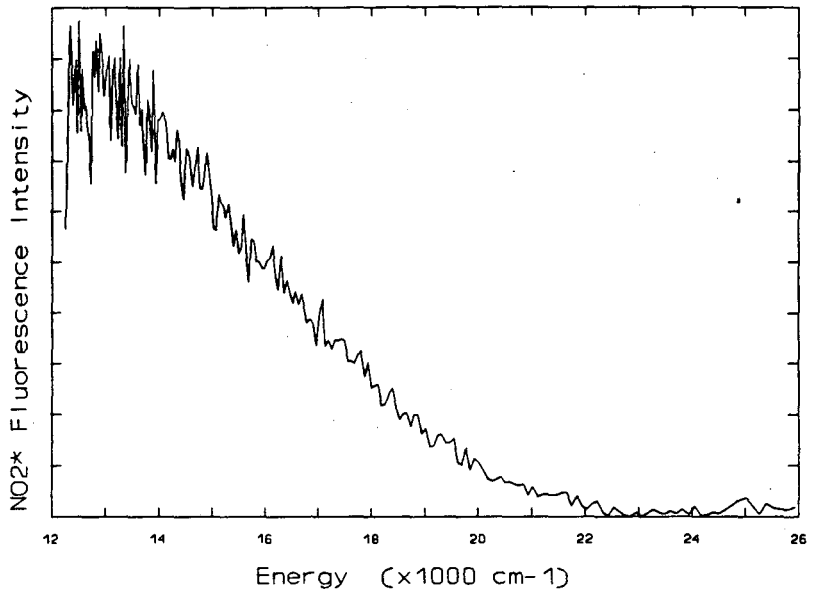

Figure 9. NO_2^* PIF signal from 245nm $HONO_2$ photodissociation.

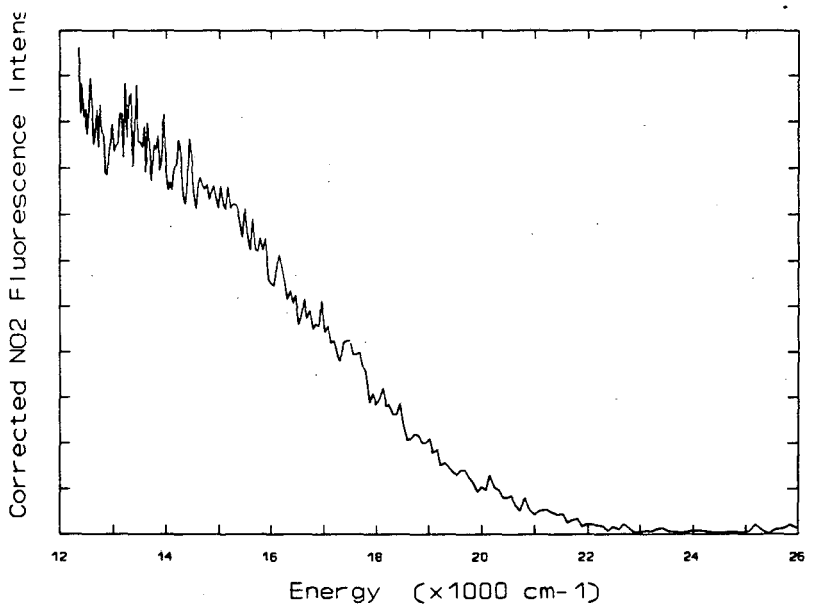

Figure 10 NO_2^* PIF signal from 248.5nm $HONO_2$ photodissociation.

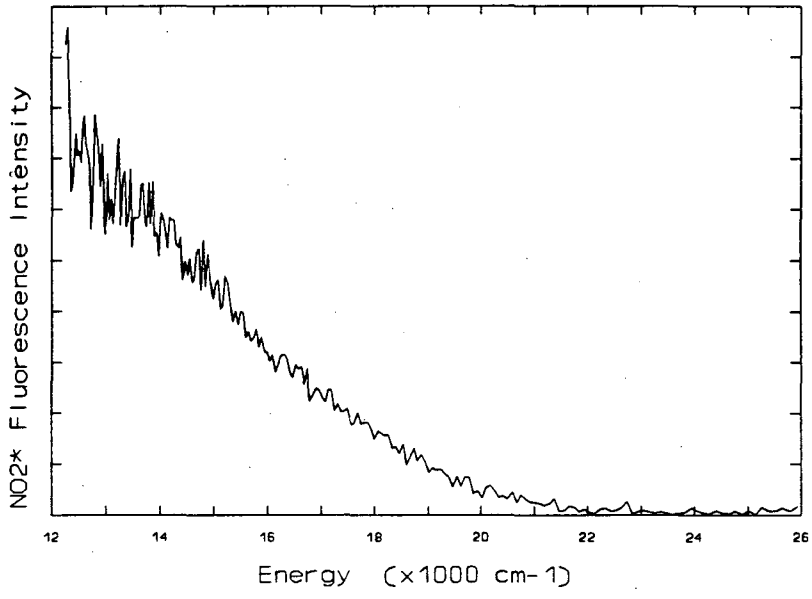

Figure 11. NO_2^* PIF signal from 250nm $HONO_2$ photodissociation.

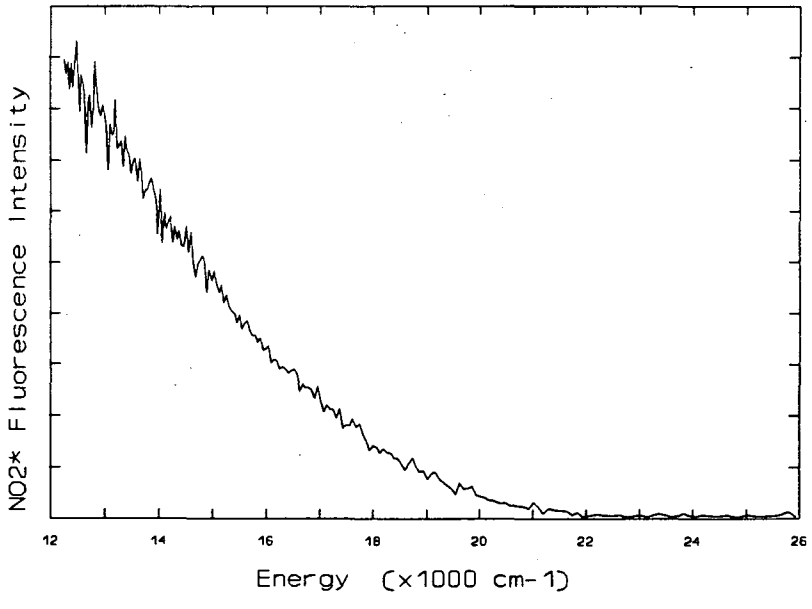

Figure 12. NO_2^* PIF signal from 255nm $HONO_2$ photodissociation.

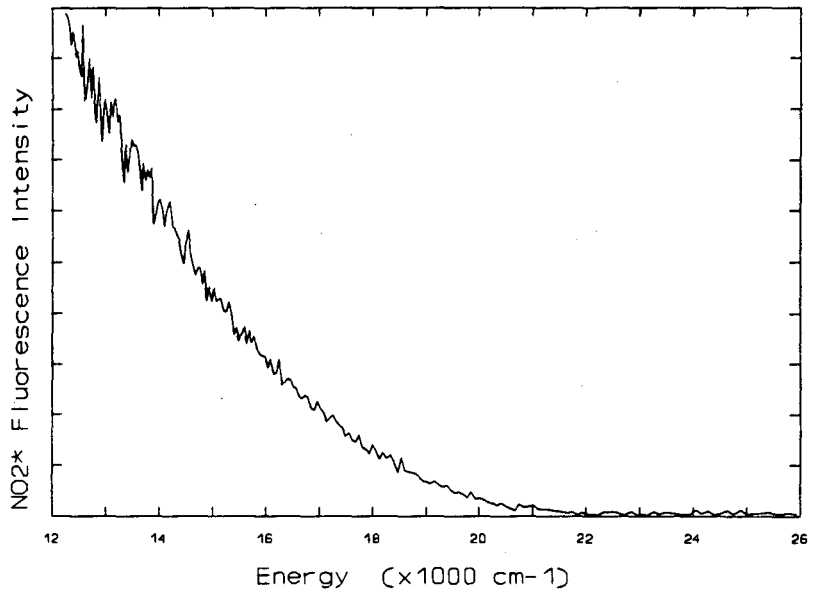

Figure 13. NO_2^* PIF signal from 260nm $HONO_2$ photodissociation.

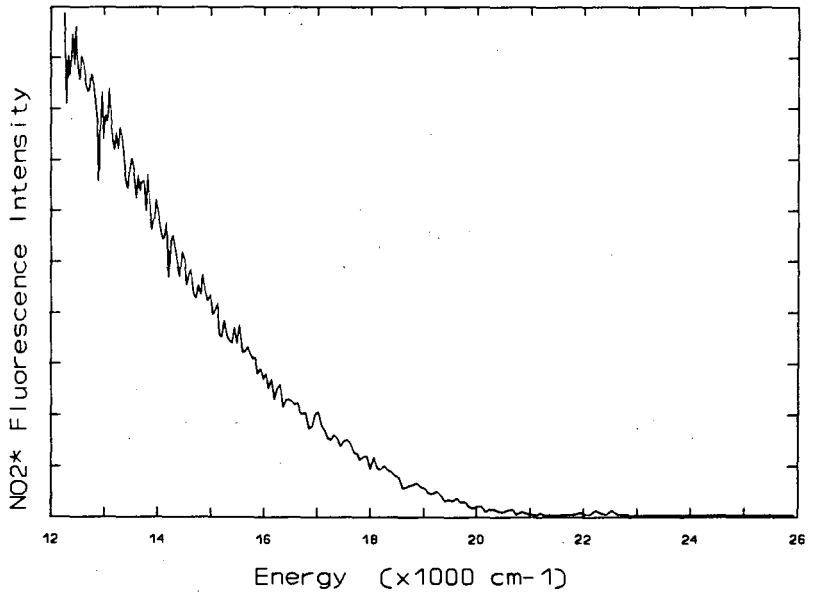

Figure 14. NO_2^* PIF signal from 265nm $HONO_2$ photodissociation.

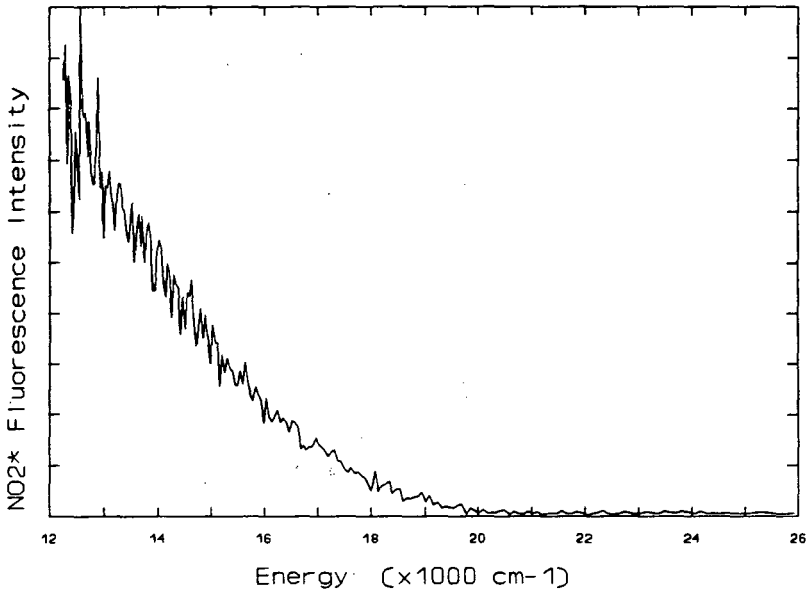

Figure 15. NO_2^* PIF signal from 270nm $HONO_2$ photodissociation.

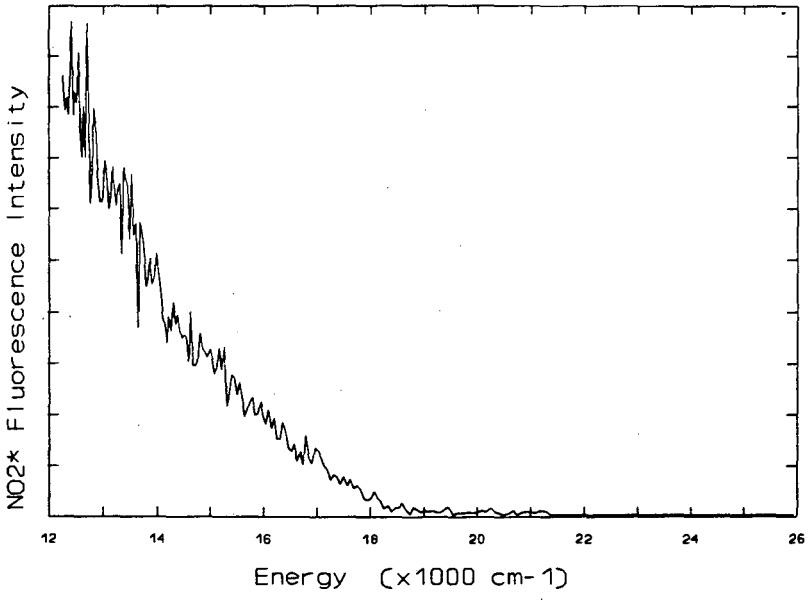

Figure 16. NO_2^* PIF signal from 275nm $HONO_2$ photodissociation.

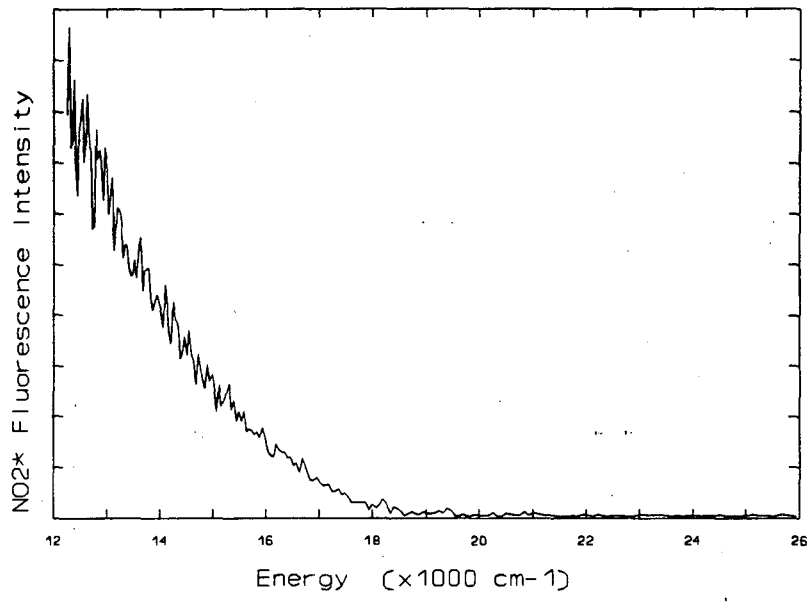

Figure 17. NO_2^* PIF signal from 280nm $HONO_2$ photodissociation.

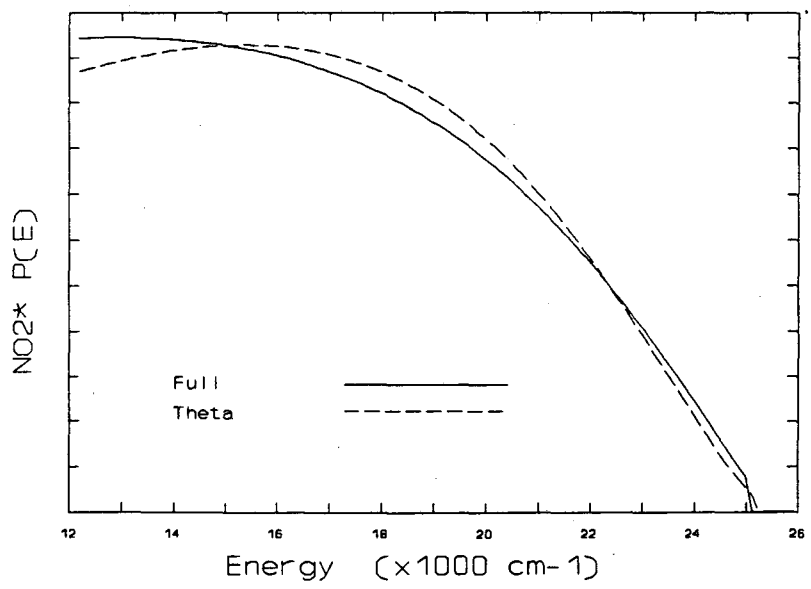

Figure 18. A comparison of the NO_2^* $P(E_{int})$ derived from the gamma kernel weighting function for the Full and θ data for 245nm $HONO_2$ photolysis.

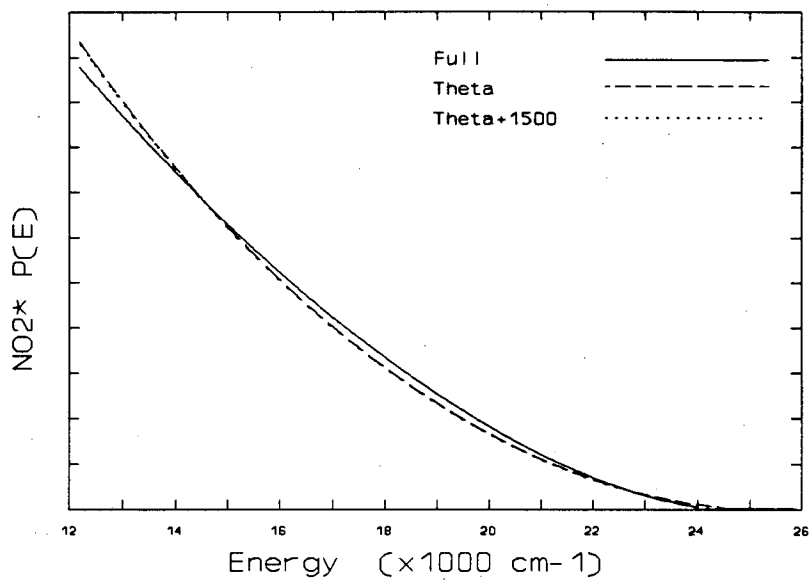

Figure 19. A comparison of the NO_2^* $P(E_{int})$ derived from the gamma kernel weighting function for the Full, θ, and $\theta+$ data for 265nm $HONO_2$ photolysis.

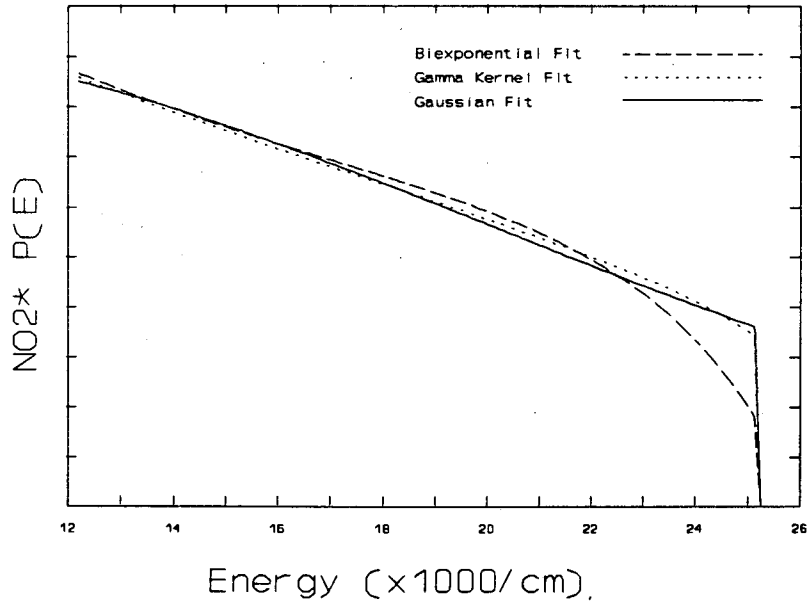

Figure 20. 235nm $HONO_2$ NO_2^* $P(E_{int})$: θ = 26,055 cm^{-1}. See also Figure 6 and Table V.

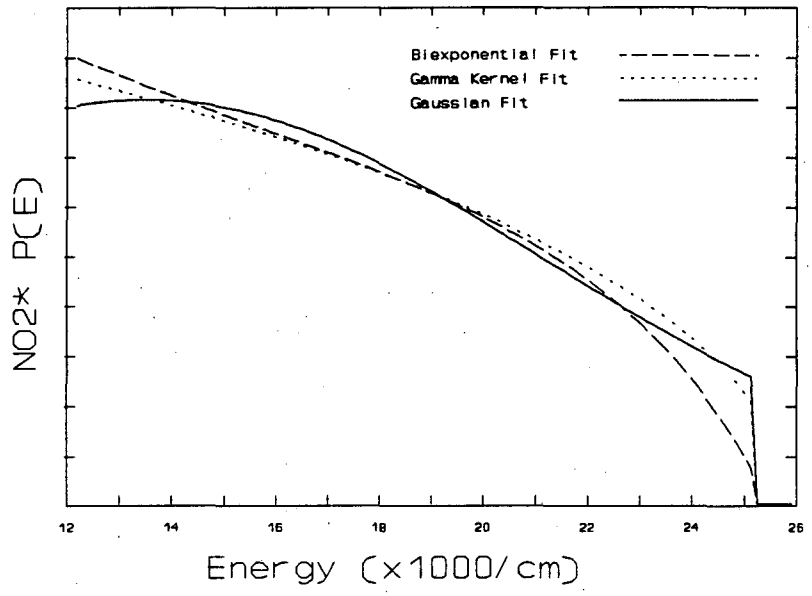

Figure 21. 238nm $HONO_2$ NO_2^* $P(E_{int})$: θ = 25,515 cm^{-1}. See also Figure 7 and Table VI.

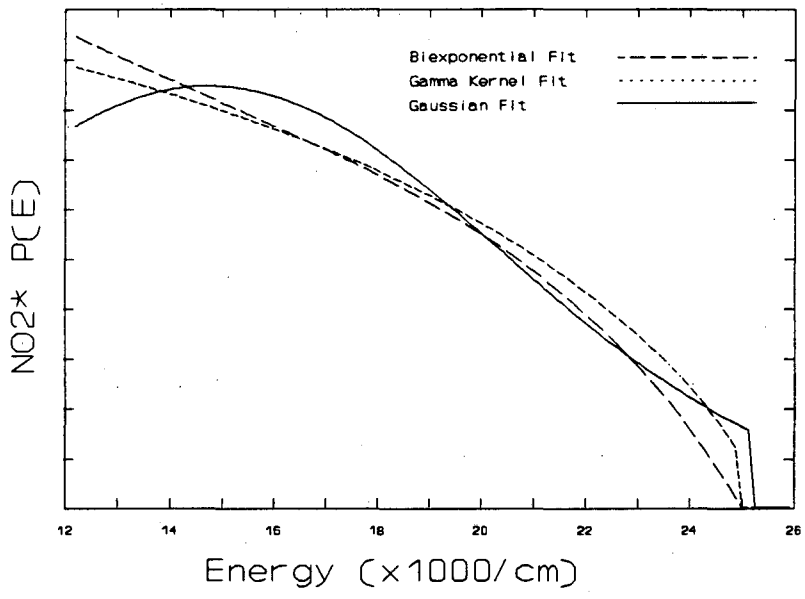

Figure 22. 241nm $HONO_2$ NO_2^* $P(E_{int})$: θ = 24,995 cm^{-1}. See also Figure 8 and Table VII.

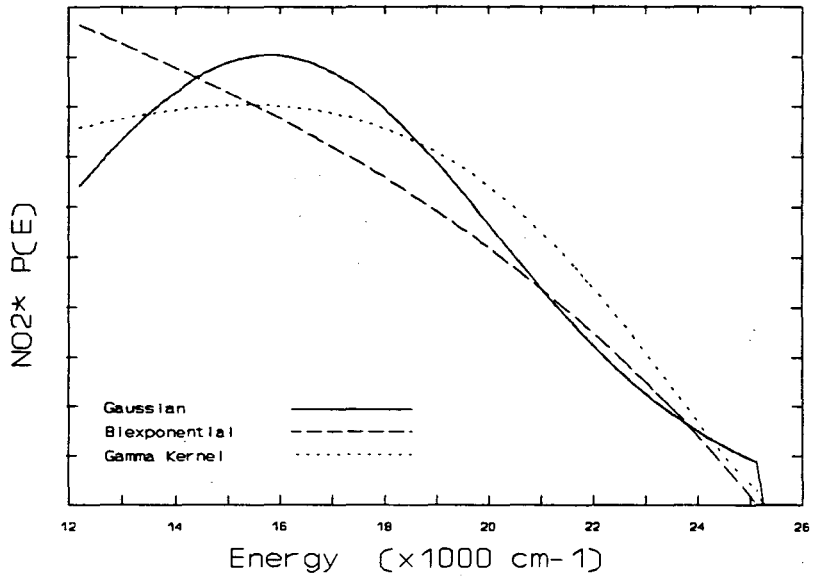

Figure 23. 245nm $HONO_2$ NO_2^* $P(E_{int})$: θ = 24,315 cm^{-1}. See also Figure 9 and Table VIII.

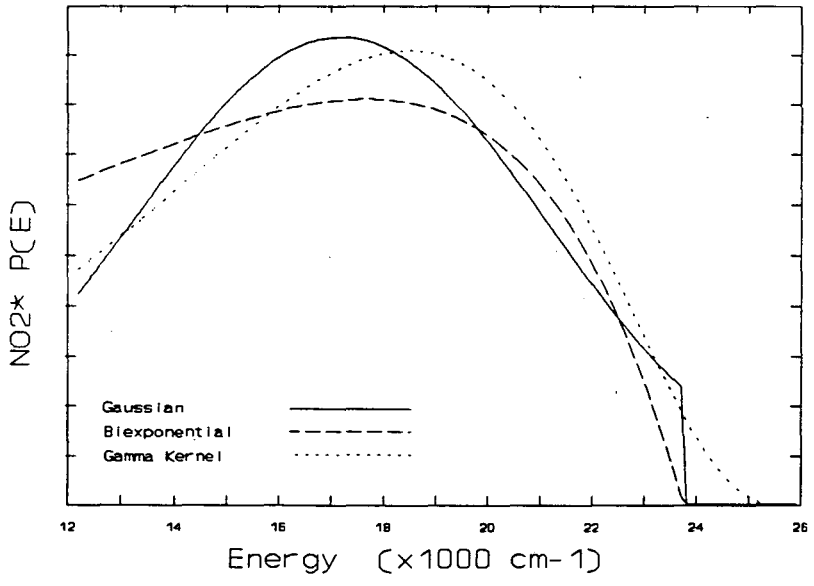

Figure 24. 248.5nm $HONO_2$ NO_2^* $P(E_{int})$: θ = 23,740 cm^{-1}. See also Figure 10 and Table IX.

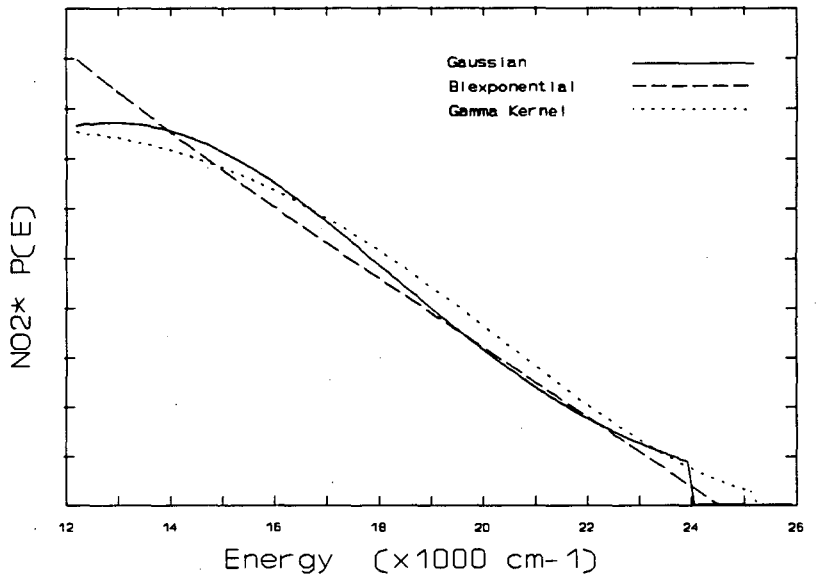

Figure 25. 250nm $HONO_2$ NO_2^* $P(E_{int})$: θ = 23,500 cm^{-1}. See also Figure 11 and Table X.

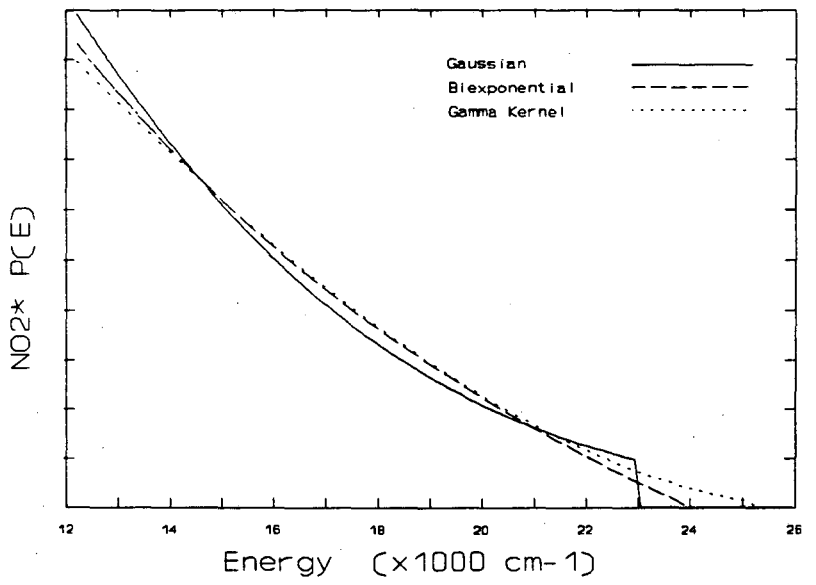

Figure 26. 255nm $HONO_2$ NO_2^* $P(E_{int})$: θ = 22,715 cm^{-1}. See also Figure 12 and Table XI.

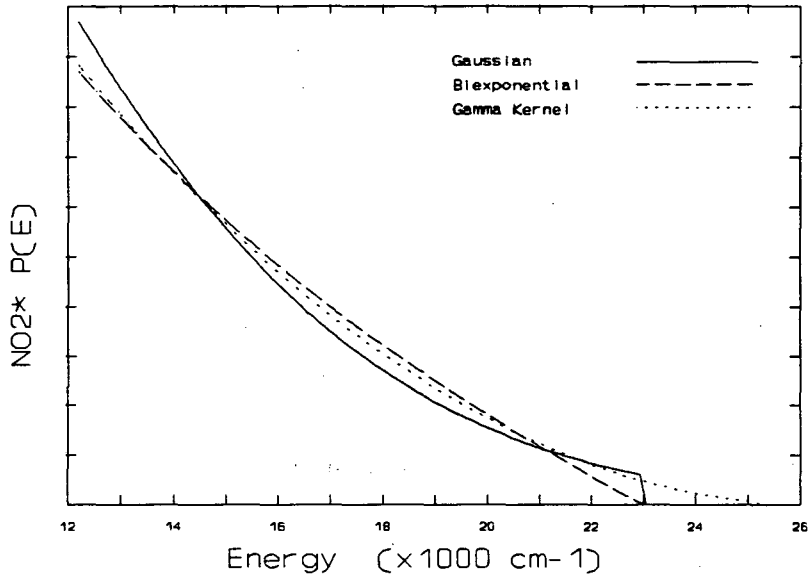

Figure 27. 260nm $HONO_2$ NO_2^* $P(E_{int})$: θ = 21,960 cm^{-1}. See also Figure 13 and Table XII.

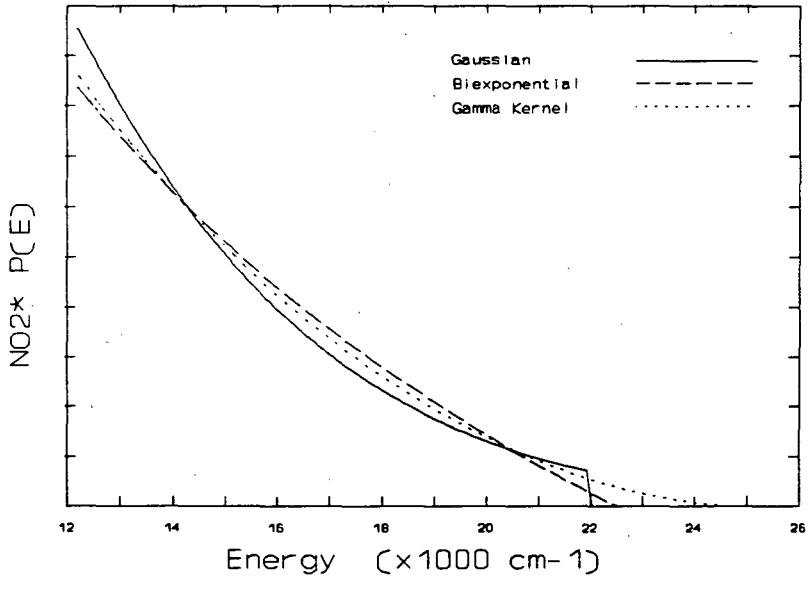

Figure 28. 265nm $HONO_2$ NO_2^* $P(E_{int})$: θ = 21,235 cm^{-1}. See also Figure 14 and Table XIII.

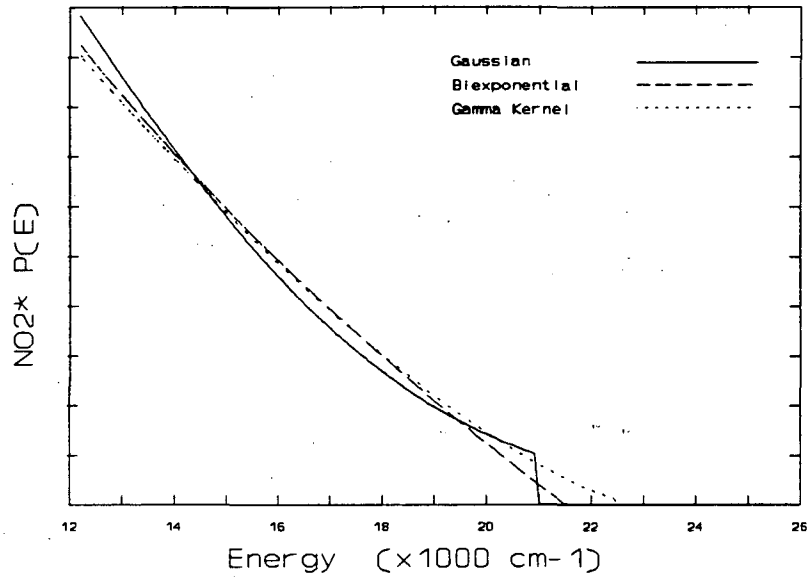

Figure 29. 270nm $HONO_2$ NO_2^* $P(E_{int})$: θ = 20,535 cm^{-1}. See also Figure 15 and Table XIV.

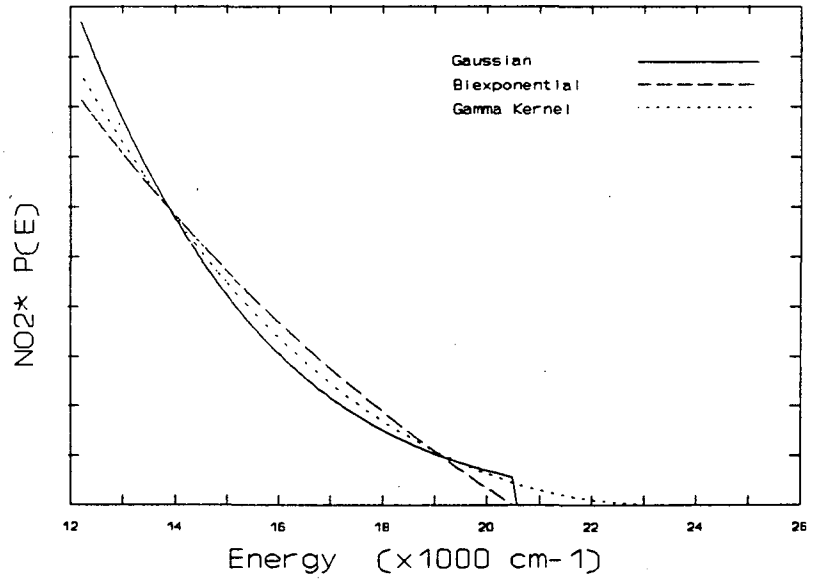

Figure 30. 275nm $HONO_2$ NO_2^* $P(E_{int})$: θ = 19,865 cm^{-1}. See also Figure 16 and Table XV.

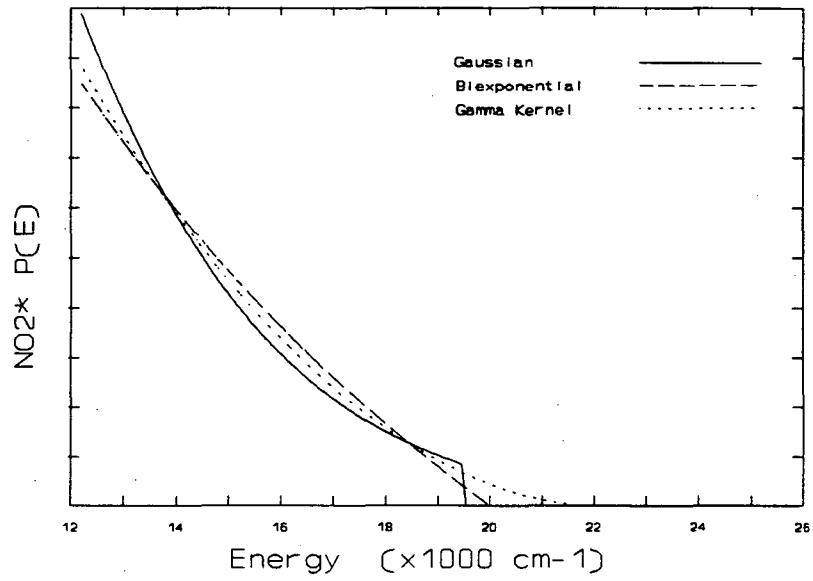

Figure 31. 280nm $HONO_2$ NO_2^* $P(E_{int})$: θ = 19,215 cm^{-1}. See also Figure 17 and Table XVI.

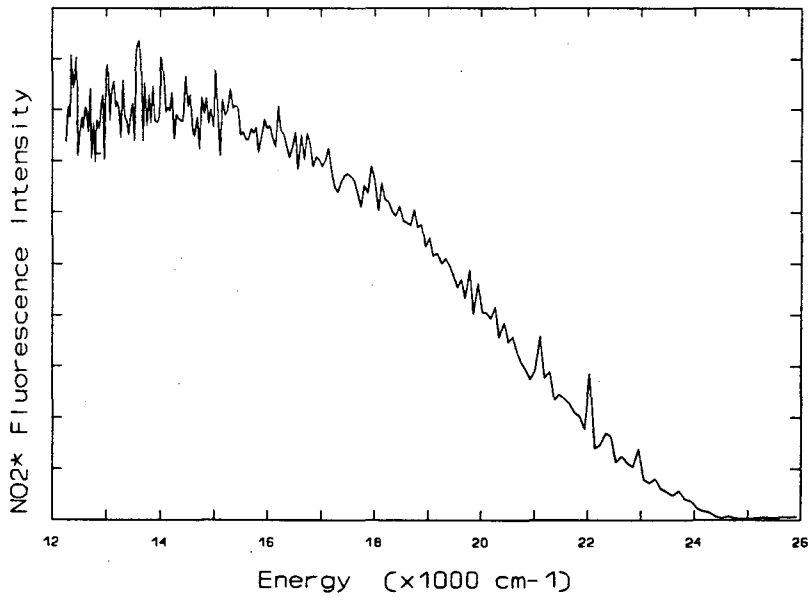

Figure 32. 235nm $ClNO_2$ NO_2 PIF spectrum.

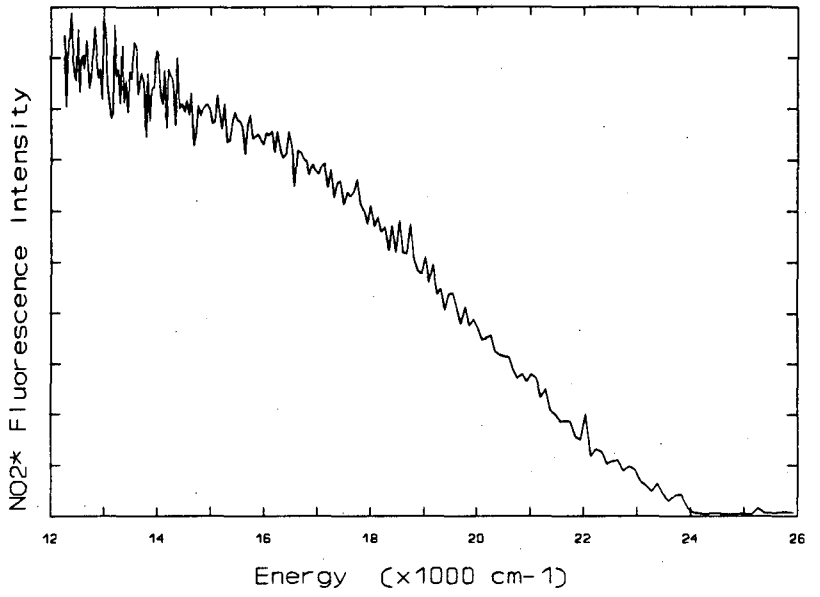

Figure 33. NO_2^* PIF signal from 240nm $ClNO_2$ photodissociation.

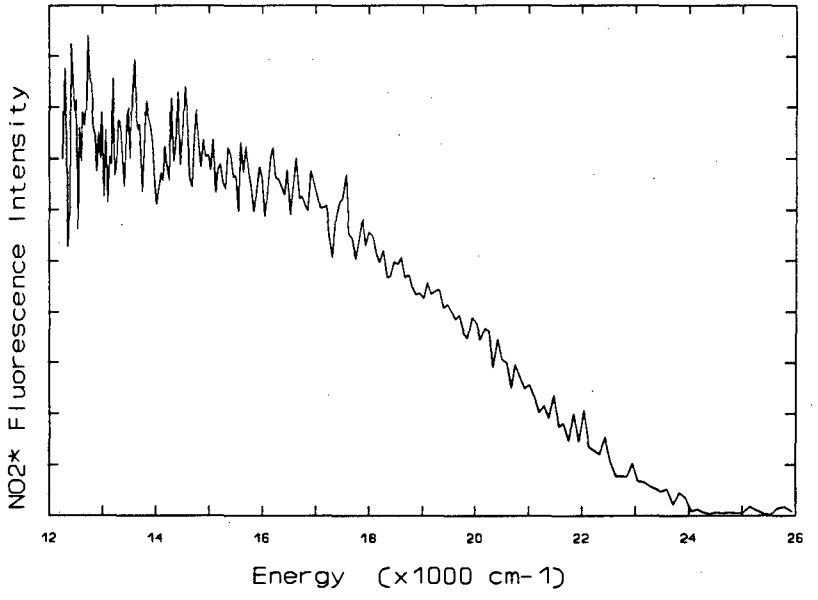

Figure 34. NO_2^* PIF signal from 245nm $ClNO_2$ photodissociation.

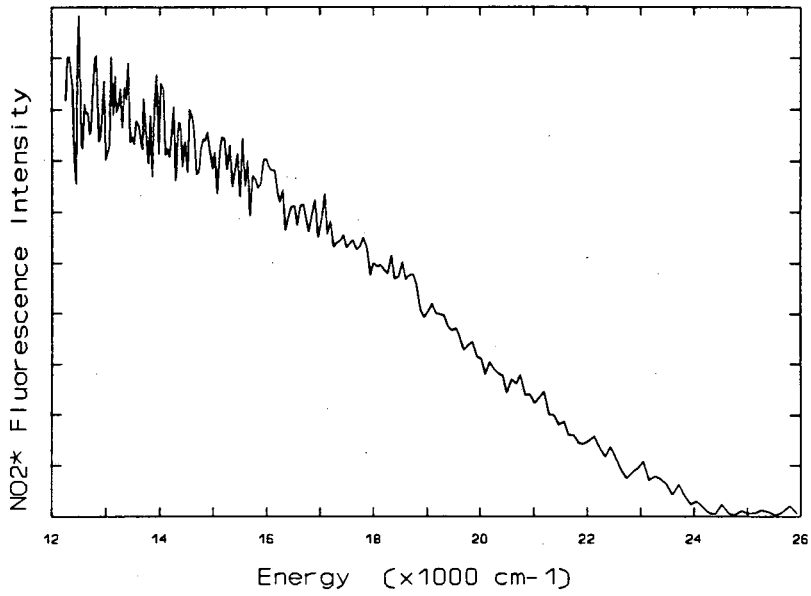

Figure 35. NO_2^* PIF signal from 250nm $ClNO_2$ photodissociation.

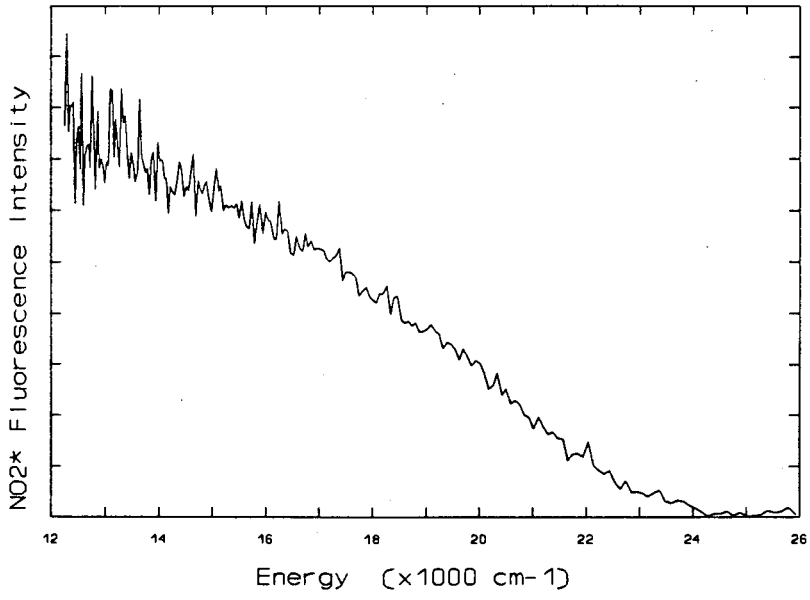

Figure 36. NO_2^* PIF signal from 255nm $ClNO_2$ photodissociation.

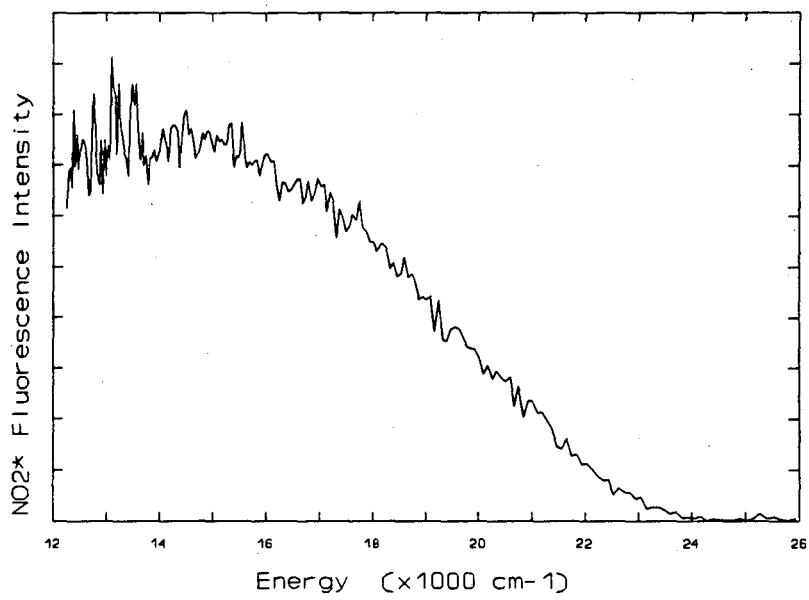

Figure 37. NO_2^* PIF signal from 260nm $ClNO_2$ photodissociation.

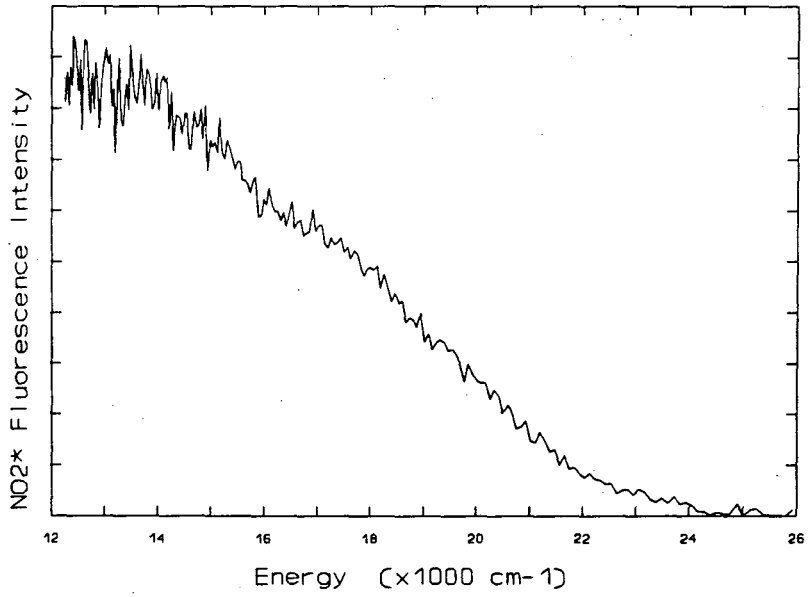

Figure 38. NO_2^* PIF signal from 270nm $ClNO_2$ photodissociation.

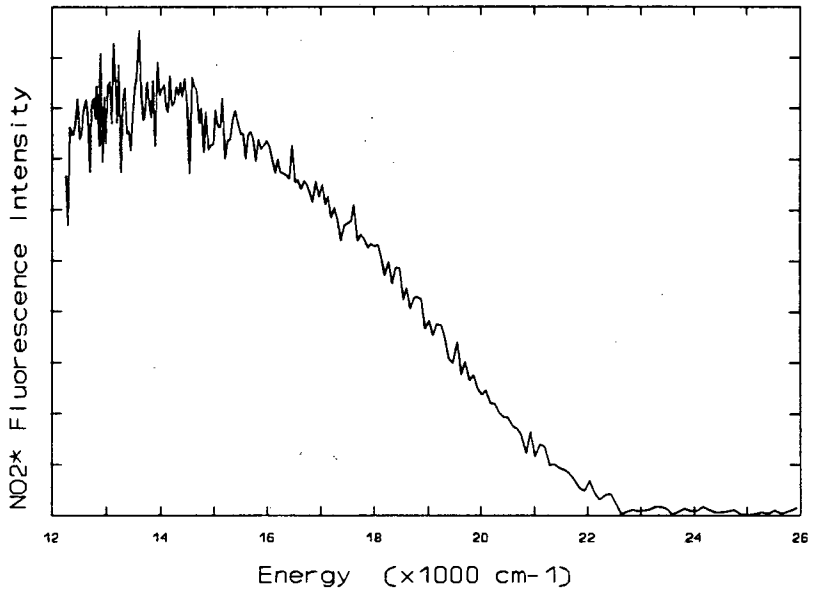

Figure 39. NO_2^* PIF signal from 275nm $ClNO_2$ photodissociation.

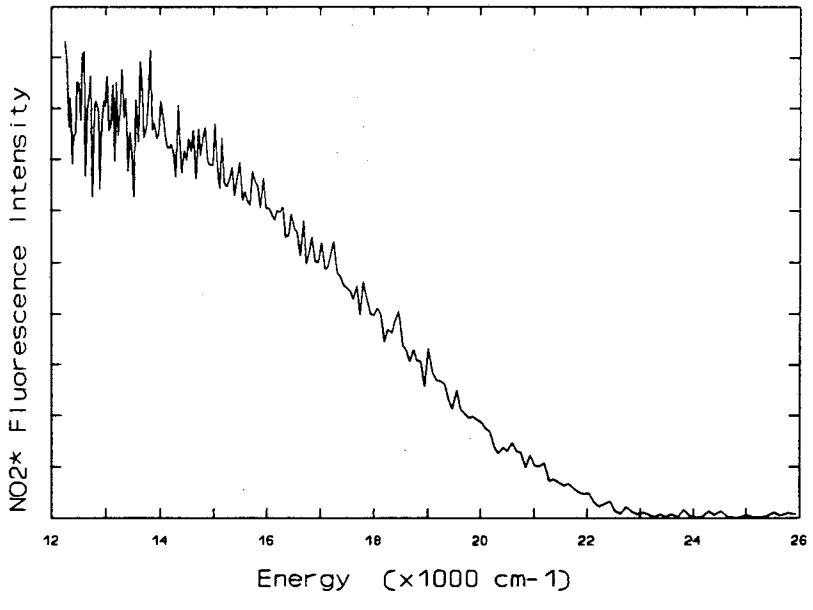

Figure 40. NO_2^* PIF signal from 280nm $ClNO_2$ photodissociation.

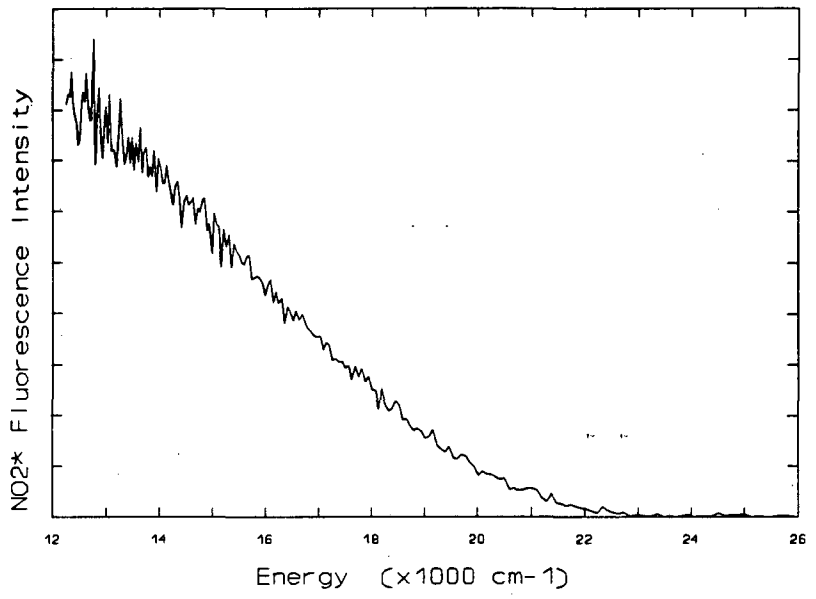

Figure 41. NO_2^* PIF signal from 290nm $ClNO_2$ photodissociation.

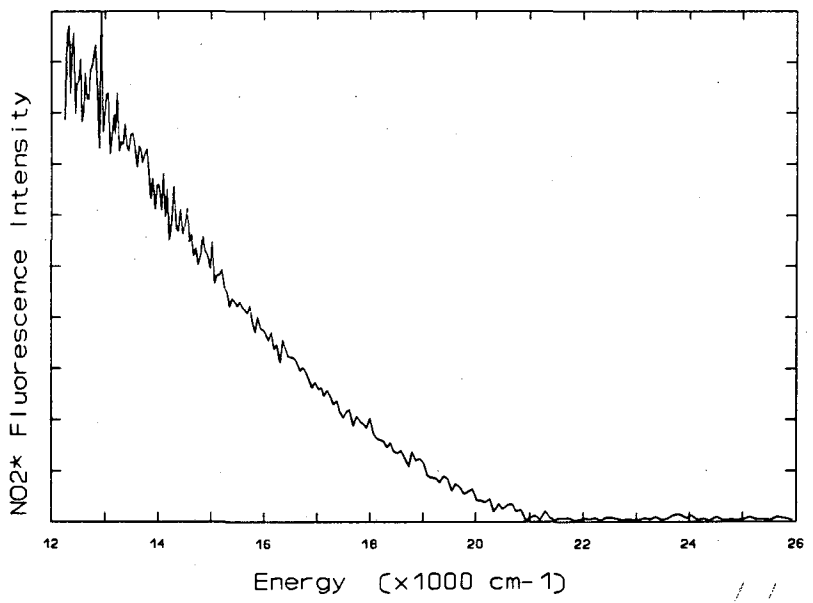

Figure 42. NO_2^* PIF signal from 300nm $ClNO_2$ photodissociation.

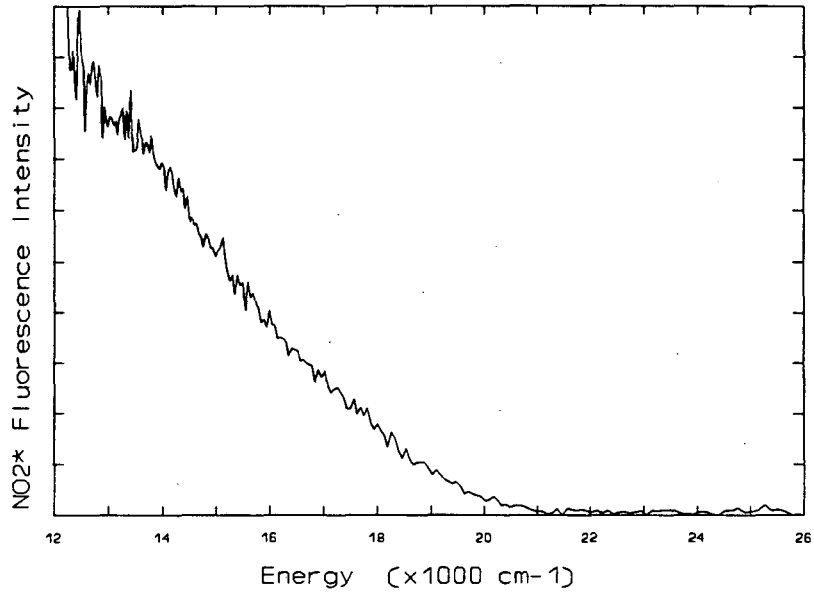

Figure 43. NO_2^* PIF signal from 308nm $ClNO_2$ photodissociation.

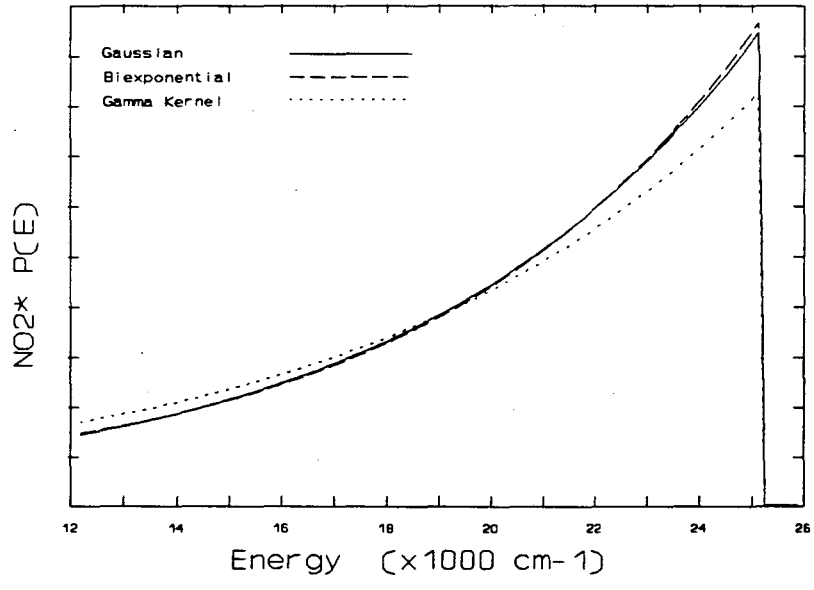

Figure 44. 235nm $ClNO_2$ NO_2^* $P(E_{int})$: θ = 30,690 cm^{-1}. See also Figure 32 and Table XVII.

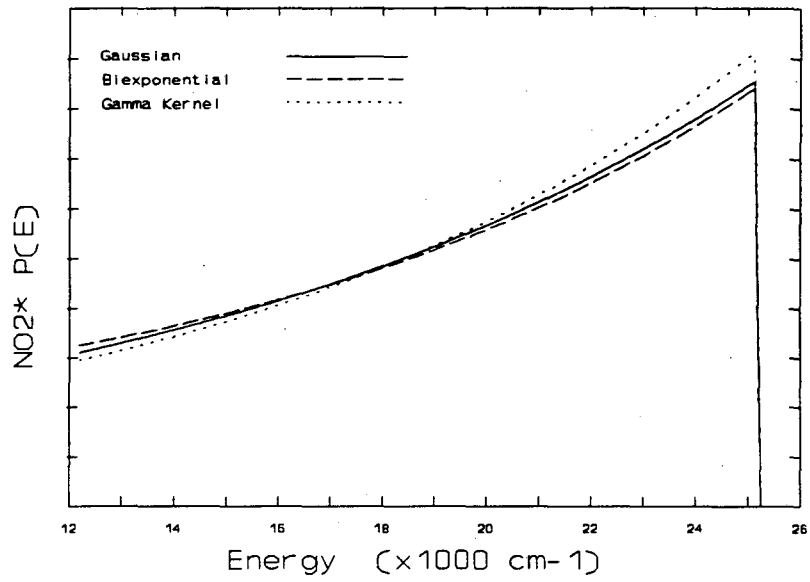

Figure 45. 240nm $ClNO_2$ NO_2^* $P(E_{int})$: θ = 29,800 cm^{-1}. See also Figure 33 and Table XVIII.

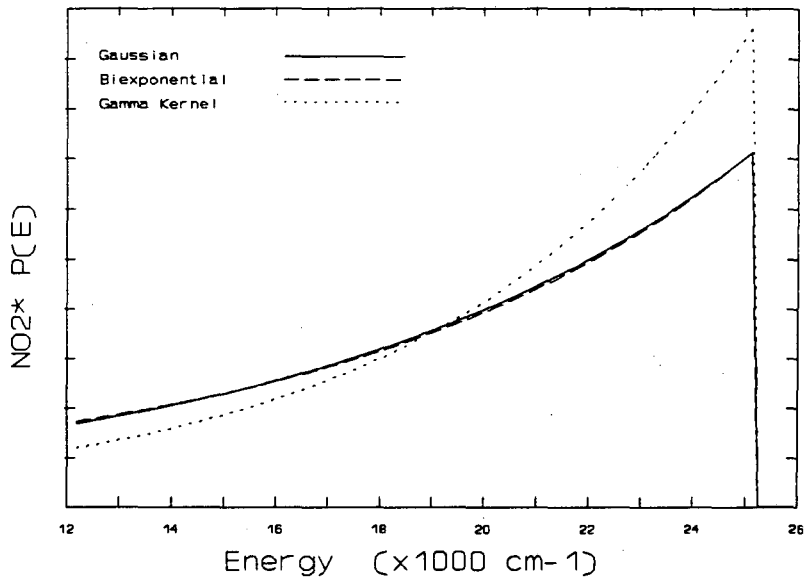

Figure 46. 245nm $ClNO_2$ NO_2^* $P(E_{int})$: θ = 28,950 cm^{-1}. See also Figure 34 and Table XIX.

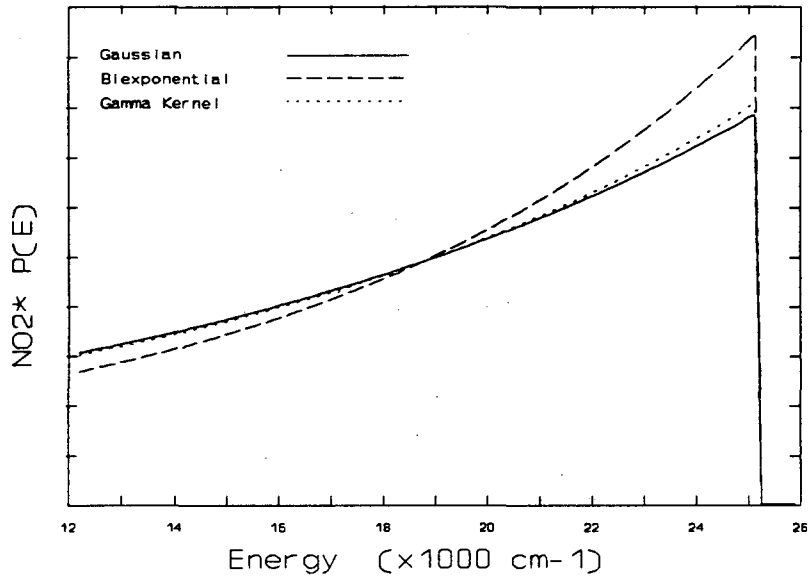

Figure 47. 250nm $ClNO_2$ NO_2^* $P(E_{int})$: θ = 28,135 cm^{-1}. See also Figure 35 and Table XX.

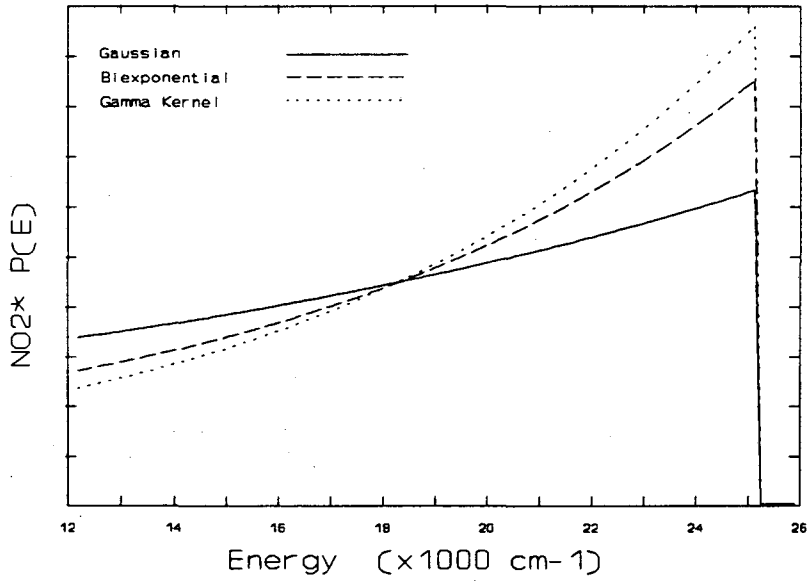

Figure 48. 255nm $ClNO_2$ NO_2^* $P(E_{int})$: θ = 27,350 cm^{-1}. See also Figure 36 and Table XXI.

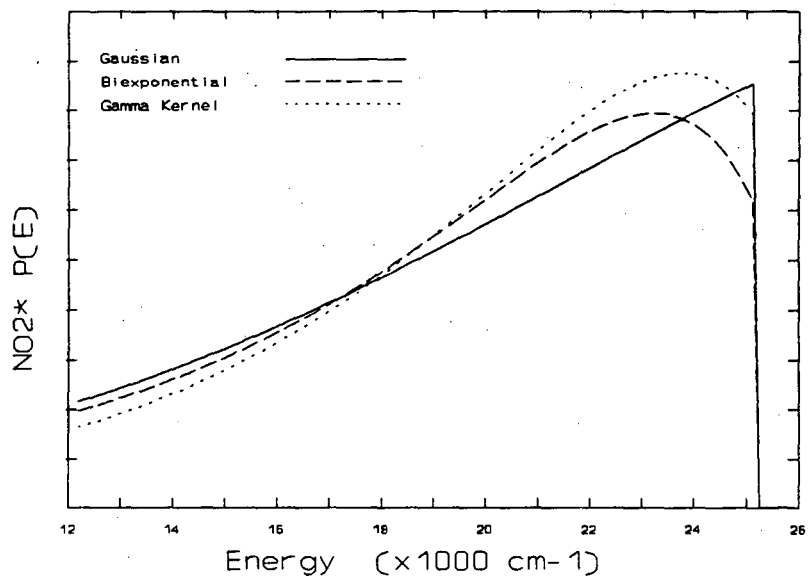

Figure 49. 260nm $ClNO_2$ NO_2^* $P(E_{int})$: θ = 26,595 cm^{-1}. See also Figure 37 and Table XXII.

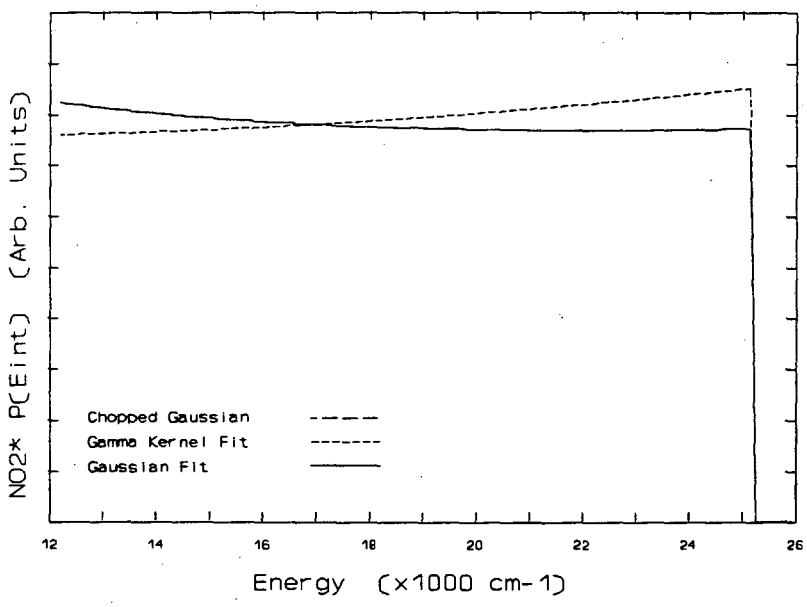

Figure 50. 270nm $ClNO_2$ NO_2^* $P(E_{int})$: θ = 25,170 cm^{-1}. See also Figure 38 and Table XXIII.

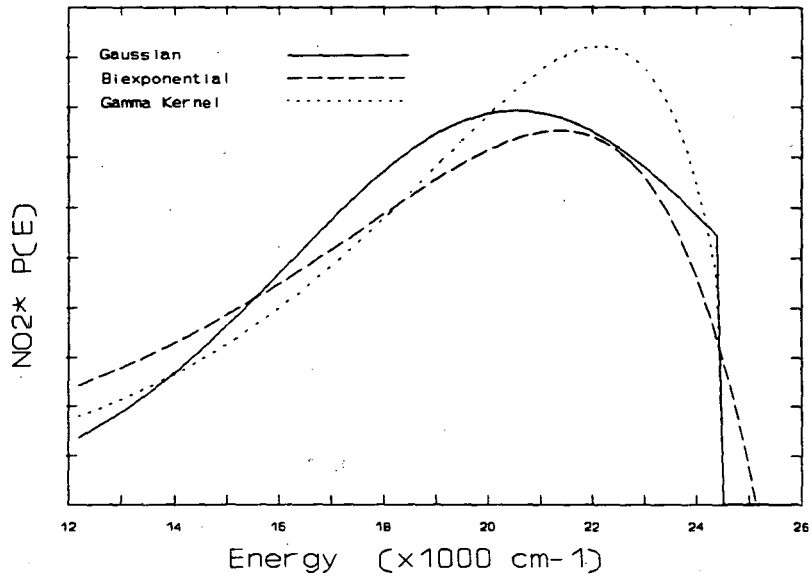

Figure 51. 275nm $ClNO_2$ NO_2^* $P(E_{int})$: θ = 24,500 cm^{-1}. See also Figure 39 and Table XXIV.

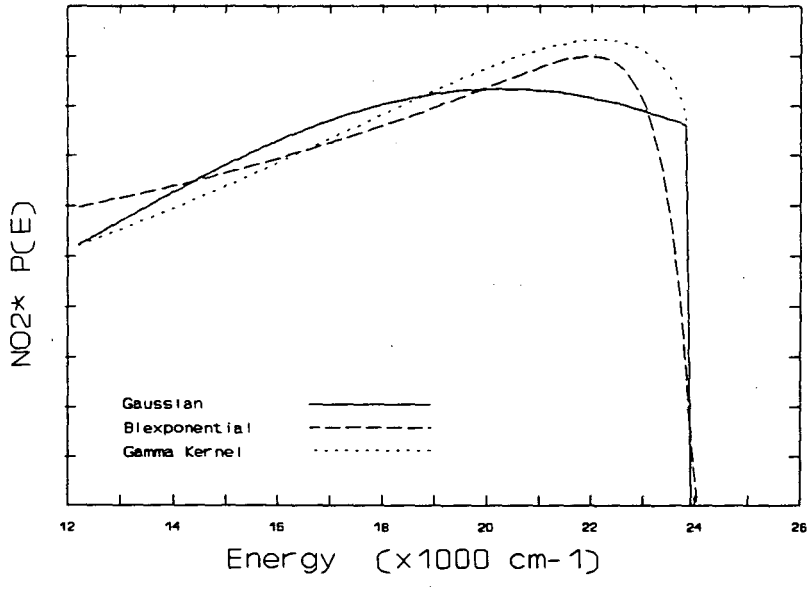

Figure 52. 280nm $ClNO_2$ NO_2^* $P(E_{int})$: θ = 23,850 cm^{-1}. See also Figure 40 and Table XXV.

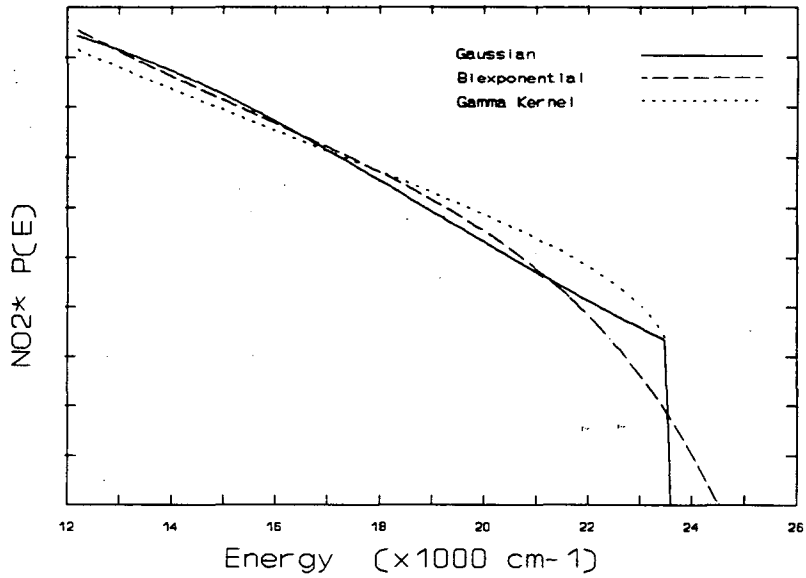

Figure 53. 290nm $ClNO_2$ NO_2^* $P(E_{int})$: θ = 22,620 cm^{-1}. See also Figure 41 and Table XXVI.

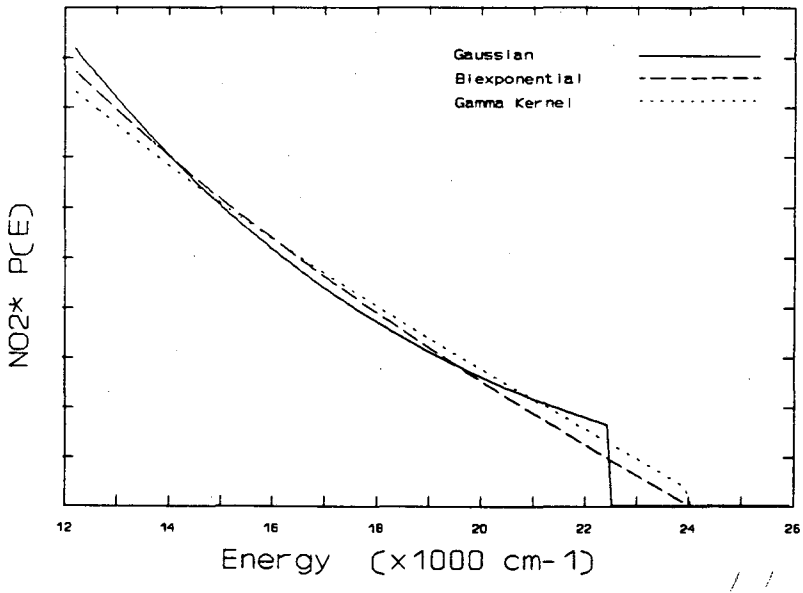

Figure 54. 300nm $ClNO_2$ NO_2^* $P(E_{int})$: θ = 21,470 cm^{-1}. See also Figure 42 and Table XXVII.

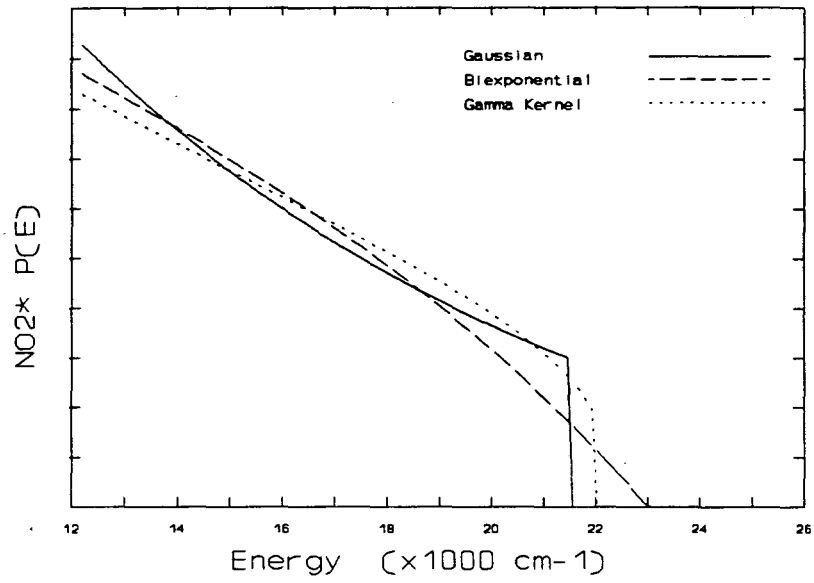

Figure 55. 308nm $ClNO_2$ NO_2^* $P(E_{int})$: θ = 20,600 cm^{-1}. See also Figure 43 and Table XXVIII.

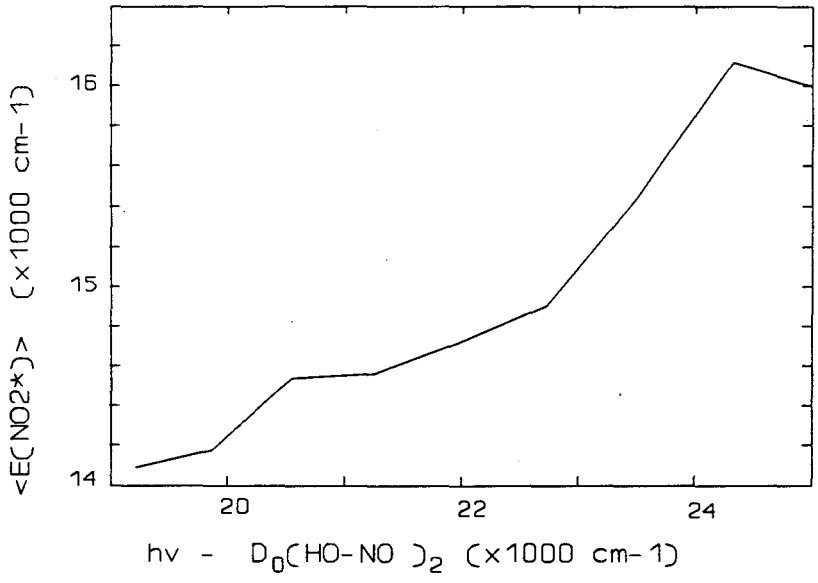

Figure 56. The average NO_2^* $P(E_{int})$ from $HONO_2$ photodissociation plotted as a function of θ.

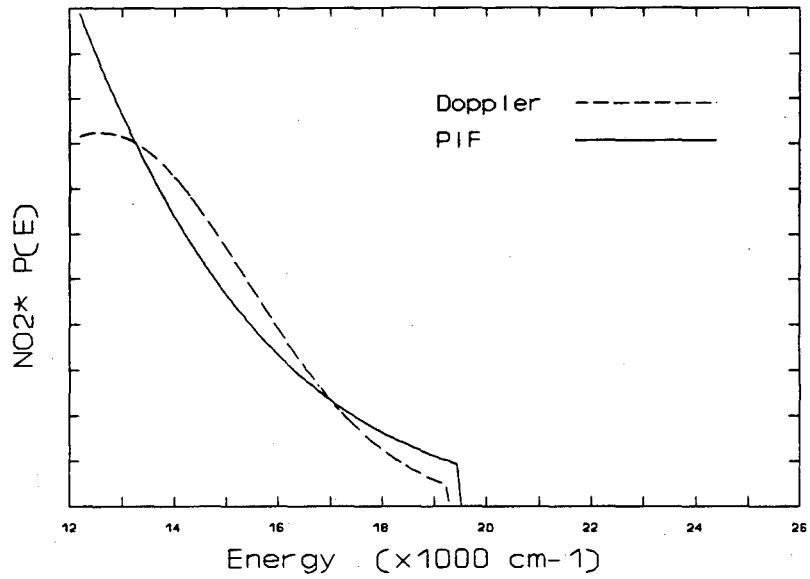

Figure 57. 280nm $HONO_2$ PIF NO_2^* $P(E_{int})$ and August's NO_2 $P(E_{int})$ [Ref. 8]. The Doppler $P(E_{int})$ is Gaussian with ν = 12,600 and σ = 6820. θ = 19,215 cm^{-1}.

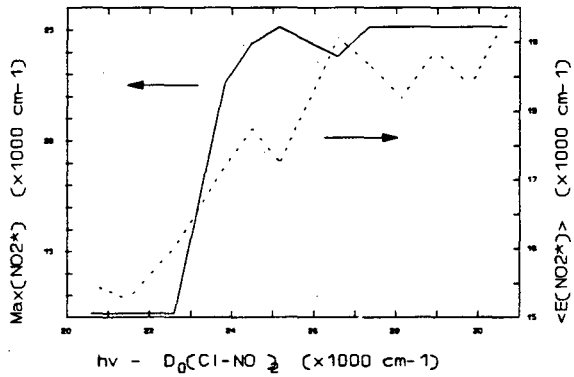

Figure 58. Average (dashed line) and most probable (solid line) energies for the $ClNO_2$ NO_2^* $P(E_{int})$ as a function of θ.

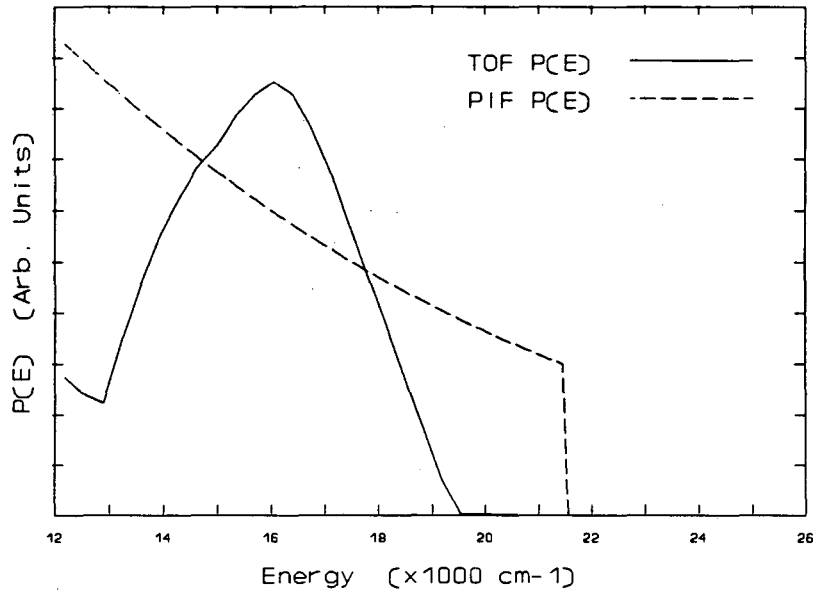

Figure 59. PIF NO_2^* $P(E_{int})$ and TOF NO_2 $P(E_{int})$ from 308nm $ClNO_2$ photolysis. θ = 20,600 cm^{-1}.

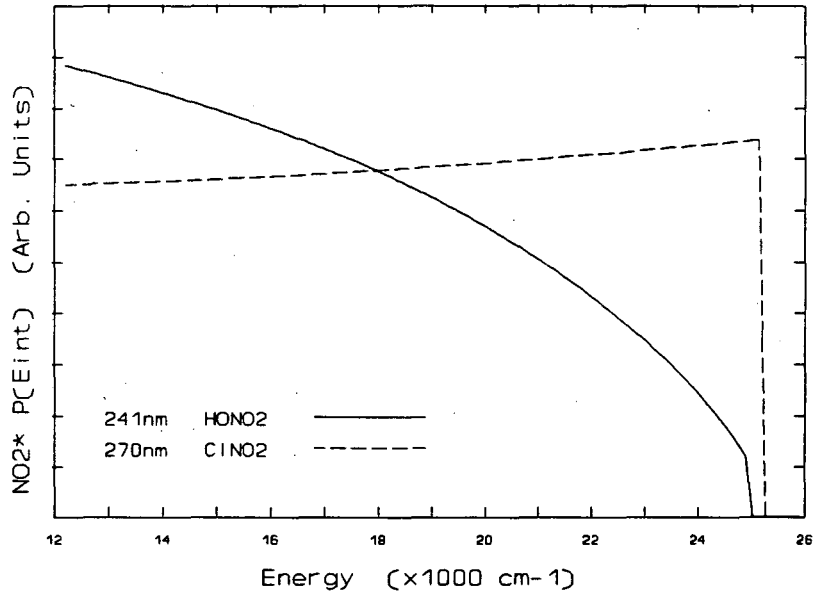

Figure 60. NO_2^* $P(E_{int})$ distributions for 270nm $ClNO_2$ and 241nm $HONO_2$ PIF experiments. $\theta \approx$ 25,100 cm^{-1}.

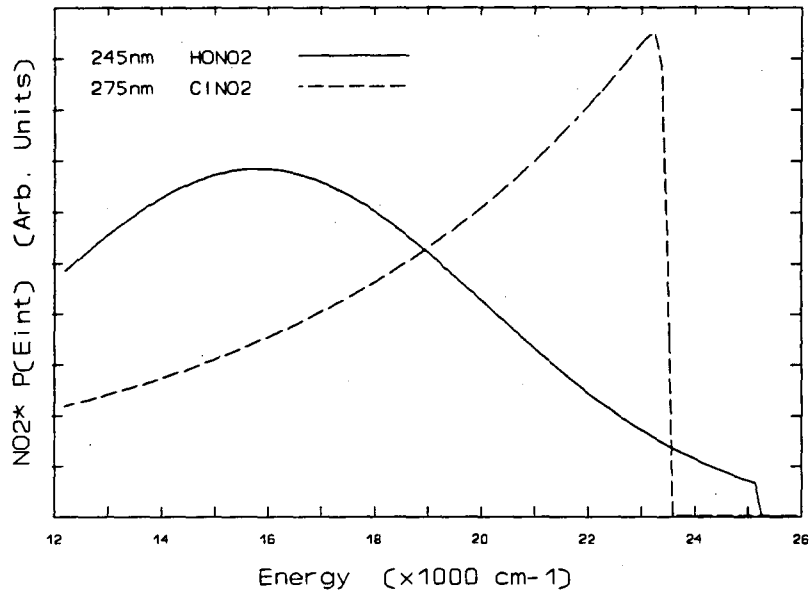

Figure 61. NO_2^* $P(E_{int})$ dsitributions for 275nm $ClNO_2$ and 245nm $HONO_2$ PIF experiments. $\theta \approx 24{,}400\ cm^{-1}$.

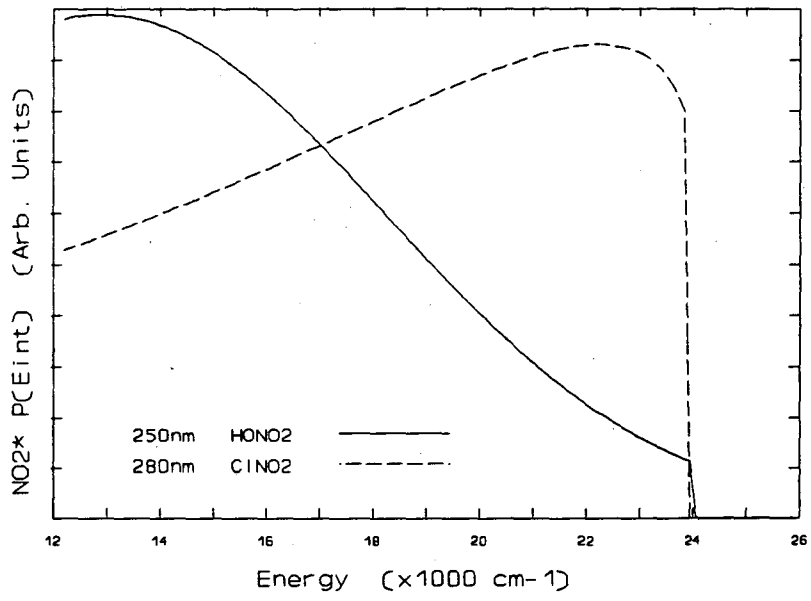

Figure 62. NO_2^* $P(E_{int})$ distributions for 280nm $ClNO_2$ and 250nm $HONO_2$ PIF experiments. $\theta \approx 23{,}650\ cm^{-1}$.

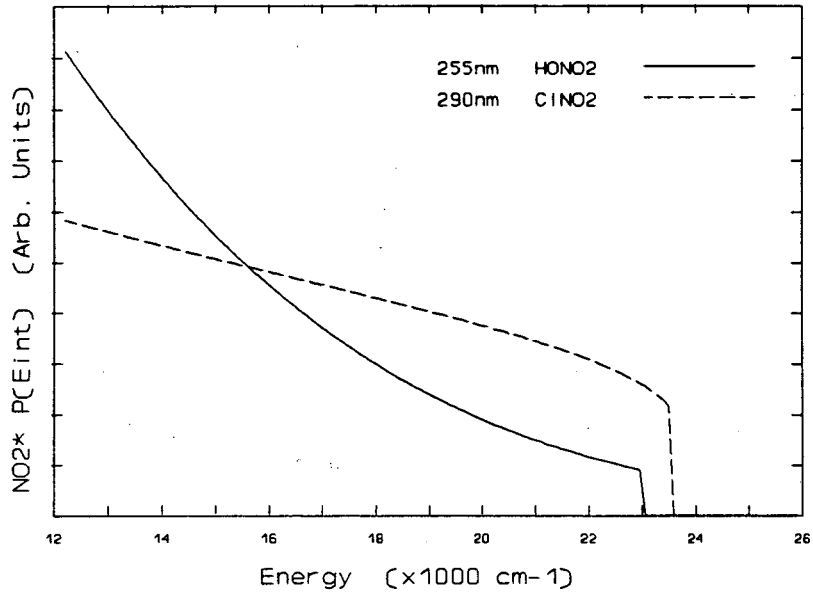

Figure 63. NO_2^* $P(E_{int})$ distributions for 290nm $ClNO_2$ and 255nm $HONO_2$ PIF experiments. $\theta \approx 22{,}650\ cm^{-1}$.

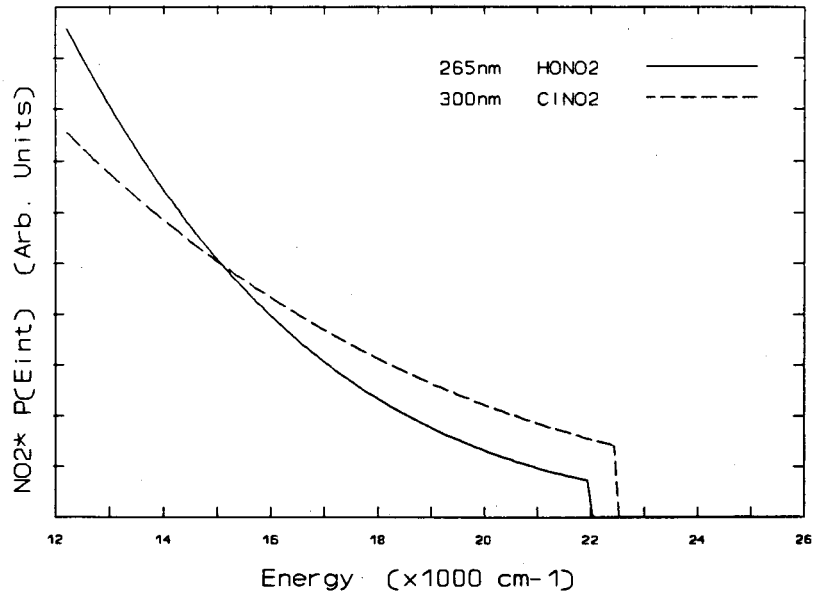

Figure 64. NO_2^* $P(E_{int})$ distributions for 300nm $ClNO_2$ and 265nm $HONO_2$ PIF experiments. $\theta \approx 21{,}350\ cm^{-1}$.

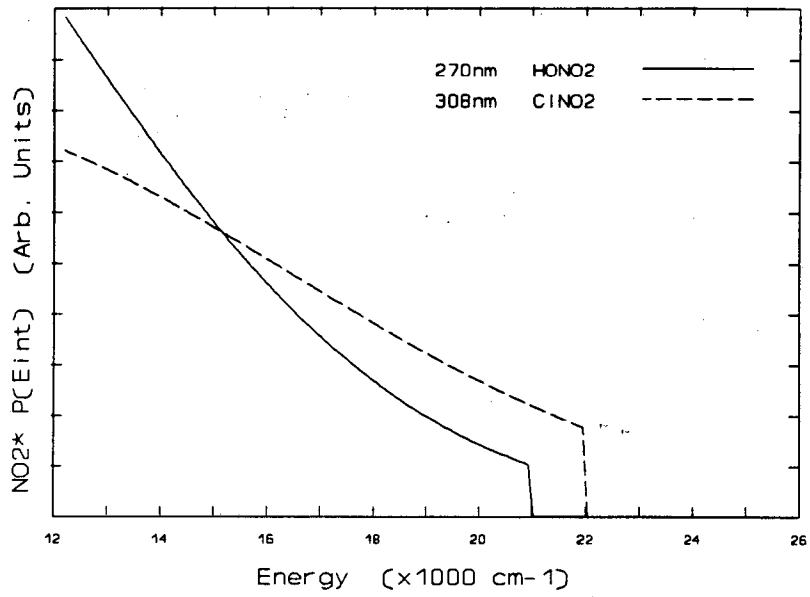

Figure 65. NO_2^* $P(E_{int})$ distributions for 308nm $ClNO_2$ and 270nm $HONO_2$ PIF experiments. $\theta \approx 20{,}570\ cm^{-1}$.

LAWRENCE BERKELEY LABORATORY
UNIVERSITY OF CALIFORNIA
INFORMATION RESOURCES DEPARTMENT
BERKELEY, CALIFORNIA 94720